The Combined Effect of Particle Shape and Grain Size Distribution on the Critical State Parameters of Coarse-Grained Soils

by

Ammar Alshammari

A dissertation submitted in partial fulfillment of

the requirements for the degree of

Doctor of Philosophy

(Geological Engineering)

at the

University of Wisconsin-Madison

2022

Date of final oral examination: 07/ 27/ 2022

The dissertation is approved by the following members of the Final Oral Committee:

Dante Fratta, Associate Professor, Geological Engineering

William J. Likos, Professor, Civil and Environmental Engineering

James Tinjum, Associate Professor, Civil and Environmental Engineering

Bu Wang, Assistant Professor, Civil and Environmental Engineering

Lucas Zoet, Associate Professor, Geoscience

Dedication

To my Parents, siblings, wife, and kids

Abstract

Particle shape and grain size distribution (GSD) control the mechanical response of coarse-grained soils. Based on that, several researchers have sought the link between coarse-grained soils' intrinsic properties (e.g., GSD, and particles' roughness, roundness, and aspect ratio) and the mechanical response (e.g., stiffness and strength). Unfortunately, those studies investigate the effects of particle shape descriptors and GSD on the mechanical response of coarse-grained soils separately. However, both sets of parameters are required to fully capture the mechanical behavior of the coarse-grained soils.

We implemented a systematic experimental study to assess the combined effect of particle shape (i.e., roundness) and GSD on the parameters that control the critical state line in coarse-grained particles. In this regard, we evaluated the particulate material response within the critical state soil mechanics model because it is a robust framework that captures particulate materials' ultimate volumetric and shear strength response. Furthermore, the critical state soil mechanics model should be adopted while designing safe geotechnical engineering structures, as recent infrastructure failures have shown (Jefferies, 2022).

We tested fifty-six mixtures made of mono-sized, bi-sizes, and poly-sized glass beads and crushed glass particles. These mixtures permit studying the combined effect of particle shape and GSD on critical state parameters. To assess the critical state friction angle,

- We deployed a rotating cylinder to capture the angle of repose of failing particulate material.
- We developed a new algorithm to systematically analyze digital images and measure particulate material's angle of repose and the void ratio at failure.

The repose angle mimics the critical state friction angle of particulate materials. While for testing the critical state void ratio,

- We modified the simple method proposed by Santamarina and Cho (2001) to evaluate the critical state parameters on the void ratio-vs.-the log of the mean effective stress space.

The significant advantage of our methodology is that it allows the systematic and straightforward evaluation of the effect intrinsic properties of the tested materials at low applied effective stresses to avoid particle breakage. In addition, our modifications improved the quality of the collected data.

Results show that the particle shape of the small-size fractions significantly influences the critical state parameters more than the coarse-grained fractions. However, the interaction of the particle shape on different size fractions is complex. For example, the intercept of the critical state line on the compressional plane is affected by the GSD and particle shapes of both the large-size and small-size fractions. Furthermore, the results appear to be controlled by the particle shape of the large-size fractions when the small-size fractions do not fill all the void spaces left by the large-size particles. In contrast, the particle shape of the small-size fraction controls the critical state parameters when small particles fill all voids.

Based on the experimental observations, interpretation, and analyses, we proposed calculating the equivalent roundness of mixtures based on the surface area. This equivalent roundness correlates well with the critical state parameters. Furthermore, the correlations provide a greater coefficient of correlations when functions include both roundness (i.e., a measure of particle shape) and coefficient of curvature (i.e., a measure of GSD). The proposed correlations allow estimating all the critical state parameters based on intrinsic properties of the coarse-grained soils' particles.

Acknowledgments

In the first place, I thank Allah, the most gracious and the most merciful. Without Allah's help, I will not be able to learn and accomplish my Ph.D. degree. I cannot thank Allah enough for the bounties and blessings that He gave me.

I want to express my sincerest thanks to my advisor, Professor Dante Fratta. Beyond his successful mentorship, he was a good character, a man of integrity, a friendly presence, and more. I have learned a lot of academic and nonacademic things from Dante. Furthermore, I would not waste any chance of collaborating with him in the future. For the prospective students, I would say you are lucky if you are working with Dante.

I also want to express my gratitude to my Ph.D. committee, Professor William Likos, Professor James Tinjum, Professor Bu Wang, and Professor Lucas Zoet for their valuable feedback on my research proposal presentation. During that day, I was challenged constructively to hone my critical thinking and look at different dimensions of any problem. Over and above, I interacted with those professors during my graduate studies and learned many lessons.

I cannot forget to thank the many instructors I have had throughout my life, from kindergarten to graduate school. I would not be who I am without my teachers' dedicated efforts. So, thank you so much my teachers!

I would like to thank King Fahd University of Petroleum and Minerals (KFUPM) for providing me with a scholarship to pursue my graduate studies. I also thank the Wisconsin Department of Transportation (WisDOT) for providing funds to support my research.

A great learning resource I had was my interactions with fellow graduate students. I thank all my colleagues who enhanced my knowledge through arguments, tutoring, or chatting. My list of

colleagues is larger than to be listed here. However, I will mention those with whom I had thoughtful discussions or who taught me valuable skills on my Ph.D. research: Mayukh Talukdar, Mike Zimmerman, Moayad Alnammi, Mohammed Omar, Susan Richmond, and Rayan Alkashgari.

I would like to thank all staff who facilitated my research experimental work. In the Geoengineering lab, Xiaodong Wang (Buff) is the support technician. In Makerspace lab, Brett Prussack helped me design and cut some of the testing kits.

I am so grateful to the uncountable friends who made my graduate school life easier and more enjoyable. In addition, I wholeheartedly thank my parents, siblings, wife, and kids for their unconditional love and continued prayers and support.

Table of Content

Dedication i

Abstract ii

Acknowledgments iv

List of Tables x

List of Figures xi

CHAPTER 1: Introduction and Motivation 1

1.1. Load-Deformation Behavior of Materials 1

1.2. Critical State Soil Mechanics 2

1.3. The Motivation of the Dissertation 3

1.4. Research Hypotheses 4

1.5. Scope of Work 5

1.6. References 6

CHAPTER 2: An Image Processing Algorithm for the Systematic Evaluation of the Angle of Repose and Void Ratio of Particulate Media 12

Abstract 12

2.1. Introduction 13

2.2. The Testing Cylinder 14

2.3. The Angle of Repose and Void Ratio Calculations 15

2.4. Material Testing 21

2.5. Testing Challenges and Limitations 22

2.6. Conclusions 24

2.7. Acknowledgments 25

2.8. References 26

2.9. Appendix: Matlab Script 45

CHAPTER 3: The Combined Effect of Gradation and Particle Shape on Coarse-Grained Soils' Critical State Friction Angle 48

Abstract 48

3.1. Introduction 50

3.2. Frictional Behavior of Coarse-grained Soils 52

3.3. Index Parameters and Frictional Response of Soils 54

3.3.1. The effect of mineralogy 54

3.3.2. The effect of the grain size distribution 55

3.3.3. The effect of the particle shape 56

3.4. Materials and Methods 57

3.4.1. Material 57

3.4.2. Particle shape measurement 58

3.4.3. The angle of repose measurement 59

3.5. Results and Interpretation 60

3.5.1. Mono-sized mixtures 60

3.5.2. Bi-sized mixtures 63

3.5.3. Poly-sized mixtures 65

3.6. Equivalent Roundness 66

3.6.1. Roundness based on the volume fraction 66

3.6.2. Roundness based on particle numbers 67

3.6.3. Roundness based on the surface area 68

3.7. Discussion 68

3.8. Conclusions 70

3.9. Acknowledgments 72

3.10. References 72

CHAPTER 4: The Combined Effect of Particle Shape and Grain Size Distribution on the Critical State Response of Coarse-Grained Soils 99

Abstract 99

4.1. Introduction 101

4.2. Materials and Methods 103

4.2.1. Material 103

4.2.2. CS Parameters Testing 105

4.3. Results and Interpretation 110

4.3.1. Mono-sized Mixtures 111

4.3.2. Bi-sized Mixtures 112

4.3.3. Poly-sized Mixtures 116

4.4. Correlations of CS Parameters with Particles Shape 117

4.5. Conclusions 118

4.6. Acknowledgments..... 119

4.7. References..... 119

List of Tables

Table 2.1: Parameters needed for volumetric calculations. 30

Table 2.2: Size and particle shape properties of the mono-sized particles. 31

Table 2.3: Angle of repose and void ratio results of two sets of binary mixtures. The first six are binary size mixtures, and the last six are binary shape mixtures. 32

Table 3.1: Five definitions of sphericity (Zheng and Hryciw, 2015). 80

Table 3.2: Size and particle shape properties of uniform GB and CG..... 81

Table 3.3: Volume calculations statistics of thirty-five GB and CG particles retained between sieves No. 30 and No. 35. 82

Table 3.4: Particle volume and surface area of the testing particles..... 83

Table 3.5: Equivalent roundnesses calculated based on volume fraction, number of particles, and surface area of the testing mixtures. 84

Table 4.1: Size and particle shape properties of the uniform GB and CG..... 124

Table 4.2: Equivalent roundnesses calculated based on volume fraction, number of particles, and surface area of the testing mixtures (Alshammari and Fratta, 2023a). 125

Table 4.3: Our modifications to Santamarina and Cho (2001)'s method with the advantages of those modifications. 126

Table 4.4: Mixtures properties and CSL parameters. 127

List of Figures

Figure 1.1: Typical load-deformation response for concrete and steel..... 8

Figure 1.2: Confined particles under deviatoric stress. The inclined surface is the shear plane. .. 9

Figure 1.3: Deviatoric and void ratio progression of dense and loose samples subjected to shear strain. Dense samples dilate and experience peak shear strength. However, the dense and loose samples merge to constant shear strength and void ratio at the critical state. Higher effective stress leads to high strength and a lower void ratio at the critical state. 10

Figure 1.4: (a) a 3D representation of the critical state line and its projection onto the p'-q and p'-e spaces, (b) p', q, and e evolution with shear strain γ for dilative and contractive samples... 11

Figure 2.1 The transparent testing cylinder is filled with the coarse-grained particulate media and water. The inset shows the holes captured from the side in contact with the material. 33

Figure 2.2: Steps for the angle of repose and void ratio calculations. 34

Figure 2.3: Cylinder mask creation processes. 35

Figure 2.4: Eroded area between the inner circle and the O-ring. 36

Figure 2.5: Pre-processing of the material under the slope. 37

Figure 2.6: The Radon transforms of the binary image and their first derivatives. The dotted green line corresponds to the transform perpendicular to the slope of the material. 38

Figure 2.7: Minimum values of the Radon transform value versus the projection angle. 39

Figure 2.8: Rotated binary image with the Rando transform and the first derivative to determine the slope vector. 40

Figure 2.9: Steps of drawing a line along the slope. 41

Figure 2.10: Angle of repose and void ratio measurements of binary shape mixtures (D_{50} = 0.548 mm). 42

Figure 2.11: Expected boundary effect on the measurements. 43

Figure 2.12: Glass beads binary mixture made of 40% solid volume of D_{50} = 0.922 and 60% solid volume of D_{50} = 0.230 mm. The large-size particles are dark, and the small-size particles are white. 44

Figure 3.1: Hypothetical shear response of particulate material. Dashed and solid lines refer to two expected responses. 85

Figure 3.2: a) Particle shape scales: sphericity, roundness, and roughness; b) definition of roundness: the average of radii of circles fitted in the particle major features divided by the radius of the maximum inscribed circle. 86

Figure 3.3: Experimental data matrix. The upper section of the y-axis documents the critical state friction angle measurements. The lower section of the y-axis presents the void ratio calculations. The x-axis is a table showing the volumetric percentage of constituents for each of the tested mixtures. The numbers in the table are volumetric percentages (%) of different fractions in the mixture. Blue cells are for the GB, and the red cells are for the CG. The left, middle and right regions present mono-sized, bi-sized, and poly-sized mixtures. 87

Figure 3.4: The critical state friction angle as a function of roundness for the mono-sized mixture made of one type of particle, either GB or CG. The open circles correspond to Cho et al. (2006)'s measurements. 88

Figure 3.5: Variation of the critical state friction and void ratio of uniform size mixtures made of CG and GB of D_{50} = 0.548 mm. 89

Figure 3.6: Pairs of the glass bead and CG retained between sieves No. 30 and No. 35 (i.e., D_{50} = 0.548 mm). 90

Figure 3.7: Silhouettes of CG and GB pairs rested naturally on the left side and rolled on the other side on the right side. 91

Figure 3.8: Critical state friction angle and void ratio variation of GB and CG binary mixtures. 92

Figure 3.9: Critical state friction angle and void ratio variation of GB or CG binary mixtures.. 93

Figure 3.10: Pictures of the testing cylinder during the angle of repose measurements of bi-sized GB mixtures where large particles have D_{50} = 0.922 mm and small particles have D_{50} = 0.230 mm. The volume fraction of small-size particles is a) 20%, b) 40%, c) 60%, and d) 80%. 94

Figure 3.11: Three-sized mixtures made of one type of particle. Then, a different particle type replaces one size. The left side is GB dominated, and the right is CG dominated. The columns of the bottom table show the constituents of each mixture; the rows show volumetric fractions of the mean particle size of each constituent..... 95

Figure 3.12: Five-sized mixtures made of one type of particle. Then, a different particle type replaces one size. The left side is GB-particle dominated, and the right is CG-particle dominated. The columns of the bottom table show the constituents of each mixture; the rows show volumetric fractions of the mean particle size of each constituent. 96

Figure 3.13: The critical state friction angle versus equivalent roundness: (a) equivalent roundness based on volume fraction, (b) equivalent roundness based on the number of particles, and (c) equivalent roundness based on the surface area. 97

Figure 3.14: Conceptual model of the frictional behavior from large-dominant to small-dominant particles. The solid and open circles are for large and small particles, respectively. ... 98

Figure 4.1: 3D representation of the CSL and its projections onto q-p’ and e-p’ spaces. 128

Figure 4.2: Photographs of the mono-sized GB and CG particles used to make the testing mixtures..... 129

Figure 4.3: Roundness definition: the average of radii of circles fitted in the particle major features divided by the radius of the maximum inscribed circle. 130

Figure 4.4: GSD curves for the testing mixtures: (a) mono-sized mixtures, (b) bi-sized mixtures made of D_{50} = 0.922 and 0.548 mm mono-sized particles, (c) bi-sized mixtures made of D_{50} = 0.653 and 0.326 mm mono-sized particles, (d) bi-sized mixtures made of D_{50} = 0.922 and 0.230 mm mono-sized particles, (e) three-sized mixtures made of D_{50} = 0.922, 0.548 and 0.326 mm particle size where each particle has the same volume fraction of 33%, and (f) five-sized mixtures made by combining 20% volume of each of the mono-sized particles. 131

Figure 4.5: (a) complete testing apparatus, and (b) sample ready for testing. 132

Figure 4.6: Sample preparation steps. 133

Figure 4.7: Process for sample saturation. 134

Figure 4.8: Critical state parameters of all mixtures against C_u: (a) CS void ratio intercept, e_{1kPa}; (b) the slope, λ. 135

Figure 4.9: (a) CSLs for the mono-sized mixtures made of CG or GB particles, (b) e_{1kPa}, and (c) λ versus roundness. 136

Figure 4.10: (a) CSLs of mono-sized GB-CG mixtures with D_{50} = 0.548 mm, (b) e_{1kPa}, and (c) λ versus roundness. 137

Figure 4.11: CSLs of bi-sized mixtures constituted by large particles with D_{50} = 0.922 mm and small particles with D_{50} = 0.230 mm: (a) both particle sizes are GB, and (b) large size GB and small size CG. 138

Figure 4.12: A comparison between CG and GB small particles to fill the void between large particles. 139

Figure 4.13: CSLs of bi-sized mixtures constituted by large particles with D_{50} = 0.922 mm and small particles with D_{50} = 0.548 mm: (a) both particle sizes are GB, and (b) large size GB and small size CG. 140

Figure 4.14: CSLs of bi-sized mixtures constituted by large particles with D_{50} = 0.653 mm and small particles with D_{50} = 0.326 mm: (a) both particle sizes are CG, and (b) large size CG and small size GB. 141

Figure 4.15: e_{1kPa} versus volume fraction of small particles, or large particles in the upper x-axis for bi-sized mixtures: (a) large particles of D_{50} = 0.922 mm and small particles of D_{50} = 0.230 mm, (b) large GB of D_{50} = 0.922 mm and small GB of D_{50} = 0.230 mm, and (c) large particles of D_{50} = 0.653 mm and small particles of D_{50} = 0.326 mm. 142

Figure 4.16: Variation of the CSL slope, λ, of GB or CG bi-sized mixtures upon increasing small size volume fraction. 143

Figure 4.17: Variation of the CSL slope, λ, of bi-sized mixtures upon increasing small size volume fraction. The mixtures are made by one mono-size of GB and the other mono-size of CG. 144

Figure 4.18: CSL's of the three-sized mixtures. (a) GB mixtures, then on size is replaced by CG, and (b) CG mixtures, then one size is replaced by GB. 145

Figure 4.19: CSL's of the five-sized mixtures. (a) GB mixtures, then on size is replaced by CG. (b) CG mixtures, then one size is replaced by GB. 146

Figure 4.20: The CS parameters of the three-sized mixtures. 147

Figure 4.21: The CS parameters of the five-sized mixtures. 148

Figure 4.22: λ versus equivalent roundness: (a) equivalent roundness based on volume fraction, (b) equivalent roundness based on the number of particles, and (c) equivalent roundness based on the surface area. 149

Figure 4.23: Different views of a plane fitting e_{1kPa} data dependent on $R_{eq,SA,}$ and C_u. 150

CHAPTER 1:

Introduction and Motivation

1.1. Load-Deformation Behavior of Materials

The load-deformation behavior of materials is an essential engineering property used to evaluate the response of structures under the action of internal and external loads and for the design of infrastructure. Depending on how materials respond during failure, they are considered brittle or ductile. Figure 1.1 shows the typical brittle response for concrete and ductile response for mild steel. Engineers calculate the ultimate strength and stiffness of materials from these load-deformation relations. However, the load-deformation behavior is more complex for soils and other particulate media. For example, an assemblage of particles cannot bear loads without mean effective stress (p'), which is the stress felt between particles. The mean effective stress is defined as $p' = (\sigma'_1 + 2\sigma'_3)/3$, where σ'_1 and σ'_3 are major and minor principal effective stresses. Therefore, the response of the discrete material depends on the mean effective stress. Applying a deviatoric stress $q = \sigma'_1 - \sigma'_3$ on confined particles causes the particles to strain along the shearing plane (Figure 1.2). Thus, the strength and strain of discrete matter are called shear strength and shear strain.

Soils' volume would contract or dilate during shear deformation depending on the void ratio (e) and the mean effective stresses p' (Reynolds, 1885). This response has implications for the shear resistance of the particles. Dense particulate materials have higher shear resistance (i.e., peak resistance) due to dilation, but eventually, the dense and loose soils merge to a constant frictional resistance (Tayler, 1948; Rowe, 1962). At that point, the void ratio also reaches a constant value, which depends on the effective stress (i.e., critical state void ratio—Casagrande, 1936). That is,

the void ratio and the mean effective stress control the load-deformation behavior of particulate materials. Figure 1.3 sketches the complex response of particulate material subjected to shear strain (γ). First, dense samples tend to dilate and experience peak shear strength. However, dense and loose samples will converge to constant shear strength and the void ratio at the critical state. Higher effective stress leads to higher critical state shear strength and a lower critical state void ratio, and vice versa.

1.2. Critical State Soil Mechanics

The different controlling variables of soil mechanical behavior, mean effective stress, and void ratio are unified in one model: the critical state soil mechanics. Roscoe et al. (1958) and Schofield and Worth (1968) proposed critical state soil mechanics and the shear strength and void ratio at constant volume. Schofield and Worth (1968) defined the critical state as soil behaving like frictional fluid upon continuous shear strain (γ). The soils reach the critical state when the deviatoric stress, mean effective stress, and void ratio approach the critical state line (CSL), a 3D line in the p'-q-e space (Figure 1.4a).

Wood (1990) described the critical state as the nonstop plastic shearing of soil without any change in volume or effective stress (i.e., $\frac{dp\prime}{d\gamma} = \frac{dq}{d\gamma} = \frac{de}{d\gamma} = 0$—Figure 1.4b).

For simplicity, the projections on the q-p' and e-p' planes typically represent the 3D CSL (Figure 1.4a). The CSL on e-p' can be plotted in a semi-log scale to fit a straight line, i.e., on the e-log(p') plane. The CSL is defined by:

$$q_{cs} = Mp'_{cs} \qquad \textit{CSL projection on the q-p' plane} \tag{1}$$

$$e_{cs} = e_{1kPa} - \lambda \ln\left(\frac{p'_{cs}}{p_r}\right) \qquad \textit{CSL projection on the e-log(p') plane} \tag{2}$$

where the subscript cs stands for the critical state, p_r is a reference pressure equals 1 kPa, e_{1kPa} is the void ratio at 1 kPa, λ is the slope of the CSL on the e-log(p') plane, and M is the slope of the CSL on the q-p' plane. M is a function of the critical state friction angle (ϕ_{cs}) and the stress path during loading:

$$M = \frac{6\ \sin(\emptyset_{cs})}{3 - \sin(\emptyset_{cs})} \qquad \textit{for axial compression} \qquad (3)$$

$$M = -\frac{6\ \sin(\emptyset_{cs})}{3 + \sin(\emptyset_{cs})} \qquad \textit{for axial extension} \qquad (4)$$

Thus, three soil parameters, ϕ_{cs}, e_{1kPa}, and λ, are needed to capture the ultimate shear strength and volume of the soil.

1.3. The Motivation of the Dissertation

- Despite the powerful features of the critical state soil mechanic model, many engineers fail to apply it in design practices to the point where significant and preventable failures have occurred (Jefferies, 2022). For instance, Morgenstern (2018) analyzed fifteen failed tailing dams and attributed the lack of understanding of static liquefactions as the main reason. Therefore, investigating topics about the critical state soil mechanics is worth the effort.
- Various field tests can characterize the initial void ratio and state of stress of in-situ soils (Mayne et al., 2009). However, the final state needs laborious lab work, such as retrieving undisturbed samples, then testing them in triaxial compression setups. So, an economical alternative for predicting the critical state based on intrinsic soil properties would allow the adoption of critical state concepts and models even on modest projects.
- Engineers and researchers proposed correlations between soils' intrinsic properties and the critical state parameters. However, this area of expertise still requires additional research. For example, particle shape and grain size distribution (GSD) characterized the response of coarse-

grained soils at failure. The effect of these two properties on the critical state is typically studied and reported individually. However, combining particle shape and GSD to anticipate the critical state is required to capture the behavior of soils more fully.

1.4. Research Hypotheses

To address the importance of the combined effect of GSD and particle shape on the mechanical behavior and design parameters of coarse-grained soils, we evaluated the following research hypotheses:

- Particle shape descriptors are inherent material properties that describe soil shear strength and void ratio. Then, quantitative measurements of particle shape descriptors must be included in soil classification systems to help quantify soil responses.
- The combined use of GSD and particle shape parameters fully captures coarse-grained soils' critical state properties. However, the scatter in published data models show correlations between particle shape and the critical state friction angle appear to be related to particle shapes within different particle size fractions. Therefore, linking the effect of particle shape and particle sizes in a systematic experimental study will improve the quality of predictive models.
- Large-sized particles fraction contribute more to the critical state frictional strength than small-sized particle fractions. That is because larger particles contribute more to the coordination numbers by carrying most of the applied load chains than the smaller particle fractions (Wood and Maeda, 2008; Nguyen et al., 2015; Cantor et al., 2018; 2020). However, increasing small particles might significantly alter the interactions between larger particles (Thevanayagam,

2007), potentially changing how the different fractions interact and control the observed friction angle.

1.5. Scope of Work

This dissertation aims to experimentally evaluate the hypotheses' validity by testing the combined effect of particle shape and relative size of coarse-grained soil fractions on the critical state parameters (i.e., ϕ_{cs}, e_{1kPa}, and λ). We tested mono-sized, bi-sized, and poly-sized mixtures made of glass beads, crushed glass, or a combination of both. These selected materials allow the investigation of the individual and combined effect of particle shape and GSD, and the proposed methodologies are simple but robust.

The primary outcomes of this research are presented in three manuscripts to be submitted for publication. These manuscripts address the following topics:

- *An Image Processing Algorithm for the Systematic Evaluation of the Angle of Repose and Void Ratio of Particulate Media*. This paper presents a detailed explanation of a novel imaging algorithm to calculate the slope angle and void ratio of particulate media under the slope in a rotating cylinder.
- *The Combined Effect of Gradation and Particle Shape on Coarse-Grained Soils' Critical State Friction Angle*. This paper documents an experimental study to evaluate how the angle of repose, a simple and fair measurement of critical state friction angle, is controlled by particle shapes and relative sizes.
- *The Combined Effect of Particle Shape and Grain Size Distribution on the Critical State Response of Coarse-Grained Soils*. This manuscript scrutinizes the combined effect of the

relative size and particle shape on the critical state void ratio. The simple method of determining critical state parameters presented by Santamarina and Cho (2001) is modified and adapted for this investigation.

1.6. References

Cantor, D., Azéma, E., Sornay, P., and Radjai, F. (2018). Rheology and structure of polydisperse three-dimensional packings of spheres. *Physical Review E*, *98*(5), 052910.

Cantor, D., Azéma, E., and Preechawuttipong, I. (2020). Microstructural analysis of sheared polydisperse polyhedral grains. *Physical Review E*, *101*(6), 062901.

Jefferies, M. (2022). Improving governance will not be sufficient to avoid dam failures. *Proceedings of the Institution of Civil Engineers-Geotechnical Engineering*, *175*(2), 166-180.

Mayne, P. W., Coop, M. R., Springman, S. M., Huang, A. B., and Zornberg, J. G. (2009). Geomaterial behavior and testing. In *Proceedings of the 17th International Conference on Soil Mechanics and Geotechnical Engineering (Volumes 1, 2, 3, and 4)* (pp. 2777-2872). IOS Press.

Morgenstern, N. R. (2018). Geotechnical risk, regulation, and public policy. 6th Victor de Mello Lecture.

Nguyen, D. H., Azéma, E., Sornay, P., and Radjai, F. (2015). Effects of shape and size polydispersity on strength properties of granular materials. *Physical Review E*, *91*(3), 032203.

Reynolds, O. (1885). LVII. On the dilatancy of media composed of rigid particles in contact. With experimental illustrations. The London, Edinburgh, and Dublin Philosophical Magazine and Journal of Science, 20(127), 469-481.

Rowe, P. W. (1962). The stress-dilatancy relation for static equilibrium of an assembly of particles in contact. *Proceedings of the Royal Society of London. Series A. Mathematical and Physical Sciences*, *269*(1339), 500-527.

Roscoe, K. H., Schofield, A., and Wroth, A. P. (1958). On the yielding of soils. *Geotechnique*, *8*(1), 22-53.

Santamarina, J. C., & Cho, G. C. (2001). Determination of critical state parameters in sandy soils—simple procedure. *Geotechnical Testing Journal*, *24*(2), 185-192.

Schofield, A., and Wroth, P. (1968). *Critical state soil mechanics*. McGraw-Hill Book Co., London.

Taylor, D. W. (1948). *Fundamentals of soil mechanics*. John Wiley and Son, New York.

Thevanayagam, S. (2007). Intergrain contact density indices for granular mixes—I: Framework. *Earthquake Engineering and Engineering Vibration*, *6*(2), 123-134.

Wood, D. M. (1990). *Soil behaviour and critical state soil mechanics*. New York: Cambridge university press.

Wood, D. M., and Maeda, K. (2008). Changing grading of soil: effect on critical states. *Acta Geotechnica*, *3*(1), 3-14.

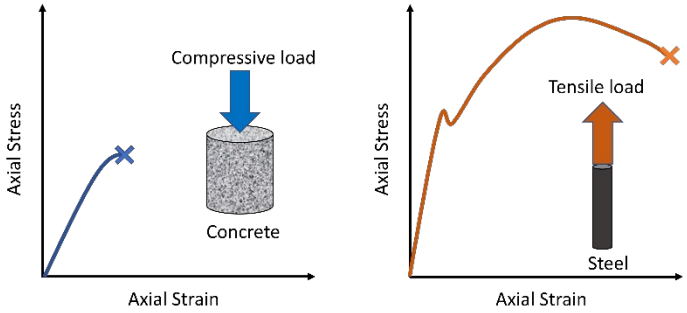

Figure 1.1: Typical load-deformation response for concrete and steel.

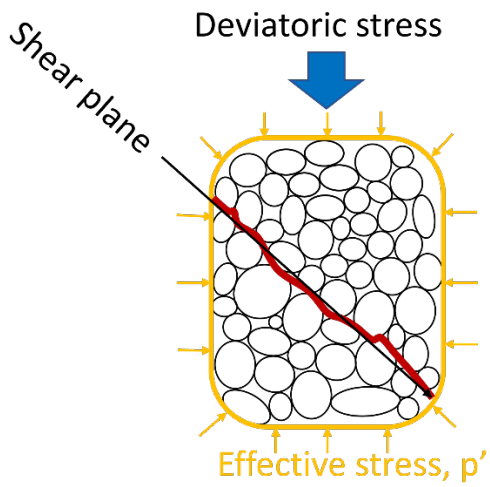

Figure 1.2: Confined particles under deviatoric stress. The inclined surface is the shear plane.

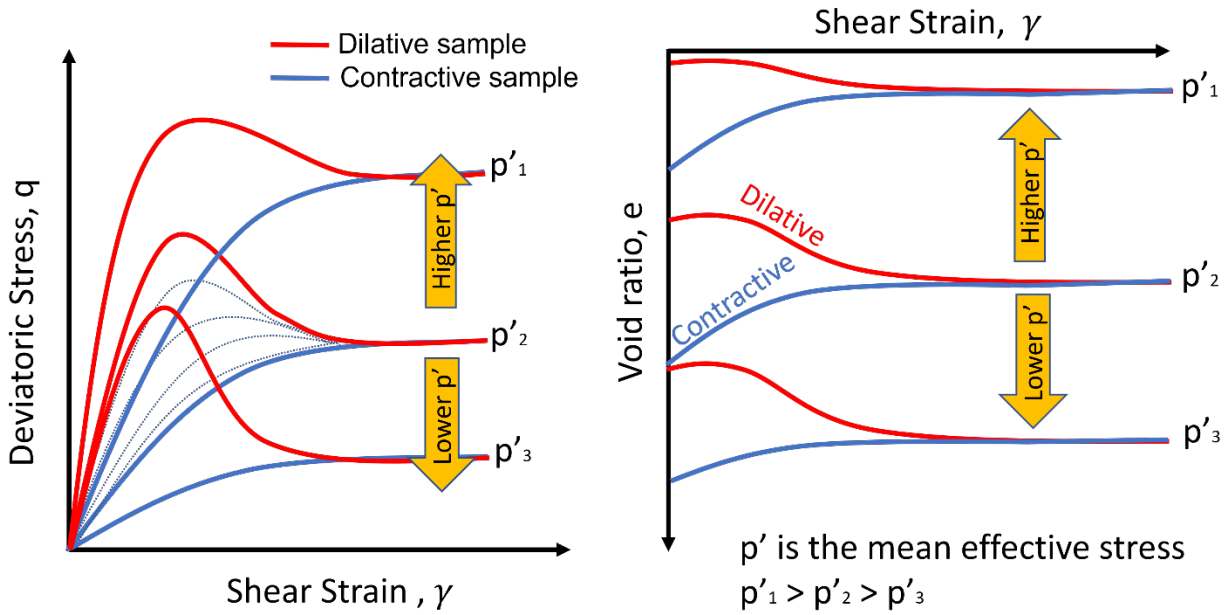

Figure 1.3: Deviatoric and void ratio progression of dense and loose samples subjected to shear strain. Dense samples dilate and experience peak shear strength. However, the dense and loose samples merge to constant shear strength and void ratio at the critical state. Higher effective stress leads to high strength and a lower void ratio at the critical state.

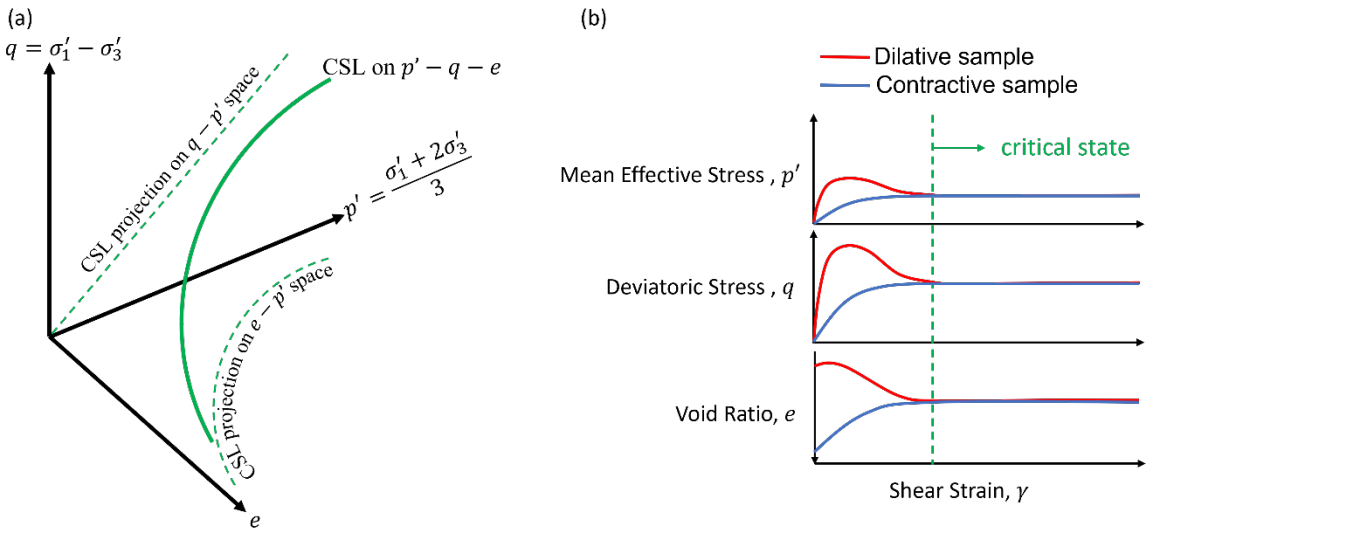

Figure 1.4: (a) a 3D representation of the critical state line and its projection onto the p'-q and p'-e spaces, (b) p', q, and e evolution with shear strain γ for dilative and contractive samples.

CHAPTER 2:

An Image Processing Algorithm for the Systematic Evaluation of the Angle of Repose and Void Ratio of Particulate Media

Ammar Mohammed Alshammari,[1,2] Dante Fratta[2]

Abstract

The angle of repose is a simple yet helpful method in evaluating particulate media's frictional response. Moreover, as multiple scientific and engineering fields are interested in the angle of repose, several testing methods have been developed. However, measurement techniques are primarily manual, and the associated packing of particles is not typically captured in the angle of repose measurements. To expand the use of these measurements, we developed a new image processing algorithm that calculates the particulate media's angle of repose and void ratio in a rotating cylinder. The algorithm uses the Radon Transform to locate the position and direction of the surface of the particulate media in the rotating cylinder so that the angle of repose and the void ratio can be estimated. Using the proposed algorithm, we assessed the repose angle and void ratio of mixtures made by crushed glass and glass beads at different volume fractions. As expected, the measured angles of repose and void ratios decrease as the glass beads' volumetric contribution increases in the mixture.

Keywords: angle of repose, void ratio, image processing, Radon transform.

[1] Department of Civil and Environmental Engineering, King Fahd University of Petroleum & Minerals, Dhahran 31261, Saudi Arabia. Email: ashammari@kfupm.edu.sa
[2] Geological Engineering, Department of Civil and Environmental Engineering, University of Wisconsin–Madison, Madison, WI 53706, USA. Email: fratta@wisc.edu

2.1. Introduction

A simple way to assess the frictional behavior of coarse-grained soils is to measure their angle of repose. As such, its measurement attracts the attention of various engineering and scientific disciplines. For example, researchers and practitioners in geotechnical engineering (Terzaghi et al., 1996), geomorphology (Kleinhans et al., 2011), drug manufacturing (Shah et al., 2008), chemical engineering (Geldart et al., 2006), granular physics (Jaeger et al., 1989), and particulate media modeling (Coetzee, 2017) use angle of repose for the evaluation of models as its measurement requires simple techniques.

Researchers have proposed several angle of repose measurement methodologies, including lifting a hollow cylinder to form a heap on a horizontal surface (Lajeunesse et al., 2004), tilting a cylinder filled with soils from the horizontal to the vertical position (Santamarina and Cho, 2001), piling particles on a round plate using a funnel (Miura et al., 1997), and rotating a horizontal partially-filled cylinder around its axis (Henein et al., 1983). However, in all these methods, the angle of repose is usually measured manually, using primarily simple visual and imaging inspections. Therefore, inconsistency and time-consuming issues are expected.

As a response to this problem, researchers implemented image processing techniques to measure the angle of repose (e.g., Frączek et al., 2007; Pirard et al., 2009; Kleinhans et al., 2011; Hu et al., 2018; Wójcik et al., 2018; Klanfar et al., 2021; Müller et al., 2021). However, those image processing methods use proprietary interpretation algorithms (Pirard et al., 2009), and are designed only for heaped particles (Frączek et al., 2007; Wójcik et al., 2018; Klanfar et al., 2021; Müller et al., 2021), or few details of the image processing are provided (Kleinhans et al., 2011; Hu et al., 2018). Furthermore, these methods do not consider the effect of density in the measurements. Nevertheless, the packing of particles is an essential property required to understand the

mechanical response of particulate materials (Jaeger and Nagel, 1992). So, adding void ratio measurements to the angle of repose of particles can enrich the analysis of particulate media behavior.

This study proposes a new imaging algorithm that uses the Radon Transform to analyze digital images and calculate the position and orientation of the surface of the particulate media in a rotating cylinder. Then, it uses that information to calculate the angle of repose and the void ratio of coarse-grained materials. Finally, to validate the methodology's performance, we test the proposed algorithm in mixtures of glass beads and crushed glass mixtures. The results show, as expected, how the angle of repose and void ratio increase as the percentage of crushed glass in the mixture increases.

2.2. The Testing Cylinder

The testing cylinder selected in this study has a length of 41 mm and an inner diameter of 51.1 mm. Two end plates cover the cylinder. To waterproof the system, the gaps between the cylinder walls and plates are sealed with O-rings and secured with three screws (Figure 2.1). We must take digital images of the particulate media within the cylinder, so we manufactured the cylinder and end caps with transparent acrylic. One of the end platens has two 3.2-mm inner diameter holes to allow for the saturation of the particulate media in the cylinder, first by flooding and then by removing large air bubbles with vacuum pressure. After removing the air bubbles from the specimen, fine hoses are placed into the 3.2-mm inner diameter holes to reduce their size and prevent particles from clogging the holes and interfering with the formation of the repose plane during the rotation of the cylinder. Then, we sealed those holes to prevent water leakages from the

cylinder. Finally, we covered the backside of the cylinder with a green liner to facilitate the image processing of the digital photographs (top photograph in Figure 2.2).

2.3. The Angle of Repose and Void Ratio Calculations

We performed the angle of repose and void ratio calculations by analyzing digital pictures of a transparent rotating cylinder with coarse-grained material inside. As the cylinder rotates, the particular media reaches failure at the angle of repose. To achieve failure, we followed several steps to prepare the material within the cylinder, bring the particulate material to the angle of repose, and capture the images. First, coarse-grained particles filled about half of the volume of the cylinder; then, we added water and saturated the particle media by applying vacuum pressure to the filled cylinder. Second, the cylinder rotates along its longitudinal axis with the saturated and submerged coarse-grained particles to form the steepest slope (i.e., the angle of repose). At the same time, a digital camera (a cellular phone's camera suffices) captures pictures perpendicular to the rotating axis, so images of the side of the slope are captured. The cylinder and the camera lens must be aligned and leveled to ensure accurate measurements of the angle of repose. Finally, the computer algorithm uses image analyses to calculate the particulate media's angle of repose and void ratio.

In the analysis of the digital images, we assume that the sloping face forms a plane, as this assumption is required for sample volume calculations. However, this assumption is potentially a source of error as past studies showed that continuously rotating particulate media might undergo segregation processes and create two different slopes on the plane perpendicular to the rotating axis (Dury et al., 1998; Ahmed et al., 2021). In addition, the void ratio calculations require that the

volume of the cylinder, the specific gravity, and the mass of the solid particles be known before testing the material. The following paragraphs describe the components of the testing and measurement setup.

The Image Processing Algorithm. The proposed algorithm calculates the angle of repose and void ratio of coarse-grained soils by analyzing digital images of the particulate media as the transparent cylinder rotates clockwise (the direction of rotation is specified for using the algorithm presented in the Appendix). The interpretation of the images assumes that the angle of the sloping surface (ϕ_{AoR}) is a proxy for the critical state friction angle (ϕ'_{cs}) (Cornforth, 1973; Bolton, 1986). The algorithm uses the Radon Transform, and Figure 2.2 documents the sequence of steps executed to determine the angle of repose.

- **Input Parameters:** Table 2.1 summarizes the input parameters required for the calculations, including the internal volume of the cylinder, the specific gravity and mass of the solid particles, and the tolerance for the angle of repose calculations.

- **Cylinder Mask:** A binary mask is required to isolate regions of interest in the digital image (Gonzalez and Woods, 2018). During the masking process, the algorithm uses color analyses to select the region of interest and then sets pixels' values to one in the region of interest and zero for the remaining pixels. So, we implemented a masking process to detect the inner diameter of the cylinder (i.e., the space that accommodates the coarse-grained soil). Figure 2.3 documents the steps performed by the algorithm to develop the cylinder mask for the captured images.

    1. *Foreground segmentation and adaptive thresholding.* The original image is mapped into a grayscale representation. Then, a foreground segmentation (i.e., an image processing method used to extract foreground objects from the background) detects the

black O-ring that seals the gap between the cylinder and the end plates. This process assigns different threshold values to each pixel based on color variation across the image (Bradley and Roth, 2007). In addition, adaptive thresholding separates the foreground (i.e., cylinder face) from the background. So, the algorithm uses two different adaptive foreground thresholds. First, a dark adaptive threshold delineates the O-ring as the dark area in the foreground. Second, a bright threshold detects the area in the foreground. We first apply both adaptive thresholds to produce binary images where the O-ring is white (the second row in Figure 2.3—each threshold detects the O-ring on the image quite well). However, spots around the O-ring might also be present, as different adaptive thresholds might identify some features incorrectly. To reduce this problem, we implemented the element-by-element multiplication of the two thresholded O-ring binary images. This element-by-element multiplication of two equal-sized matrices, X and Y, is:

$$X \odot Y = \begin{bmatrix} x_{11} & x_{12} & x_{13} \\ x_{21} & x_{22} & x_{23} \\ x_{31} & x_{32} & x_{33} \end{bmatrix} \odot \begin{bmatrix} y_{11} & y_{12} & y_{13} \\ y_{21} & y_{22} & y_{23} \\ y_{31} & y_{32} & y_{33} \end{bmatrix} = \begin{bmatrix} x_{11} * y_{11} & x_{12} * y_{12} & x_{13} * y_{13} \\ x_{21} * y_{21} & x_{22} * y_{22} & x_{23} * y_{23} \\ x_{31} * y_{31} & x_{32} * y_{32} & x_{33} * y_{33} \end{bmatrix}$$

This way, the detected noisy objects in one adaptive threshold but not in the other will have pixel values equal to one and zero, respectively. So, the product of these two pixels is a zero-value pixel, removing most of the spurious spots around the O-ring.

2. *Erosion.* We filled the area bounded by the O-ring, but this area is larger than the area occupied by the particulate media. To resolve this issue, we fit the inner diameter of the cylinder by *eroding* the area between the O-ring and the cylinder's inner diameter, as shown in Figure 2.4. Erosion is an image morphology operation that converts

boundary pixels in foreground objects into background pixels (Jain, 1989). As a result, we shrink the foreground object. The eroded pixels are determined by:

$$EP = \left(1 - \frac{r_{inner}}{r_{O-ring}}\right) r_{O-ring-pixels}$$

where r_{inner} and $r_{O\text{-}ring}$ are the radii of the inner circle of the cylinder and the O-ring, and $r_{O\text{-}ring\text{-}pixels}$ is the radius of the O-ring expressed in the number of pixels. The ratio of inner circle radius to O-ring radius is known based on the geometry of the testing cylinder. For the $r_{O\text{-}ring\text{-}pixels}$, the algorithm calculates the length in pixels.

- **Pre-processing the material under the slope:** We now have the image of the inner cylinder, but we still need to determine the area occupied by the particulate material. So, the eroded mask image is applied to the original image to crop the original image into just the area of interest for analysis, the masked cylinder in Figure 2.5. This color image of the particulate material is composed of red, green, and blue (RBG)-color channels. Splitting the image into images with the RBG color tones facilitates the detection of features (Lucchese and Mitra, 2001; Garcia-Lamont et al., 2018). For example, the masked cylinder image in Figure 2.5 was split into the three RBG channels. So, each color channel image represents the intensity of the corresponding color. Splitting those channels creates three grayscale images with pixel values ranging between 0 and 255 depending on the intensity of each color. Because different channels distinguish the material from the background much better than other color channels, the algorithm calculates pixels summation in each color channel to detect the best-performing channel. The best-performing channel yields the minimum value in the summation of the pixel values as the background areas have low pixel values (that is, the red channel in the example presented in Figure 2.5). This channel

is then binarized using a global threshold to present the material under the slope with white color. The one-and-zero image shows some noisy background features, such as the small holes on the back platen and small objects above the slope. However, those features do not generally affect slope calculations, but they can still be filtered before performing the void ratio calculations.

- **The Angle of Repose Calculations:** We implemented the Radon Transform to estimate the angle of repose from the measurements. The Radon transform computes projections of the binary image at specific orientation angles (θ). The projection is the sum of the pixel values along parallel lines (Santamarina and Fratta 2005). The angles of interest range from $0°$ to $90°$ with the angle increment ($\Delta\theta$) in the input parameters. We defined the angle increment as the tolerance of the measurements. Finer tolerances in the measurements increase the accuracy of the results and the computational cost. Therefore, we assigned $\Delta\theta$ to be $0.1°$ as a compromise between tolerance and computation time. MATLAB calculates the Radon transform of the first angle and moves counterclockwise to calculate the following angle. In this way, one of the Radon transforms is perpendicular to the slope of particles. Figure 2.6 summarizes the Radon transforms of the binary image and their first derivatives. The Radon transform projection perpendicular to the slope of the particles appears as a dotted green line. The algorithm detects the slope of the particulate media in the cylinder by taking the first derivatives of all Radon transforms and finding the projection with the minimum value of its derivative. The lowest minimum derivative of the Radon transforms stands for the transform perpendicular to the slope (Figure 2.7). At this perpendicular Radon transform, the image intensity (i.e., the pixels count) drops sharply at

the slope's edge (Figure 2.6). Therefore, the complement angle to the projection with the lowest minimum derivative of the Radon transform is ϕ_{AoR}.

- **The Void Ratio Calculations:** The binary image produced at the end of Figure 2.5 is rotated clockwise at an angle complementary to the angle of repose. This rotation aligns the slope in the vertical direction (Figure 2.8). Next, the algorithm calculates the Radon transform at $\theta = 0°$ and its first derivative to locate the slope's column vector. The location of the minimum value coincides with the column vector of the slope. Then, the algorithm removes any spots above the slope (i.e., the right side of the vertical slope in the rotated binary image in Figure 2.8). The summation of the white pixels in the resulting image represents the area of the particulate material in the digital image. Then, the algorithm divides the area of the particulate material by the area of the eroded mask cylinder in Figure 2.3 to obtain the occupied area ratio of the specimen. This ratio is the same as the particulate material volume (V) to the cylinder volume (V_{cyl}) ratio if the repose's slope is constant along the length of the cylinder. Finally, knowing solid particles' volume, the void ratio can be estimated (i.e., $e = \frac{V - V_s}{V_s}$).

- **The Line Along the Slope:** Figure 2.9 shows the steps required for drawing a line along the slope of the particulate material. First, we rotate the grayscale image as we did with the binary image in Figure 2.8. We use the column vector of the vertical slope to draw a line along the slope. The algorithm changes the pixel values of that vector to 255 to generate a straight line representing the slope. Next, we increase the line's width by adding the adjacent column vectors to plot the line to facilitate plotting the slope line. Finally, the algorithm rotates the image back to its original position. Image rotation creates a black box that outlines the image. The algorithm filters out this box and presents only the grayscale

image with a white line along the slope. Drawing the line along the slope helps interpret the data and validates the quality of the calculated results.

2.4. Material Testing

We evaluated the algorithm against a set of particulate media using the cylinder and the imaging setup. Table 2.2 shows the properties of glass beads and crushed glass used to prepare the binary mixtures. Each material was sieved, and we only used material passing sieve #30 and retained by sieve #35. As a result, the particles have uniform sizes (with a coefficient of uniformity $C_u = 1.1$ and a mean particle size $D_{50} = 0.548$ mm). Furthermore, the roundness and aspect ratio of the mono-sized particles were determined using the image analysis approach proposed by Zheng and Hryciw (2015). At least 35 particles of the glass beads and 112 particles of the crushed glass were analyzed to get the average and standard deviation of particle shape parameters.

We then mixed the mono-sized particles using volumetric fractions to create six different mixtures. We started with 100% glass beads; then sequentially replaced 20% of glass beads volume with the crushed glass to prepare a total of six mixtures. Table 2.3 presents the matrix of the mixtures and their angle of repose and void ratio measurements. While testing, the cylinder was rotated slowly and stopped to take digital images of the slope at repose. Then, the rotation was resumed to form new slopes for the following measurements. Thirty images of each mixture were analyzed to get the average value and standard deviation of the repose angle and void ratio measurements.

Figure 2.10 shows the mixtures' angle of repose and void ratio variation. Unsurprisingly both properties decrease as the volume of glass beads increases. The friction angle of particles increases as particle shape deviates from the spherical shape (e.g., Cho et al., 2006; Binaree et al., 2019).

Cho et al. (2006) conducted a wide angle of repose experiment to evaluate the effect of roundness on the critical state friction angle. They suggested that the critical state friction angle is $\phi_{cr} = 42 - 17R$, where R is the roundness of the particles. When applying this relation to the roundness values of the glass beads and crushed glass in Table 2.2, we found 25.85° and 37.58°, respectively. These values are comparable to the measured angle of repose values, $25.62° \pm 0.41°$ and $36.66° \pm 0.76°$ for glass beads and crushed glass. The void ratio measurements also agree with the expected behavior of particle packing. The angular particles create a higher void ratio than rounded particles (Youd, 1973). The highest measured void ratio is for pure crushed glass and decreases as glass beads volume increases in the mixture.

2.5. Testing Challenges and Limitations

While we tested several situations to evaluate and validate the proposed methodology and results, we must discuss potential challenges and testing limitations. We identified three potential issues: boundary conditions (i.e., the effect of friction against the walls on the measured angle of repose), segregation (i.e., the separation of different particles due to density, size, and shape in the testing cylinder), and color contrast (i.e., identification of different particle material color against the cylinder background). The following paragraphs discuss the three potential issues and proposed conditions and procedures to reduce their effects.

Boundary conditions. Researchers have studied boundary conditions on the dynamic angle of repose measurements using a rotating cylinder (e.g., Dury et al. 1988). Those studies assessed the effect of small side walls' friction, rotational speeds, cylinder diameter/length ratio, and cylinder diameter/particle size ratio on the measured dynamic angle of repose. Dury's research team used

glass beads and muster seeds to represent different particle sizes and shapes in the tested media. While our proposed methodology does not continuously rotate the cylinder, as we intend to measure the static angle of repose, the results by Dury et al. inform the challenges in our tests.

Dury et al. (1988) noted that the boundary effects reduce at lower rotational speeds (i.e., below 8 rpm), and that effect reaches zero as the rotational velocity decreases. However, they also modeled different angles of repose at different sections along the length of the cylinder (with lower angles at the center of the cylinder), indicating that side fraction influences the results. Please note that we assumed in our analyses for the angle of repose and void ratio calculations that the slope formed by the particulate media is plane surface.

So to evaluate the effect of the smooth boundary on the results on our pseudo-static rotations, we performed a thought experiment. As we would measure the angle of repose on the plane against the cylinder end and if the smooth boundary controls the response, the angle along the boundary would be lower than the angle of repose (dashed) than at the center of the cylinder (solid line—Figure 2.11). In that case, the digital image on boundary observation will show a slope projection showing a no-constant slope (green line on the right sketch). However, we did not observe this phenomenon in our images, so we should expect that boundary effects are smaller than the resolution of our observations and do not influence our angle of repose results.

Segregation. The user should consider particle segregation while using the proposed methodology. That is because particle segregation may affect the angle of repose and void ratio calculations, and particles of different densities, sizes, and shapes tend to segregate in rotating cylinders (Khakhar et al., 1997; Pereira and Cleary, 2017; Gray, 2018). To control this problem, the user should manually shake the cylinder to mix the particles to avoid segregation after making each angle of repose measurements. Then, slowly rotate (< 8 rpm as recommended by Dury et al. 1988), the

cylinder until the angle of repose forms. At that point, take the digital images of the slope before particles segregate. These recommendations are important because even with a few cylinder rotations, some of our specimens showed segregation. For example, during the testing of binary glass beads mixture made of 40% solid volume of D_{50} = 0.922 mm and 60% solid volume of D_{50} = 0.230 mm, we photographed situations where segregation was observed (Figure 2.12).

Color contrast. It is also essential to maintain color contrast between the material and background. For example, we utilized a green liner in the background of the cylinder. However, if the particles are green, we do not expect the algorithm to separate the material from the algorithm. Therefore, we should use a different liner color in the background, and the RBG channels analysis should be able to separate the material from the background (Figure 2.2).

2.6. Conclusions

We developed an imaging algorithm to automatically evaluate the particulate materials' angle of repose and void ratio in a rotating cylinder. The algorithm was coded into MATLAB, a commonly used programming language. We discussed details including image processing, the angle of repose and void ratio calculations, and drawing a straight line along the slope as an output. The algorithm's main points are:

- Program inputs include cylinder volume, specific gravity, the mass of the dry soil particles, and tolerance of angle of repose calculations.
- The sloping surface of the particles is assumed to be a plane, which means that the angle of repose is assumed constant across the sloping surface.

- The angle of repose is calculated using the Radon transforms of the binary images of the sloping particles. First, the Radon transform perpendicular to the slope is detected by taking the first derivatives of the Radon transforms and then identifying the minimum value of these derivatives.
- The void ratio is estimated by first calculating the area ratio between material under the slope and the cylinder's inner circle. Second, multiplying this ratio by cylinder volume to get total volume of particulte material. Finally, knowing solid partilces volume, void ratio can be calcuated.
- The algorithm draws a line along the slope as an output, so the user can validate the quality of calcutions.
- The algorithm is tested against mixtures made by combining different fractions of same-size glass beads and crushed glass. Presumptively, the measured angle of repose and void ratio increase with glass beads fraction in the mixture.

2.7. Acknowledgments

The King Fahd University of Petroleum and Minerals (KFUPM) scholarship through the Saudi Arabian Cultural Mission (SACM) and financial support from the Wisconsin Department of Transportation (WisDOT) supported this research.

2.8. References

Ahmed, E. M., Govender, I., & Mainza, A. (2021). The geometric axial surface profiles of granular flows in rotating drums. *Journal of the Southern African Institute of Mining and Metallurgy*, *121*(5), 261-265.

Binaree, T., Preechawuttipong, I., and Azéma, E. (2019). Effects of particle shape mixture on strength and structure of sheared granular materials. *Physical Review E*, *100*(1), 012904.

Bolton, M. D. (1986). The strength and dilatancy of sands. *Géotechnique*, 36(1), 65-78.

Bradley, D., and Roth, G. (2007). Adaptive thresholding using the integral image. *Journal of Graphics Tools*, 12(2), 13-21.

Coetzee, C. J. (2017). Calibration of the discrete element method. *Powder Technology*, 310, 104-142.

Cho, G. C., Dodds, J., and Santamarina, J. C. (2006). Particle shape effects on packing density, stiffness, and strength: natural and crushed sands. *Journal of Geotechnical and Geoenvironmental Engineering*, *132*(5), 591-602.

Cornforth, D. H. (1973). Prediction of Drained Strength of Sands from Relative Density Measurements. In *Evaluation of relative density and its role in geotechnical projects involving cohesionless soils*, Edited by R.S. Ladd, ASTM STP 523, American Society for Testing and Materials, Philadelphia, p. 281–303.

Dury, C. M., Ristow, G. H., Moss, J. L., and Nakagawa, M. (1998). Boundary effects on the angle of repose in rotating cylinders. *Physical Review E*, *57*(4), 4491.

Gonzalez, R. C., and Woods, R. E. (2018). Digital image processing. Pearson.

Gray, J. M. N. T. (2018). Particle segregation in dense granular flows. *Annual review of fluid mechanics*, *50*, 407-433.

Frączek, J., Złobecki, A., and Zemanek, J. (2007). Assessment of angle of repose of granular plant material using computer image analysis. *Journal of Food Engineering*, 83(1), 17-22.

Garcia-Lamont, F., Cervantes, J., López, A., and Rodriguez, L. (2018). Segmentation of images by color features: A survey. *Neurocomputing*, 292, 1-27.

Geldart, D., Abdullah, E. C., Hassanpour, A., Nwoke, L. C., and Wouters, I. J. C. P. (2006). Characterization of powder flowability using measurement of angle of repose. *China Particuology*, 4(3-4), 104-107.

Henein, H., Brimacombe, J. K., & Watkinson, A. P. (1983). Experimental study of transverse bed motion in rotary kilns. *Metallurgical Transactions B*, *14*(2), 191-205.

Hu, Z., Liu, X., and Wu, W. (2018). Study of the critical angles of granular material in rotary drums aimed for fast DEM model calibration. *Powder Technology*, 340, 563-569.

Jaeger, H. M., and Nagel, S. R. (1992). Physics of the granular state. *Science*, 255(5051), 1523-1531.

Jaeger, H. M., Liu, C. H., and Nagel, S. R. (1989). Relaxation at the angle of repose. *Physical Review Letters*, 62(1), 40.

Jain, A. K. (1989). *Fundamentals of digital image processing*. Prentice-Hall, Inc.

Khakhar, D. V., McCarthy, J. J., and Ottino, J. M. (1997). Radial segregation of granular mixtures in rotating cylinders. *Physics of Fluids*, *9*(12), 3600-3614.

Klanfar, M., Korman, T., Domitrović, D., and Herceg, V. (2021). Testing the novel method for angle of repose measurement based on area-weighted average slope of a triangular mesh. *Powder Technology*, 387, 396-405.

Kleinhans, M. G., Markies, H., De Vet, S. J., and Postema, F. N. (2011). Static and dynamic angles of repose in loose granular materials under reduced gravity. *Journal of Geophysical Research: Planets*, 116(E11).

Lajeunesse, E., Mangeney-Castelnau, A., & Vilotte, J. P. (2004). Spreading of a granular mass on a horizontal plane. *Physics of Fluids*, *16*(7), 2371-2381.

Lucchese, L., and Mitra, S. K. (2001). Colour image segmentation: a state-of-the-art survey. *Proceedings-Indian National Science Academy Part A*, 67(2), 207-222.

Miura, K., Maeda, K., & Toki, S. (1997). Method of measurement for the angle of repose of sands. *Soils and Foundations*, *37*(2), 89-96.

Müller, D., Fimbinger, E., and Brand, C. (2021). Algorithm for the determination of the angle of repose in bulk material analysis. *Powder Technology*, 383, 598-605.

Pereira, G. G., and Cleary, P. W. (2017). Segregation due to particle shape of a granular mixture in a slowly rotating tumbler. *Granular Matter*, *19*(2), 1-12.

Pirard, S. L., Lumay, G., Vandewalle, N., and Pirard, J. P. (2009). Motion of carbon nanotubes in a rotating drum: The dynamic angle of repose and a bed behavior diagram. *Chemical Engineering Journal*, *146*(1), 143-147.

Santamarina, J. C., and Cho, G. C. (2001). Determination of Critical State Parameters in Sandy Soils—Simple Procedure. *Geotechnical Testing Journal*, 24(2), 185–192.

Santamarina, J. C., and Fratta, D. (2005). *Discrete Signals and Inverse Problems*. Wiley & Sons. 350 pages.

Shah, R. B., Tawakkul, M. A., and Khan, M. A. (2008). Comparative evaluation of flow for pharmaceutical powders and granules. *Aaps Pharmscitech*, 9(1), 250-258.

Terzaghi, K., Peck, R. B., and Mesri, G. (1996). *Soil mechanics in engineering practice*. John Wiley & Sons.

Wójcik, A., Klapa, P., Mitka, B., and Sładek, J. (2018). The use of the photogrammetric method for measurement of the repose angle of granular materials. *Measurement*, 115, 19-26.

Youd, T. L. (1973). Factors controlling maximum and minimum densities of sands. Evaluation of Relative Density and its Role in Geotechnical Projects Involving Cohesionless Soils. In STP523-EB *Evaluation of relative density and its role in geotechnical projects involving cohesionless soils*, Edited by R.S. Ladd, ASTM STP 523, American Society for Testing and Materials, Philadelphia, ASTM, 98-112.

Zheng, J., and Hryciw, R. D. (2015). Traditional soil particle sphericity, roundness and surface roughness by computational geometry. *Géotechnique*, 65(6), 494-506.

Table 2.1: Parameters needed for volumetric calculations.

Assumptions	Algorithm Inputs	Algorithm Outputs
• The slope along the plane of repose is constant. • The angle of repose ϕ_{AoR} is a proxy for the critical state friction angle ϕ_{CS}	• The internal volume of the cylinder $V_{cylinder}$ • The specific gravity of the solid particles G_s • The mass of the solid particles M_s • Digital image perpendicular to the cylinder axis of rotation • Calculation tolerance	• The angle of repose ϕAoR • Particulate material volume V • Solid particle volume V_s • Average void ratio e = (V-Vs)/Vs

Table 2.2: Size and particle shape properties of the mono-sized particles.

Material		**Glass beads**	**Crushed glass**
Sieve # (passed-retained)		30-35	30-35
Mean particle size, D_{50} (mm)		0.548	0.548
Specific gravity, G_s		2.49	2.51
Number of particles tested for particle shape		35	112
Roundness	**Average**	0.95	0.26
	SD	0.12	0.11
Aspect ratio	**Average**	0.96	0.65
	SD	0.09	0.16

Table 2.3: Angle of repose and void ratio results of two sets of binary mixtures. The first six are binary size mixtures, and the last six are binary shape mixtures.

Material	**Glass beads**	**Crushed glass**	**The angle of repose, ϕ_{AoR} (°)**		**Void ratio, e (-)**	
D_{50} (mm)	**0.548**	**0.548**	**Average**	**SD**	**Average**	**SD**
Volume fraction	**100%**	**0%**	36.66	0.76	1.13	0.03
	80%	**20%**	33.78	1.01	1.07	0.03
	60%	**40%**	30.64	1.26	0.94	0.03
	40%	**60%**	28.24	0.85	0.90	0.03
	20%	**80%**	27.21	0.68	0.81	0.03
	0%	**100%**	25.62	0.41	0.69	0.03

Figure 2.1 The transparent testing cylinder is filled with the coarse-grained particulate media and water. The inset shows the holes captured from the side in contact with the material.

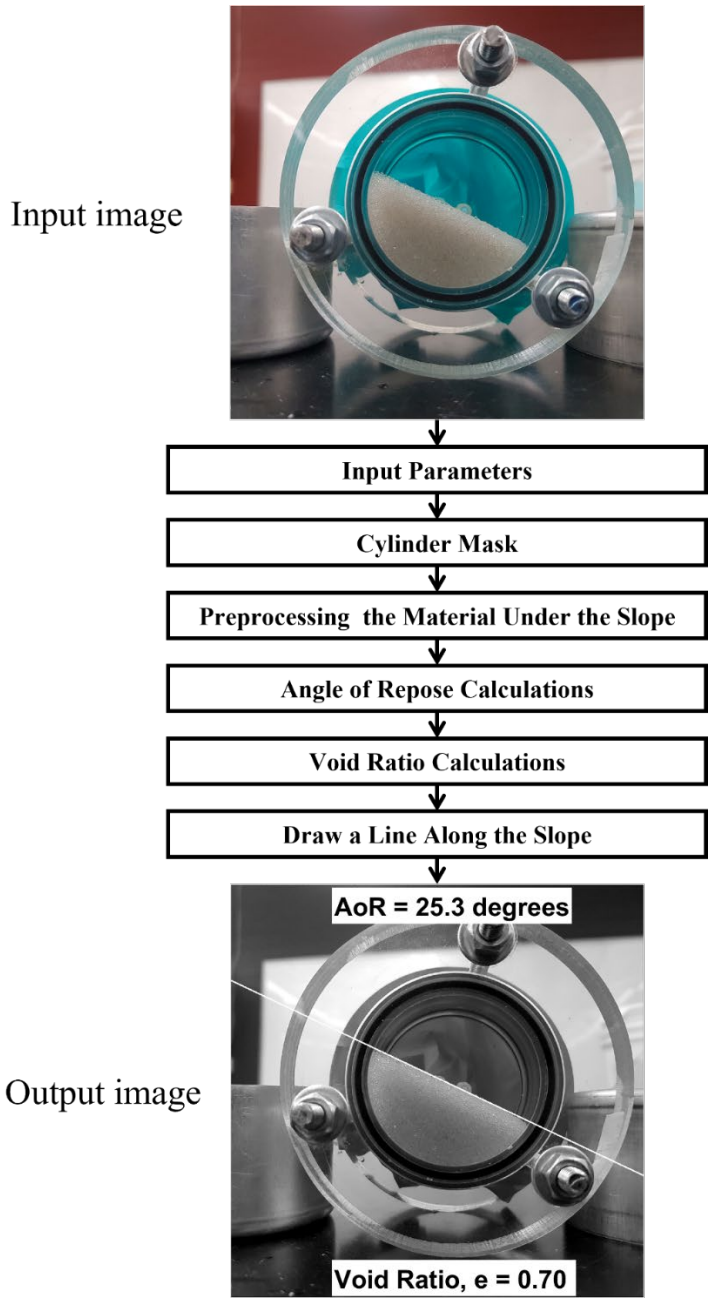

Figure 2.2: Steps for the angle of repose and void ratio calculations.

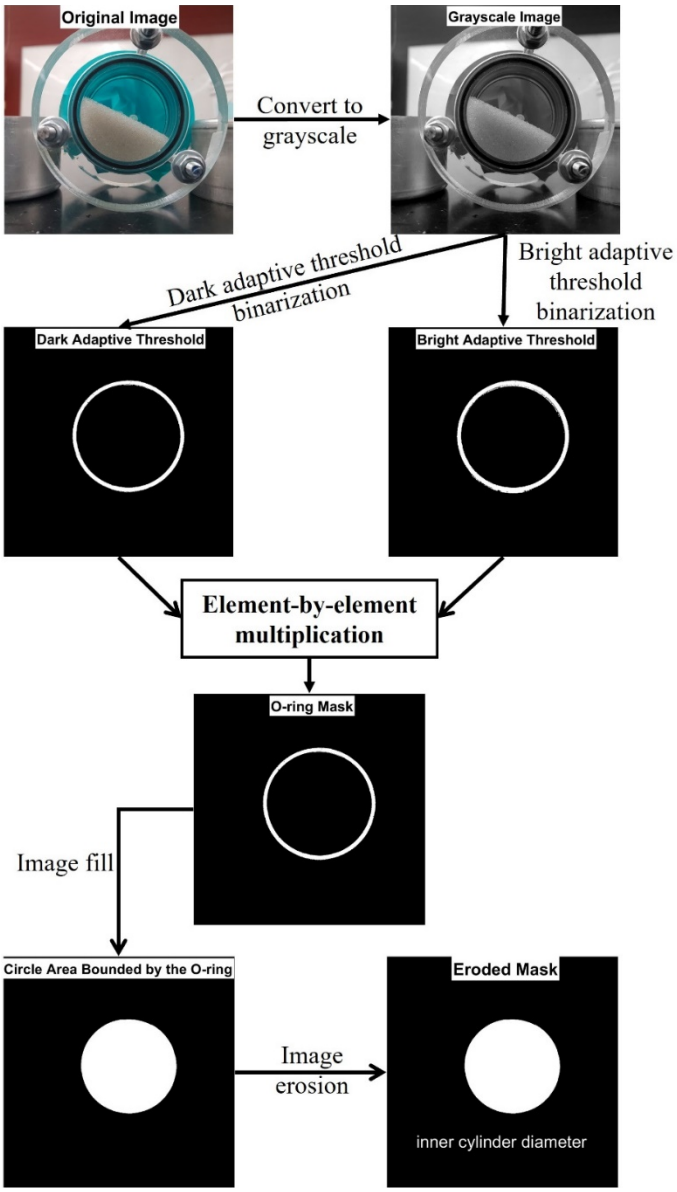

Figure 2.3: Cylinder mask creation processes.

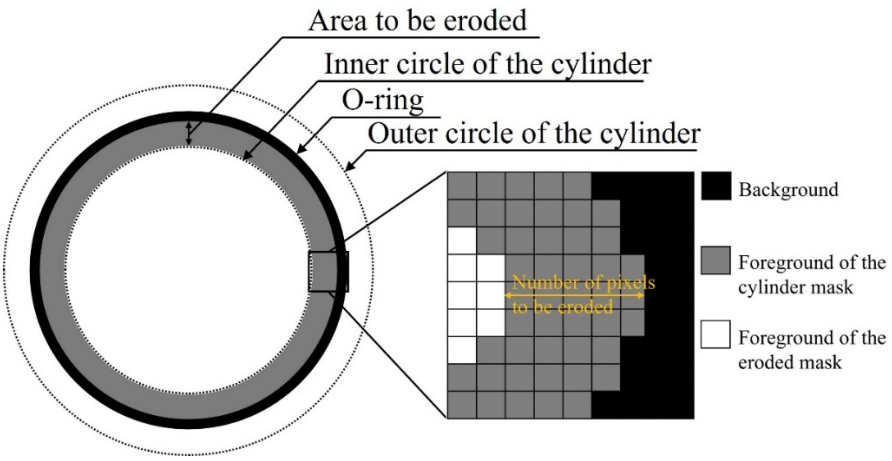

Figure 2.4: Eroded area between the inner circle and the O-ring.

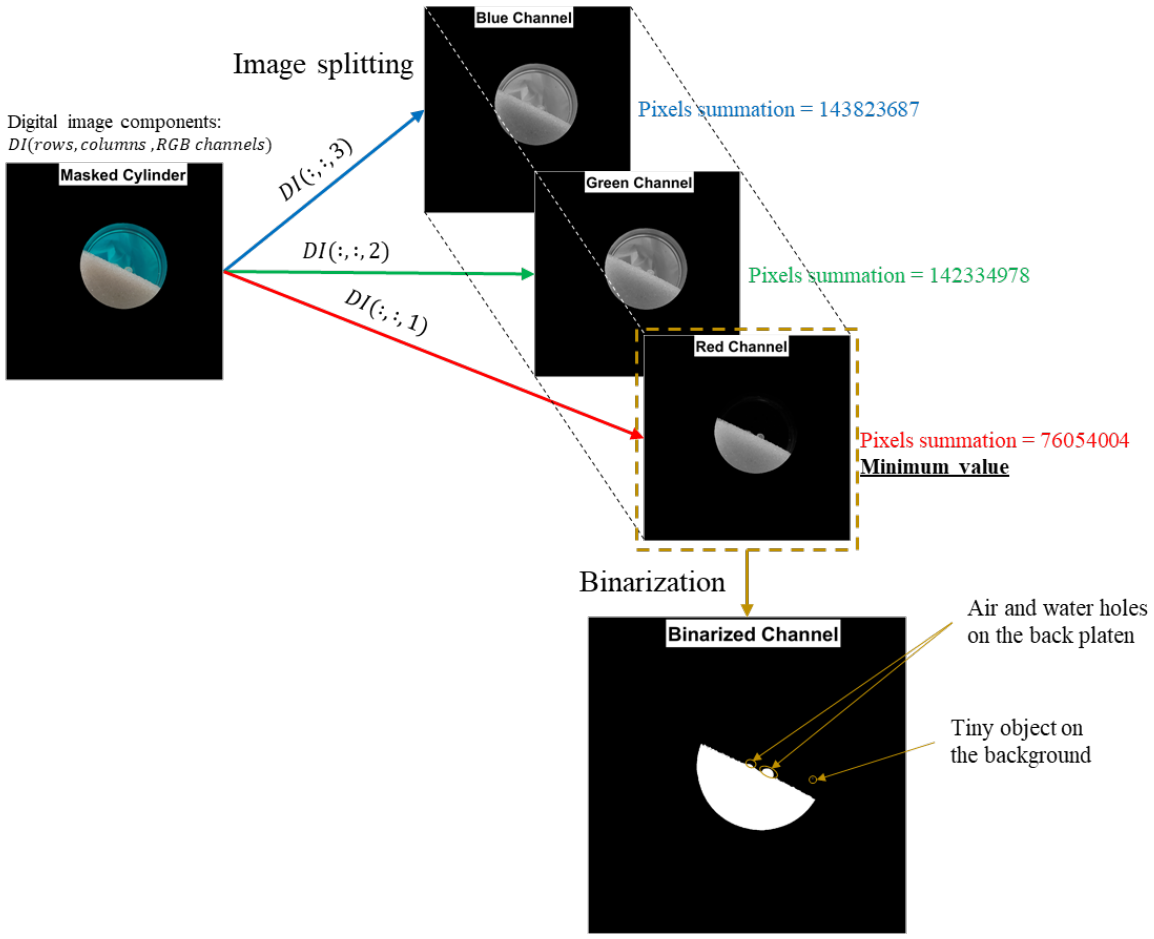

Figure 2.5: Pre-processing of the material under the slope.

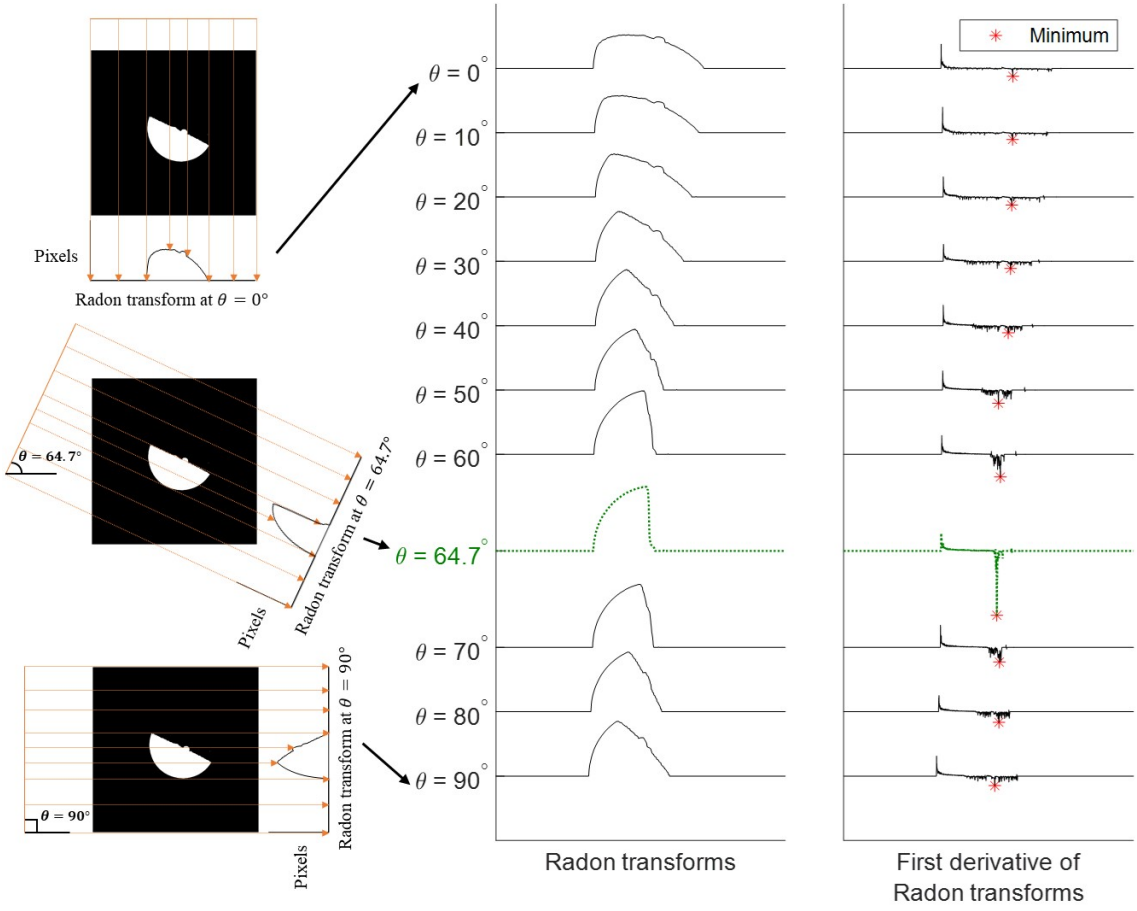

Figure 2.6: The Radon transforms of the binary image and their first derivatives. The dotted green line corresponds to the transform perpendicular to the slope of the material.

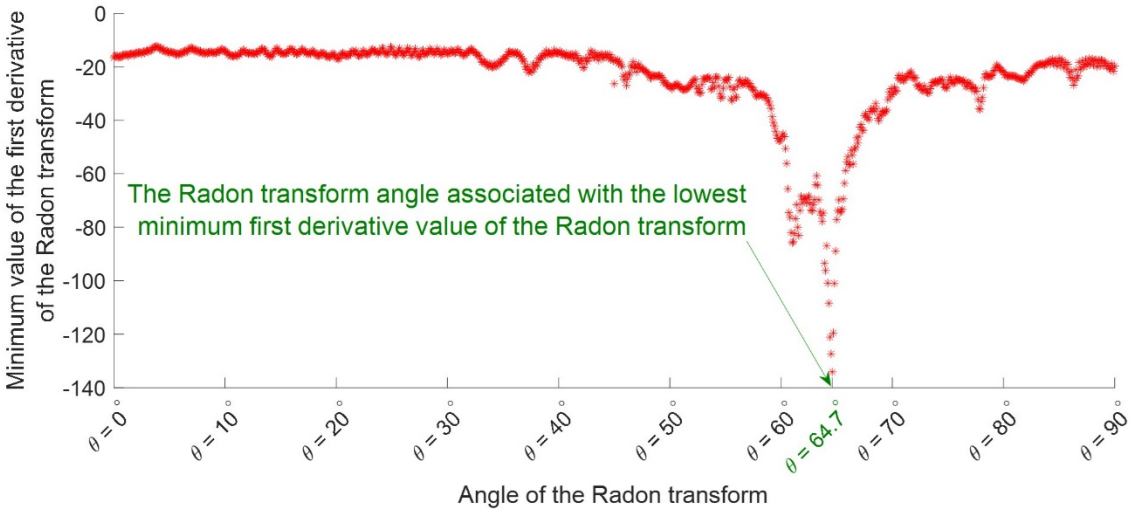

Figure 2.7: Minimum values of the Radon transform value versus the projection angle.

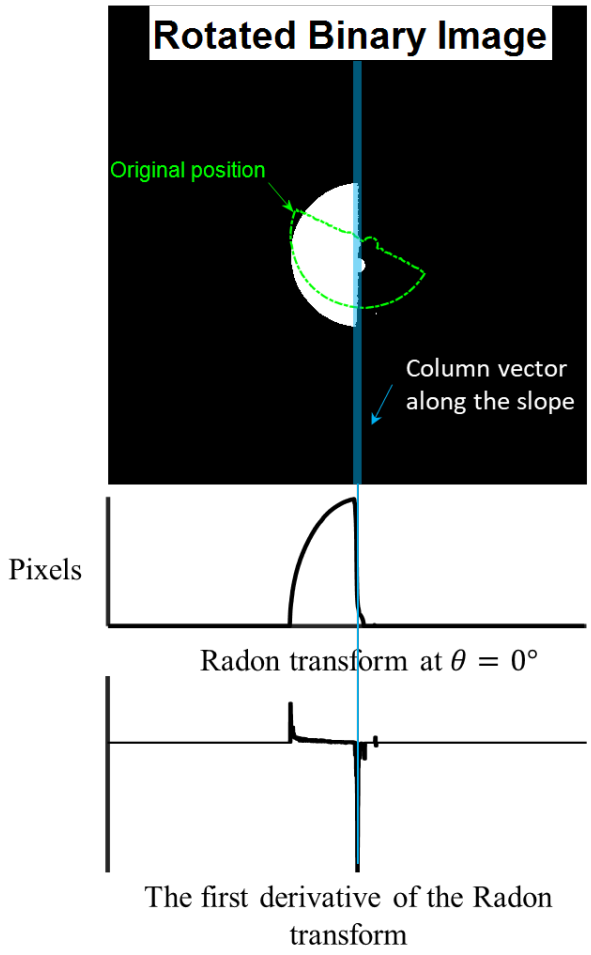

Figure 2.8: Rotated binary image with the Rando transform and the first derivative to determine the slope vector.

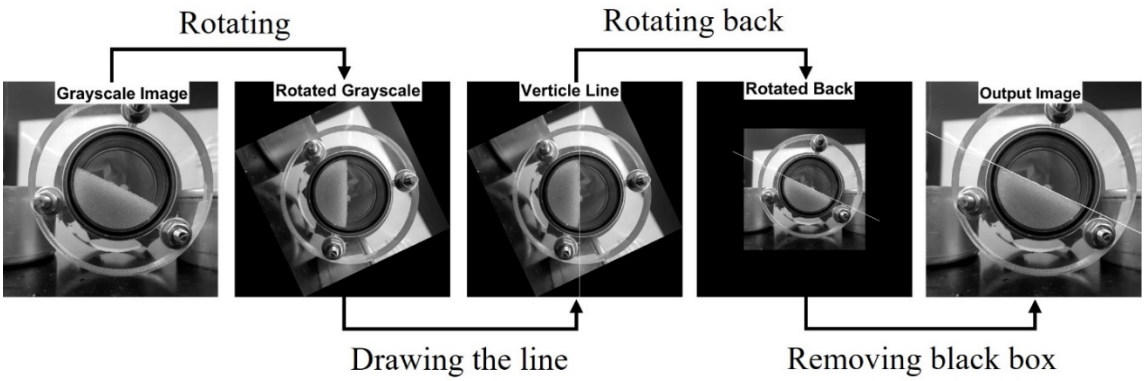

Figure 2.9: Steps of drawing a line along the slope.

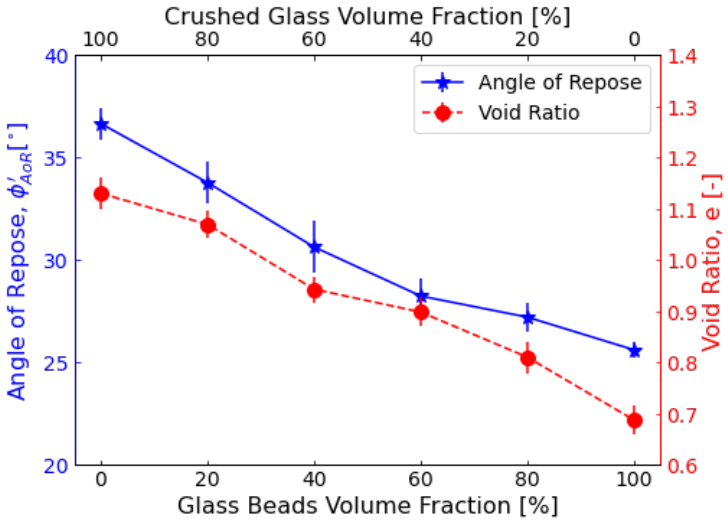

Figure 2.10: Angle of repose and void ratio measurements of binary shape mixtures (D_{50} = 0.548 mm).

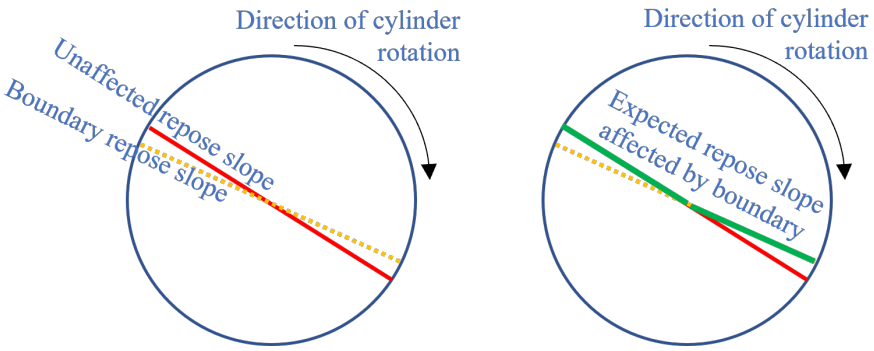

Figure 2.11: Expected boundary effect on the measurements.

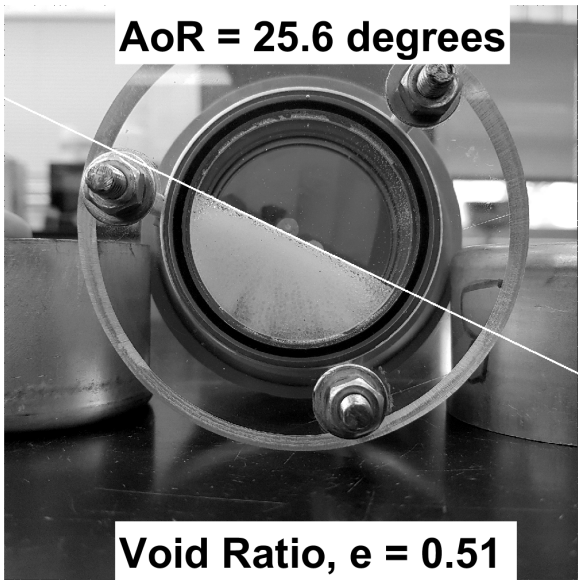

Figure 2.12: Glass beads binary mixture made of 40% solid volume of D_{50} = 0.922 and 60% solid volume of D_{50} = 0.230 mm. The large-size particles are dark, and the small-size particles are white.

2.9. Appendix: Matlab Script

```
%% Input parameters
V_cyl = 83.72;                  % cylinder volume
G_s = 2.49;                     % Specific gravity of solid particles
M_s = 56;                       % mass of solid particles
tol_deg = 0.1;                  % tolerance of angle measurement
(degree)
%% Read and Preprocess Original Image
I_o=imread('15.jpg');           % Read original image
I_GS = rgb2gray(I_o);           % Convert image to grayscale
I_GS = imadjust(I_GS);          % Adjust image to increase contrast
%% Cylinder Mask
[imheight, imwidth] = size(I_GS); % Image size
% Cylinder size in the image is greater than one-third of the image
width
cir_size = 1/3*imwidth;
% Dark adaprive threshold mask
I_BW_dark = imbinarize(I_GS, 'adaptive', 'Sensitivity', 0,
'ForegroundPolarity', 'dark');
dark_mask = bwpropfilt(~I_BW_dark, 'MinorAxisLength', [cir_size,
Inf]);
% Bright adaptive threshold mask
I_BW_bright = imbinarize(I_GS, 'adaptive', 'Sensitivity', 1,
'ForegroundPolarity', 'bright');
bright_mask = bwpropfilt(~I_BW_bright, 'MinorAxisLength', [cir_size,
Inf]);
% The O-ring mask
Oring_mask = dark_mask.*bright_mask;
% cylinder mask
Cyl_mask = imfill(Oring_mask, 'holes')-Oring_mask;
% To filter tiny holes on the image
Cyl_mask = imopen(Cyl_mask, strel('disk', 3));
% The mask need to be eroded to fit the inner circle of the cylinder
% The ratio between the inner and O-ring raduis
ratio = 25.55/28;
% The number of pixels to be eroded
EP = 0.5*(1-ratio)*regionprops(Cyl_mask,
'MajorAxisLength').MajorAxisLength;
% Eroded mask
Eroded_mask = imerode (Cyl_mask, strel('disk',round(EP),8));
Cyl_area = sum(sum(Eroded_mask)); % Area of the inner circle in pixels
% Applying the eroded mask on the original image
Cyl = I_o.*uint8(Eroded_mask);
%% Preprocessing for the material inside the cylinder
% Split image into RGB channels
[r,g,b] = imsplit(Cyl);
% Calculation of pixels summation for each channel
r_in = sum(r,[1,2]);        % Red channel
g_in = sum(g,[1,2]);        % Green channel
```

```
b_in = sum(b,[1,2]);        % Blue channel
% The minimum value stands for color channel with highest contrast
% Index of color channel with highest contrast
[~,ind_HC] = min([r_in g_in b_in]);
% Cyl grayscale with the color of highest contrast
Cyl_HC = Cyl(:,:,ind_HC);
% Binarize the image of highest color contrast
Cyl_BW = imbinarize(Cyl_HC);
Cyl_BW = imfill(Cyl_BW, 'holes');
%% Repose angle
% The Radon transform is applied to Cyl_BW with theta increment equals
to the measurement tolerance
Cyl_radon = radon(Cyl_BW, [0:tol_deg:90]);
% each vector in Cyl_radon is differentiated and the minimum 1st
% derivative is calculated. Then, the index of vector with the lowest
value of
% 1st derivative stands for repose angle.
[~,ind_min]=min(min(diff(Cyl_radon)));
Com_angle = ind_min*tol_deg;   % Complementary angle of the angle of
repose
Repose_angle = 90-Com_angle;% The angle of repose
%% Calculate the Area and Draw a Line Along the Slope
% Rotate I_GS to make the slope vertical
I_rotate = imrotate(I_GS,Repose_angle-90);
% Two images are copied out of I_rotate for two purposes
I_box = I_rotate;   % To remove black box created by image rotation
I_slope = I_rotate; % To draw a line along the slope
% Rotating the I_box back to the original position.
I_box = imrotate(I_box,90-Repose_angle);
% To find indices of black columns and rows
black_col = find(sum(I_box)==0);       % Indices of columns
black_row = find(sum(I_box,2)==0);     % Indices of rows
% To draw a line along the slope
I_line = imrotate(Cyl_BW,Repose_angle-90); % Find vector index of the
slope
[~, s_line] = min((diff(sum(I_line))));    % Vector index of the
I_slope
I_slope(:, s_line-5:s_line+5) = 255;       % A white line along the
slope
% Rotate the image to back to the origin
I_slope = imrotate(I_slope,90-Repose_angle);
% Remove the black box around I_slope
I_slope(:,black_col)=[];
I_slope(black_row,:)=[];
% To calculate the area of material under the slope
I_area = I_line;
I_area(:,s_line+1:end) = 0;
I_area = imrotate(I_area,90-Repose_angle);
% Remove the black box around I_area
I_area(:,black_col)=[];
I_area(black_row,:)=[];
% fill holes in the material area
```

```
I_area = imfill(I_area, 'holes');
mat_area = sum(sum(I_area)); % material area in pixel
%% Void Ratio Calculations
area_ratio = mat_area/Cyl_area; % Material to cylinder area ratio
V_mat = V_cyl*area_ratio;       % Volume of material under the slope
V_solid = M_s /G_s;             % Solid volume
e = (V_mat-V_solid)/V_solid;    % Void ratio of material

figure
imshow(I_slope)
hold on
title_x = size(I_o,1)/4; % x-coordinate for title
title_y = 155;                  % y-coordinate for title
text(title_x, title_y, sprintf('AoR = %1.1f degrees', Repose_angle),
...
'Color', 'k', 'FontSize', 35, 'fontweight','bold','BackgroundColor',[1
1 1])
text(title_x, title_y+2730, sprintf('Void Ratio, e = %1.2f ', e), ...
'Color', 'k', 'FontSize', 35, 'fontweight','bold','BackgroundColor',[1
1 1])
hold off
```

CHAPTER 3:

The Combined Effect of Gradation and Particle Shape on Coarse-Grained Soils' Critical State Friction Angle

Ammar Mohammed Alshammari[3,4], Dante Fratta[4]

Abstract

We present a systematic experimental study to evaluate grain size and particle shape's combined effect on coarse-grained particulate media's critical state friction angle. The goal is to understand and characterize the ultimate shear strength of the coarse-grained soils based on particles' properties. We mixed five uniform particle ranges of glass beads (GB) and crushed glass (CG) to make 56 mono-sized, bi-sized, or poly-sized testing mixtures. We then used an imaging algorithm to calculate the angle of repose in a rotating cylinder to assess the critical state friction angle. Measurement results show that the critical state friction angle is higher for mixtures created by combining CG and GB of the same size fraction; however, the critical state friction angle decreases if the GB fraction increases. The results of bi-sized and poly-sized mixtures made of one particle type reveal a negligible effect of GSD on the critical state friction angle. However, if bi-sized and poly-sized mixtures include different particle types, the small size fraction controls the measured critical state friction angle. Finally, we proposed and tested different definitions of roundness for mixtures to capture the contribution of different particle shapes and responses to the measurements. We defined equivalent roundness based on the volume of the size fractions, the

[3] Department of Civil and Environmental Engineering, King Fahd University of Petroleum & Minerals, Dhahran 31261, Saudi Arabia. Email: ashammari@kfupm.edu.sa
[4] Geological Engineering, Department of Civil and Environmental Engineering, University of Wisconsin–Madison, Madison, WI 53706, USA. Email: fratta@wisc.edu

number of particles in each size fraction, and the surface area of the size fractions. All equivalent roundness definitions produced comparable correlations with the critical state friction angle. However, the equivalent roundness definition based on the surface area yields the highest correlation coefficients for the proposed models.

Keywords: Angle of repose, roundness, bi-sized, poly-sized, relative size effect, grain size distribution.

3.1. Introduction

The goal of soil classification systems is for engineers to capture soil responses by assessing readily available characteristics of the soil samples (Casagrande, 1948; Terzaghi et al., 1996; Holtz et al., 2011; Kovačević et al., 2018). Grain size distribution (GSD) is the most common index property used in the Unified Soil Classification System (USCS) when determining whether soils have fine-grained or coarse-grained soil characteristics (Park and Santamarina, 2017). For example, if the mean particle size (D_{50}) is larger than 0.075 mm, the soil is classified as coarse-grained; otherwise, the soil is classified as fine-grained. Atterberg limits provide insight into fine-grained soils by assessing how the particles interact with water. This soil-water interaction is measured as the water content corresponding to specific undrained shear strengths (1.7 kPa for liquid limit and 170 kPa for plastic limit—Worth and Wood, 1978). Moreover, the frictional response of fine-grained soils can be estimated based on the Atterberg limit measurements (Ladd et al., 1977; Santamarina and Shin, 2009).

For coarse-grained soils, the GSD captures the effect of the dominant particle size (i.e., coarse or fine) and gradation (i.e., poor, well, or gap-graded) as a means to assess how soils would behave as filters (FEMA, 2011) or how well they would retain water under unsaturated conditions (Fredlund, 1997). However, the current soil classification systems tell engineers little about frictional response and, therefore, the shear strength of coarse-grained soils. For these reasons, coarse-grained soil index parameters are not used in geotechnical strength analysis such as bearing capacity, slope stability, or earth retaining structures calculations. So, an in-depth understanding of the index properties related to shear strength parameters can lead to predictive models to better estimate soils' ultimate shear strength, which is of utmost importance.

One issue is that GSD parameters alone do not provide information on soils' critical state friction angle ϕ_{cr} (Li et al., 2013; Nguyen et al., 2015; Cantor et al., 2018; Jiang et al., 2018; Yang and Luo, 2018). Nevertheless, Simoni and Houlsby (2006) and Igwe et al. (2007) documented how GSD characteristics influence critical state friction angles. Their observations could be attributed to different particle shapes among different particle size fractions on the same soil. For example, the particle shape of the fine fractions of soils can increase or decrease the critical state friction angle if the fine particle shape is angular or rounded, respectively (Yang and Wei, 2012). Still, those characteristics are not fully captured in the parameters collected in the USCS.

The particle shape's significance on soil behavior has been known for over 70 years (Casagrande, 1948; Taylor, 1948; Terzaghi et al., 1996). However, despite its importance, particle shape was only visually assessed with qualitative descriptors (ASTM D2488-17, 2017). More recently, with the ability to quantify particle shape descriptors, researchers correlated particle shape with the frictional behavior of coarse-grained soils, but primarily for uniform soils (Cho et al., 2006; Yang and Luo, 2015; Altuhafi et al., 2016; Suh et al., 2017; Xiao et al., 2019). The results and correlations presented in those studies show a relationship between critical state friction angles and particle shape parameters. However, the quality of these correlations is more robust when the tested materials are uniform (e.g., Suh et al., 2017; Xiao et al., 2019). However, Cho et al. (2006) and Altuhafi et al. (2016) tested materials that were not necessarily uniform, and their correlations showed a large scatter. This scatter could be attributed to the different particle shapes among different particle size fractions.

In this study, we explore the combined effect of particle shape and GSD of coarse-grained soils on the critical state friction angle. We tested rounded glass beads (GB) and angular crushed glass (CG) of different sizes in different particulate mixtures. For multi-sized particle systems, we

hypothesize that the particle shape of large-size particle fractions contributes more to the frictional response than the small-size particle fractions. We support our hypothesis on the concept that larger particles have greater coordination numbers and carry most of the load chains than smaller particle fractions (Wood and Maeda, 2008; Nguyen et al., 2015; Cantor et al., 2018; 2020). However, increasing small particles might significantly alter the interactions between larger particles (Thevanayagam, 2007), potentially changing how the different fractions interact and control the observed friction angle. We begin with a revision of relevant topics, including the frictional behavior of coarse-grained soils; the influence of coarse-grained index properties on the frictional response. Then, we describe the experimental materials and methods and discuss the test results. We noted that the particle shape effect on the critical state friction angle increases as the particles' relative size becomes smaller. We ascribe this behavior to the ability of the small-size particles to cover the large-size particles and mask the interactions between them. This ability improves as the volume of small-size particles increases.

3.2. Frictional Behavior of Coarse-grained Soils

The frictional behavior of soils is a complex phenomenon, and the parameter that defines it, the friction angle, is generally not an intrinsic property of soils (Bolton, 1986; Santamarina and Shin, 2009). The issue is that there is not a single definition of friction angle. Furthermore, those definitions depend on shear strain levels and other factors. These other factors include particle's hardness and shape, grain size distribution, strain rate, and boundary conditions (i.e., confining effective stress, drainage, temperature, and vibration—Santamarina and Shin, 2009).

Different strength conditions occur when soils undergo shear deformations; therefore, defining different friction angles. For example, dense soils under low effective stresses develop a peak shear strength during volumetric expansion, followed by a constant volume strength. Thus, the peak shear strength yields the peak friction (ϕ_p), while the constant volume strength defines the constant volume friction angle (ϕ_{cs}). The constant volume strength is also called the critical state (i.e., soils undergo shear deformation under constant void ratio, shear stress, and effective stress—Schofield and Wroth, 1968). Santamarina and Shin (2009) described the critical state as the statistical balance between dilation and contraction of the particulate media under the high shear strain range.

In contrast, the peak friction angle (ϕ_p) is the aggregation of constant volume strength and dilatancy (Bolton, 1986). Hence, the peak friction angle equals the constant volume friction angle when the soil does not undergo dilation. However, some particulate materials have friction angles that emerge at strain levels beyond the constant volume shear strength: residual and post-segregation. For example, residual shear strength tends to appear in elongated (e.g., rice—Aloufi and Santamarina, 1995) or plate-like (e.g., mica and clays) particles at large shear strains when the particles align in the direction of the shear plane. The resulting friction angle is the residual friction angle (ϕ_r), which is less than the constant volume friction angle when particles are elongated or plate-like or equal to the constant volume friction for spherical or cubical particles (Lee et al., 2007; Wood, 1990).

Under strain larger than the strain required to develop residual shear strength, particulate media may also segregate particles with different shapes (Lee et al., 2007) or densities and sizes (Savage and Lun, 1988). During segregation, a new particulate media fabric forms yielding the post-segregation shear strength and the associated post-segregation friction angle (ϕ_{ps}). This friction angle is less than or equal to the residual friction angle. Therefore, to prevent post-segregation

friction angle, soil remixing should be enabled (Lee et al., 2007). Figure 3.1 sketches the shear response of a particulate material as shear strain increases and the progression of the different friction angles: $\phi_p \geq \phi_{cs} \geq \phi_r \geq \phi_{ps}$.

3.3. Index Parameters and Frictional Response of Soils

Soil properties can be intrinsic (e.g., mineral composition, shape, grain size, critical state friction angle) or conditional (e.g., void ratio, moisture content, and peak friction angle) (Mitchell and Soga, 2005). Intrinsic properties are less likely to change upon external factors. Therefore, it is more rational to correlate frictional strengths with intrinsic properties. Moreover, intrinsic properties such as shape and GSD could be obtained while characterizing soils and particulate media.

3.3.1. The effect of mineralogy

Quartz, mica, pyroxenes, and amphiboles are common minerals in coarse-grained soils (Mitchell and Soga, 2005). While quartz is the most common mineral in coarse-grained soils, other minerals are also important in the characterization and interpretation of the mechanical behavior of soils. Carbonate minerals like calcite and dolomite dominate sea sediments, while semiarid and arid area soils contain sulfate minerals; tropical areas contain iron and aluminum oxides (Mitchell and Soga, 2005). Nevertheless, the shear strength of soils is seldom controlled solely by their mineralogy. Although, Terzaghi et al. (1996) provided ranges of sliding friction angles ($\emptyset'_\mu$) for common minerals, the peak and critical state friction angles are more complex parameters controlled by properties beyond just the sliding between mineral surfaces (Santamarina et al., 2001; Santamarina

and Shin, 2009). For example, quartz's critical state friction angle varies within a wide range, leading to inaccurate predictions of soil strength based solely on mineralogy. For example, Bolton (1986) assigned 33º as a fair estimate of the critical state friction angle for quarzitic sands with a marginal error of 2º. However, Ottawa #20/30 sand (quarzitic fluvial sand) possesses a critical state friction angle as low as 27º (Cho et al., 2006), and weathered sandstone sand has a critical state friction angle as high as 36.4º (sample # P3-S5 in Bareither et al., 2008). So, not only mineralogy but also particle shape is essential in assessing the shear strength of soils. Thus, establishing a frictional response of soils based solely on the mineralogy could be unreliable.

3.3.2. The effect of the grain size distribution

GSD is a valuable property for predicting soil engineering properties like hydraulic conductivity (Alyamani and Sen, 1993; Odong, 2007), soil-water characteristic curve (Fredlund et al., 1997), void ratio ranges (Cubrinovski and Ishihara, 2002), critical state line on e-log(p') plane (Chang and Deng, 2020), and stiffness (Wichtmann et al., 2011). However, the GSD does not directly affect the critical state friction angle (Li et al., 2013; Nguyen et al., 2015; Cantor et al., 2018 and 2020; Jiang et al., 2018; Yang and Luo, 2018). To understand how GSD does not control the critical state friction angle, one must recall the microstructural components of shear strength (i.e., contact orientations and contact forces in particle assembly). The friction angle captures the summation of contact and force anisotropy coefficients (Rothenburg and Bathurst, 1989). As the grain size distribution becomes more well graded, the contact anisotropy decreases, and the normal force anisotropy increases to maintain a constant friction angle (Nguyen et al., 2015; Cantor et al., 2018 and 2020).

3.3.3. The effect of the particle shape

Coarse-grained soils possess different particle shapes and sizes due to mineralogy, weathering mechanisms, and formation processes (Santamarina and Cho, 2004). Three independent scales describe the shapes of coarse-grained particles: roughness, roundness, and sphericity (Figure 3.2a - Barrett, 1980; Santamarina and Cho, 2004; Mitchell and Soga, 2005). Roughness captures the smallest of the descriptors' scales, and it represents surface smoothness. However, roughness measurements are problematic due to the fractal nature of the particles. So, the roughness scale is inconclusive (Santamarina and Cho, 2004). Roundness is an intermediate descriptor scale that reflects particle corners' sharpness. Figure 3.2b shows the numerical definition of roundness: the average of radii of circles fitted in the particles' major features divided by the radius of the maximum inscribed circle. The roundness value is one for well-rounded particles, decreasing with increasing particles' angularity. Finally, sphericity depicts the global form of the particle. Table 3.1 compiles five definitions of sphericity. For those sphericity definitions, a sphere has a value of one, and the value decreases with particle elongation. Among these definitions, the aspect ratio sphericity (S_{AR}) appears to be genuinely independent of roundness (Zheng and Hryciw, 2015).

The roughness descriptor does not appear to control particulate media's critical state friction angle based on experimental observations of roughened spheres (Cavarretta et al., 2010; Tapia et al., 2019). Cavarretta et al. (2010) suggested that regular contact forces flatten the roughened surface, alleviating the roughness effect. However, roundness and sphericity are much more relevant for characterizing soils' critical state friction angle (Cho et al., 2006; Yang and Luo, 2015; Altuhafi et al., 2016; Suh et al., 2017; Xiao et al., 2019). Micromechanical considerations indicate that the reduction in roundness or sphericity values enhances the interlocking between particles, increases

stress anisotropy, and favors the dilation in soils. Thus, higher shear strength appears with the reduction in roundness or sphericity (Cho et al., 2006).

3.4. Materials and Methods

This research aims to evaluate the combined effect of particle shape and GSD on the critical state friction angle. First, we evaluate the effect of particle shape and GSD independent of each other; then, we combine their effects. Therefore, we include testing materials that are variable in particle shape but have constant gradation, variable in gradation but have constant particle shape, and graded with variable particle shape among different particle sizes. Finally, we maintain parameters and conditions consistent for all materials.

3.4.1. Material

GB and CG particles are the two materials we mix to develop 56 different particulate mixtures for our experimental program. Since CG is a recycled material and it contains impurities. So, to remove those impurities, we washed it in a bleach solution and then rinsed it thoroughly with deionized water. We then sieved the GB and CG through consecutive sieve sizes to prepare five uniform particle ranges. In this way, each of the retained materials on sieves has a coefficient of uniformity (C_u) equal to 1.1. Table 3.2 documents the particle size, shape, and specific gravity (G_s) of the uniform GB and CG particles tested. To create the 56 particle mixtures, we combined different particle ranges on volumetric fractions.

3.4.2. Particle shape measurement

We performed particle shape measurements using an image processing technique. As GB and CG particles are transparent materials, image processing techniques must be conditioned to detect the particle boundaries from digital images. So, we laid the particles on a glass plate while illuminating the plate from underneath to reduce the boundary detection problem of the transparent particles. Then a digital camera, Dino-Lite Pro Digital Microscope, was placed over the particles to capture images of the particles' silhouette. This imaging method helps eliminate the shadows of the particles in the background, which was documented as a problem when particles are imaged on a white background (Kumara et al., 2012). Using the captured images, we calculated the roundness and aspect ratio using the computational geometry algorithm that Zheng and Hryciw (2015) developed. We used images of 85 and 35 particles for the CG and GB to develop measurement statistics. Table 3.3 lists the averages and standard deviations of roundness and aspect ratio for the two different sets of particles.

The average particle shape descriptor, e.g., roundness, represents the particle shape descriptor of the whole particulate material (e.g., Cho et al., 2006; Bareither et al., 2008; Cavarretta et al., 2010; Suh et al., 2017). So, intuitively, the shape descriptor of a mixture composed by mixing two fractions of different particle types is the fraction-weighted average of their particle shape descriptor. Yang and Wei (2012) proposed this approach to calculate the combined roundness. However, while correlating the combined roundness to the critical state friction angle, different models, material dependent, were developed (Yang and Wei, 2012). Unlike Cho et al. (2006)'s model based on roundness regardless of soil type, Yang and Wei (2012) provided two models for two different grains of sand, Toyoura and Fujian, mixed with fines. Thus, the fraction-weight average to calculate the roundness of the particulate mixture does not account for the relative size

effect of the mixed particles. In Section 6, we proposed and evaluated different approaches to calculate mixture equivalent roundness while the effect of the relative size is considered.

3.4.3. The angle of repose measurement

The angle of repose is a fair estimate of the critical state friction angle (Cornforth, 1973; Bolton, 1986; Santamarina and Cho, 2001). However, different testing methods of the angle of repose could yield different measurements owing primarily to particle segregation (Rousé, 2014). Lee et al. (2007) tested the angle of repose of sand-mica mixtures using a tilting container and rotating cylinder. Particle segregation degrades the measured friction angle in the titling container, but a rotating cylinder compels particle remixing and helps eliminate the effect of particle segregation. So, we adopted the rotating cylinder method to measure the particulate mixtures' angle of repose. Capillary and electrostatic forces may also affect the measurements of the angle of repose, especially for fine particles (Santamarina and Cho, 2001; Kleinhans et al., 2011). Therefore, we saturated the testing cylinder by adding water and vacuuming the air through tiny holes in one side of the testing cylinder.

We used a transparent plexiglass cylinder with 51.1 mm inner diameter and 41 mm length for our tests. While testing, we manually and slowly rotated the cylinder. We frequently stopped the rotation to capture the digital images of the formed slopes across the end cap. We maintained the tested cylinder, and the digital camera leveled and aligned to capture slope images adequately. We captured 30 digital images of the slopes to calculate the statistics of the measured angle of repose of all the different mixtures. We developed an imaging algorithm to calculate the angle of repose and void ratio from images of sloping particles in the rotating cylinder (please refer to Alshammari and Fratta (2023) for details of the image processing algorithm).

3.5. Results and Interpretation

Table 3.2 documents the properties of the GB and CG particles we used to create the 56 mono-sized, bi-sized, and poly-sized mixtures. The mono-sized mixtures consist of one uniform material or a combination of the same size range of CG and GB. We mixed two uniform sizes of GB, CG, or a combination of both for the bi-sized mixtures. Finally, the poly-sized mixtures correspond to three or five different size ranges of GB or CG particles. In the three-sized mixtures, the mean particle sizes of the composing particles are 0.922 mm, 0.548 mm, and 0.326 mm, and each size shares 33.3% of the mixture volume. While for the five-sized mixtures, we mixed a 20% of volumetric fraction of each uniform particle size range. We created the three- and five-sized mixtures to evaluate the contribution of particles' relative size and shape in the angle of repose. Figure 3.3 presents the matrix of the combination of all the mixtures tested in our program.

3.5.1. Mono-sized mixtures

We tested mono-sized mixtures to evaluate the effect of particle shape alone. Figure 3.4 presents the measured critical state friction angle results as a function of roundness. These results are compared to the data from Cho et al. (2006). The scatter in our study's mono-size critical state friction angle is smaller than Cho et al.'s data. The scatter difference could be attributed to two reasons: (1) the image analysis of Cho et al. was semi-quantitative (i.e., Cho et al. used chars to estimate the particle shapes); and (2) the materials presented in Cho et al. were not necessarily uniform. Therefore, the variation of particle shapes among different particle sizes is expected.

Nevertheless, the mono-sized glass bead mixtures attained similar void ratios (first five mixtures in Figure 3.3). Similarly, the void ratios of the mono-sized CG mixtures are also relatively constant regardless of the mean particle size (mixtures six to ten in Figure 3.3). However, the void ratio of the crashed glass mixtures is larger than those of the mono-sized GB mixtures. Youd (1973) investigated the packing of rounded and angular particulate systems and reported that rounded particles achieve denser packings than angular particles.

We prepared other mono-sized mixtures by keeping the particle size constant but mixing different particle shape proportions. For example, we sequentially replaced 20% of CG volume with GB while keeping the same mean particle size D_{50} = 0.548 mm. Figure 3.5 documents how increasing the mixtures' angularity controls the critical state friction angle and void ratio. The critical state friction angle and void ratio decrease as the volumetric content of the GB increases in the mixture. However, decreasing the critical state friction angle requires only a small percentage of GB. For example, 20% of the GB lowers the critical state friction angle by about 3°, whereas 20% of the CG increases the critical state friction angle by about 1.5°. Yang and Wei (2012) and Wei and Yang (2014) also noted the effect of rounded particle vs. angular particle interaction on particulate media's critical state frictional response. First, Yang and Wei (2012) tested the effect of adding fine crushed silica and GB, where both have approximate GSD and specific gravity to uniform sands. They observed that GB altered the critical state friction angle more than the crushed silica. Then, Yang and Wei (2012) explained their observations by the preferential rolling movement of fine-grained GB over coarse-grained particles when the coarse-grained particles are also rounded. In contrast, fine angular particles prefer sliding over coarse-grained particles.

However, by looking at the data reported by Yang and Wei (2012) and Wei and Yang (2014), we noted that the uniform sands are not the same size, and the effect of fines is more pronounced on

the large-size uniform sand. We also observed that while the GSDs for the crushed silica and GB fines obtained by sieving are similar, laser diffraction methods report a slight difference in particle size measurements for the crushed silica particles. Probably the elongation of the crushed silica particles made GSD measurements by the two methods to be different. Those observations made us reevaluate the CG, and GB particle sizes postulated to have the same mean particle size. For example, Figure 3.6 shows pictures of different CG and GB between sieves No. 30 and No. 35 (i.e., D_{50} = 0.548 mm). The pictures show the principal and intermediate axes of the particles; however, the dimension of the minor axis is not captured as it is perpendicular to the pictures' plane. However, the minor axis dimension is needed to calculate the particles' volumes.

Furthermore, the intermediate axis controls the passing particles through the sieve opening, while the major axis of the particle is not as important (Kumara et al., 2012; Ohm and Hryciw, 2013). As a result, particles with a smaller aspect ratio (i.e., the major axis is larger than the intermediate axis) can be larger than the sizes described by sieve analyses. So, we evaluated the particle volume of thirty-five pairs made of the GB and CG retained between sieves No. 30 and 35. We captured silhouettes of the pairs at two projections. First, the particles are rested naturally on a surface to form the maximum area. Then, we carefully rolled the particles on their used side using a spatula and a pin rod. Figure 3.7 shows three samples of the silhouettes taken for volume calculations. The particles are assumed to be ellipsoids for volume calculations, and we used MATLAB imaging capabilities to obtain the dimensions. The intermediate and minor axes are the minimum particle axes in the naturally rested and rolled particle. The major axis is the maximum particle axis of both projections. Figure 3.7 shows that the GB particles have identical axes in both projections, while CG particles show a clear difference between the intermediate and minor axes. We estimated the particle's volume by approximating the particles to ellipsoids:

$$V_{particle} = \frac{\pi}{6} d_1 d_2 d_3 \quad (5)$$

where d_1, d_2, and d_3 are major, intermediate, and minor diameters. Table 3.3 summarizes the volume calculation of thirty-five CG and GB pairs. The average volume of CG particles is 1.9 greater than the average volume of GB particles. Moreover, the variation of particles' volumes is more in CG particles than in GB. Therefore, the size difference between the two particles can explain the dominance of GB over the CG on frictional response. We evaluate the effect of different particle sizes in the following two sections.

3.5.2. Bi-sized mixtures

We made bi-sized mixtures by combining two sets of different uniform-size particles. One group of the bi-sized mixtures contains different particle shapes to evaluate the effect of relative particle size on the critical state friction angle and packing. We also composed another group of only one particle shape to isolate the effect of particle shape on the measurements. Figure 3.8 shows the variation of the critical state friction angle and void ratio of the bi-sized mixtures that combine two different shapes and particle sizes. The critical state friction angle decreases with increasing GB volume. However, the rate of change of the critical state friction angle depends on the ratio of the mean particle size of the CG and GB. The smaller the CG size fraction, the greater the control it has over the critical state friction angle. When the CG fraction becomes larger than the GB, the GB fraction controls the critical state friction angle. The solid line in Figure 3.8 represents particles having the same mean particle size; however, CG particles are larger than GB, as discussed in the previous section. The void ratio decreases with the increase of GB volume fraction, yet the effect of relative particle size is not as significant as it is in the case of critical state friction angle.

Figure 3.9 presents the data of binary GB or CG mixtures. Variation of particle sizes has a negligible effect on the critical state friction angle. For the bi-sized CG mixtures, a minor increase in the critical state friction angle at 100% fraction of the larger particles because they have a slightly lower roundness value. That is, if the particle shape is identical, the particle size variation does not affect the measurement of the critical state friction angle (Li et al., 2013; Nguyen et al., 2015; Cantor et al., 2018; Jiang et al., 2018; Yang and Luo, 2018). However, the void ratio is sensitive to particle size gradation (Youd, 1973). Figure 3.9 shows that the void ratio variation decreases when the fraction of the fine particles increases. Then, at a point between 60% and 80% of the small particle fraction, the void ratio increases to match the void ratio of the fine particles. This behavior is more pronounced when the size difference between coarse and fine particles increases.

Previous research on the extreme void ratios of binary mixtures showed similar behavior, but the threshold of the small-size fraction to hit the lowest void ratio is less than 40% (Lade et al., 1998; Cubrinovski and Ishihara, 2002; Thevanayagam, 2007; Fuggle et al., 2014; Chang et al., 2015). We carefully assessed the images taken for the angle of repose and noted non-homogeneities in the material under the slope. In Figure 3.10, large particles are darker than small particles, and particle segregation manifests as the small-size fraction increases. The particle segregation takes place at the end of the slope. Then as the cylinder continued to rotate, the segregated particles rolled down to form radial strips. Khakhar et al. (1997) and Gray (2018) reported that particles of different densities or sizes tend to segregate in rotating drums. We attribute this segregation behavior to the void ratio variation with increasing small-size particles fraction. Pillitteri et al. (2020) also showed that the threshold of small-size fractions in the minimum void ratio could increase because of small-size particle separation.

3.5.3. Poly-sized mixtures

We prepared the poly-sized mixtures by combining three or five uniform particle sizes to evaluate the relative size effect on the critical state friction angle. Figure 3.3 documents the fractions used in the three-sized and five-sized mixtures. Different particle sizes and shapes allow investigation of the combined effect of particle shape and relative size. For example, we prepared a three-sized GB mixture. We then prepared three similar mixtures by replacing one uniform size of GB fraction with CG particles in each mixture. We also did the same for the tree-sized CG, five-sized GB, and CG mixtures.

Figures 3.11 and 3.12 present the three-sized and five-sized mixtures' critical state friction angle and void ratio data. The left side of the plot presents the results of glass bead-dominated mixtures; the left side presents the results of crushed glass-dominated mixtures. We made the first mixture on each side with only one particle type; then, we replaced one size fraction with another type of particle. The replaced size fraction becomes smaller from left to right. The critical state friction angle measurements show that replacing GB with CG increases the measured angle, and smaller particles have a greater effect; the GB has more influence than the CG particles. This behavior is likely the result of GB particles being smaller than crashed glass particles, as discussed in Figure 3.7.

The GB void ratio increases upon replacing one size with a CG particle, and the opposite is true when one size of the GB replaces one size of the CG fraction. However, the relative size effect of the replaced particles has yet to be established. That is because void ratio measurements of the altered mixtures are comparable (Figures 3.11 and 3.12). These observations are similar for both three-sized and five-sized mixtures.

3.6. Equivalent Roundness

Our data emphasize the effect of the small size fraction on the measured critical state friction angle. Therefore, we suggest a higher contribution for the small size fraction roundness to the total roundness of a particulate mixture. Particle numbers and surface areas increase with decreasing particle size for the same solid volume. So, we evaluated the equivalent roundness (R_{eq}) of the testing mixtures based on three methods: based on volume fraction ($R_{eq,\,V}$); based on the number of particles ($R_{eq,N}$); and based on surface area ($R_{eq,SA}$). Then, we correlate these equivalent roundnesses estimates with the critical state friction angle to assess their predictability.

3.6.1. Roundness based on the volume fraction

This equivalent roundness is similar to the combined roundness presented by Yang and Wei (2012), and it is determined as:

$$\mathrm{R_{eq,V}} = \frac{\sum_{n=1}^{m} R_n V_n}{\sum_{n=1}^{m} V_n} \tag{6}$$

where m is the total number of mono-sized materials composing the mixture, R_n and V_n are roundness and volume fraction of the n^{th} mono-sized material in the mixture. Table 3.5 documents all testing mixtures' $R_{eq,V}$ values, while Figure 3.13a plots the critical state friction angles versus $R_{eq,V}$. The fitting Equation of the data is:

$$\emptyset'_{cs} = 40 - 15\mathrm{R_{eq,V}} \tag{7}$$

and the coefficient of determination (r^2) is 0.81. Both Equation (7) and r^2 are close to the fitting model proposed by Cho et al., (2006), i.e., ϕ_{cs} = 42-17R with r^2 = 0.84.

3.6.2. Roundness based on particle numbers

We estimated each mono-sized GB and CG particles' average major, intermediate and minor diameter (Table 3.4). First, we measured the diameters of GB and CG with D_{50} = 0.548 mm using image analysis. Next, we used these measurements as a benchmark to estimate the average diameters of other particle sizes. Particle diameters of any mono-sized particle are calculated as:

$$d_i = \frac{D_{50}}{0.548} * d_{i,0.548} \quad (8)$$

where i is 1,2, or 3 for major, intermediate, and minor diameter, D_{50} is for the particle sizes of interest, and $d_{i,0.548}$ is the i^{th} diameter of the particles with D_{50} = 0.548 mm. First, assuming ellipsoid particles, we calculated their volumes using Equation (5). Then, we estimated the number of particles in a constant solid volume, i.e., 100 mm^3, for each mono-sized particle (Table 3.4). Finally, the equivalent roundness based on the number of particles is calculated by:

$$R_{eq,N} = \frac{\sum_{n=1}^{m} R_n V_n N_n}{\sum_{n=1}^{m} V_n N_n} \quad (9)$$

where N_n is the roundness of the n^{th} mono-sized particles in the mixture, Table 3.5 documents the $R_{eq,N}$ of the testing mixtures, and Figure 3.13b presents the correlation between the critical state friction angle and $R_{eq,N}$. The fitting model of the critical state friction angle with $R_{eq,N}$ is:

$$\emptyset'_{cs} = 40 - 14R_{eq,N} \quad (10)$$

with r^2 = 0.93. Equation (10) is close to Equation (7). However, the predictability of Equation (10) is better since it has a significantly higher r^2 value.

3.6.3. Roundness based on the surface area

The surface area (SA) of a single particle of each ellipsoid particle is calculated by:

$$\mathrm{SA} = 4\pi\left[\frac{(0.25\mathrm{d}_1\mathrm{d}_2)^{1.6} + (0.25\mathrm{d}_1\mathrm{d}_3)^{1.6} + (0.25\mathrm{d}_2\mathrm{d}_3)^{1.6}}{3}\right]^{\frac{1}{1.6}} \quad (11)$$

Then, the surface area of 100 mm^3 of particles (SA_{100}) is calculated by:

$$\mathrm{SA}_{100} = \text{number of particles} \cdot \mathrm{SA} \quad (12)$$

The equivalent roundness based on the number of the surface area is calculated by:

$$\mathrm{R}_{\mathrm{eq,SA}} = \frac{\sum_{n=1}^{m} R_n V_n SA_{100,n}}{\sum_{n=1}^{m} V_n SA_{100,n}} \quad (13)$$

where $SA_{100,n}$ is the SA_{100} of the n^{th} mono-sized particles in the mixture. Table 3.5 documents the $R_{eq,SA}$ of the tested mixtures. Figure 3.13c shows the critical state friction angle as a function of $R_{eq,SA}$. The correlation between them is:

$$\emptyset'_{cs} = 41 - 16\mathrm{R}_{\mathrm{eq,SA}} \quad (14)$$

The r^2 of this fitting model is 0.95, the highest compared to Equation (7) and Equation (10). This result indicates the best predictability of the critical state friction angle based on $R_{eq,SA}$.

3.7. Discussion

Our data shows the significant effect of the particle shape on the critical state friction angle in synthetic soils. Rounded particles have a lower critical state friction angle than angular particles (Figure 3.4—Cho et al., 2006). Moreover, while keeping constant particle shape, our data documents the negligible effect of GSD on the critical state friction angle (Figure 3.9—Li et al., 2013; Nguyen et al., 2015; Cantor et al., 2018; Jiang et al., 2018; Yang and Luo, 2018). However, those observations are for materials tested to evaluate the effect of one index property, either

particle shape or GSD. Therefore, to better understand the combined effect of particle shape and relative size on the critical state friction angle, we combined both the particle shape and GSD in testing mixtures.

We document that small-size fractions control the critical state friction angle in bi-sized mixtures (Figure 3.8) and poly-sized mixtures (Figures 3.11 and 3.12). We attribute a more significant contribution of GB over the CG to their size difference. While having the same mean particle size based on sieve analysis, GB particles are overall smaller than CG particles (Figure 3.7 and Table 3.3). Moreover, while larger particles contribute to force chains on soil skeleton and tend to have higher coordination numbers than small particles (Wood and Maeda, 2008, Nguyen et al., 2015; Cantor et al., 2018; 2020), an increasing number of small particles can significantly alter the interactions between larger particles (Thevanayagam, 2007).

Figure 3.8 shows the nonlinear relations between particle type fraction and the measured critical state friction angle. When the small-size fraction volume initially increases in the mixture, it highly affects the critical state friction angle. However, the change in the critical state friction angle declines at a specific volume of small-size particles. Moreover, this volume becomes lower as the small particle relative size becomes smaller (Park and Santamarina (2017) reported similar observations). We suggest that the volume corresponds to the point when small particles cover the surface of the large particles.

Figure 3.14 shows three zones of particle size dominance: large-dominant, transition, and small-dominant. The transition zone is variable depending on the size ratio of small and large particles. Suppose the ratio is large (i.e., small-size particles and large-size particles have approximate sizes). In that case, a more volume fraction of the small-size particles is needed to cover the surface of large particles. Further, a smaller volume of small-size fractions is needed as the small particle

fraction is finer. For example, the transition zone shifts to a smaller small-size fraction with a smaller size fraction.

We calculated the equivalent roundness of the particulate mixtures based on the volume fraction, the number of particles, and the surface areas. The goal was to predict the critical state friction angle. As a result, all equivalent roundnesses are correlated with the critical state friction angle and yield approximate fitting models, Equation (7), (10), and (14). However, the coefficient of determinations are not the same, $R_{eq,V}$ has the lowest r^2, and $R_{eq,SA}$ has the highest r^2. Based on these observations, we proposed the equivalent roundness based on the surface area to be a better parameter that captures the effect of particle shape on the overall response of the mixtures.

3.8. Conclusions

GSD and particle shape are two parameters that dictate coarse-grained soil behavior, and while most classification systems capture the GSD, the particle shape is not captured. Nonetheless, their effects on the critical state friction angle were individually investigated in the past. However, both GSD and particle shape effects must be integrated to capture the complete picture of coarse-grained soils' critical state frictional behavior. Therefore, we conducted a systematic experimental program to evaluate the combined effect of GSD and particle shape on the critical state friction angle. First, we combined uniform rounded GB and angular CG particles of different sizes to create 56 mixtures that vary in particle shape and gradation (including mono-sized, bi-sized, and poly-sized mixtures). Then, we captured the angle of repose (i.e., a proxy for the critical state friction angle) and void ratio in a rotating cylinder using digital photographs and an imaging algorithm (a complete

description of the method is in Alshammari and Fratta, 2023). During testing and analyses, we observe the following behavior, and we draw these conclusions:

- The critical state friction angle correlates well with roundness values for mono-sized mixtures made of a single particle shape.
- Mono-sized mixtures made by mixing different fractions of CG and GB show decreasing critical state friction angle and void ratio with increasing GB volume fractions.
- For bi-sized and poly-sized mixtures made of similar particle shapes, the critical state friction angle is constant, in agreement with previous studies (Li et al., 2013; Nguyen et al., 2015; Cantor et al., 2018; Jiang et al., 2018; Yang and Luo, 2018).
- For bi-sized mixtures made of variable particle shapes, the small-size fraction particle shape has more effect on the critical state friction angle. Furthermore, as a small-size fraction becomes finer, its effect becomes more significant. Despite the higher coordination number and chain forces carried by the large-size fraction, the small-size fraction showed a more significant effect on the critical state friction angle.
- In poly-sized mixtures, the effect of particle shape increases with decreasing particle size.
- We calculated the equivalent roundness of the mixture using three methods: based on volume fraction, particle number, and surface area. All equivalent roundness parameters correlated with the critical state friction angle. However, the equivalent roundness based on surface area yields the highest coefficient of correlation predicting the critical state friction angle.

3.9. Acknowledgments

This research is a product of a scholarship by King Fahd University of Petroleum and Minerals (KFUPM) through the Saudi Arabian Cultural Mission (SACM) and the funds from the Wisconsin Department of Transportation (WisDOT).

3.10. References

Aloufi, M., and Santamarina, J. C. (1995). Low and high strain macrobehavior of grain masses—the effect of particle eccentricity. *Transactions of the ASAE*, *38*(3), 877-887.

Alshammari, A. M., and Fratta, D. (2023). An image processing algorithm for the systematic evaluation of the angle of repose and void ratio of particulate media. To be Submitted for publication.

Altuhafi, F. N., Coop, M. R., and Georgiannou, V. N. (2016). Effect of particle shape on the mechanical behavior of natural sands. *Journal of Geotechnical and Geoenvironmental Engineering*, *142*(12), 04016071.

Altuhafi, F., O'Sullivan, C., and Cavarretta, I. (2013). Analysis of an image-based method to quantify the size and shape of sand particles. *Journal of Geotechnical and Geoenvironmental Engineering*, *139*(8), 1290-1307.

Alyamani, M. S., and Şen, Z. (1993). Determination of hydraulic conductivity from complete grain-size distribution curves. *Groundwater*, *31*(4), 551-555.

Bareither, C. A., Edil, T. B., Benson, C. H., and Mickelson, D. M. (2008). Geological and physical factors affecting the friction angle of compacted sands. *Journal of Geotechnical and Geoenvironmental Engineering*, *134*(10), 1476-1489.

Barrett, P. J. (1980). The shape of rock particles, a critical review. *Sedimentology*, *27*(3), 291-303.

Bolton, M. D. (1986). Strength and dilatancy of sands. *Geotechnique*, *36*(1), 65-78.

Cavarretta, I., Coop, M., and O'Sullivan, C. (2010). The influence of particle characteristics on the behaviour of coarse grained soils. *Géotechnique*, *60*(6), 413-423.

Casagrande, A. (1948). Classification and identification of soils. Transaction of the American Society of Civil Engineers, 113(1), 901-930.

Cantor, D., Azéma, E., Sornay, P., and Radjai, F. (2018). Rheology and structure of polydisperse three-dimensional packings of spheres. *Physical Review E*, *98*(5), 052910.

Cantor, D., Azéma, E., and Preechawuttipong, I. (2020). Microstructural analysis of sheared polydisperse polyhedral grains. *Physical Review E*, *101*(6), 062901.

Chang, C. S., and Deng, Y. (2020). Modeling for critical state line of granular soil with evolution of grain size distribution due to particle breakage. *Geoscience Frontiers*, *11*(2), 473-486.

Chang, C. S., Wang, J. Y., and Ge, L. (2015). Modeling of minimum void ratio for sand–silt mixtures. *Engineering geology*, *196*, 293-304.

Cho, G. C., Dodds, J., and Santamarina, J. C. (2006). Particle shape effects on packing density, stiffness, and strength: natural and crushed sands. *Journal of geotechnical and geoenvironmental engineering*, *132*(5), 591-602.

Cornforth, D. H. (1973). "Prediction of Drained Strength of Sands from Relative Density Measurements," Evaluation of Relative Density and Its Role in Geotechnical Projects Involving Cohesionless Soils, ASTM STP 523, American Society for Testing and Materials, Philadelphia, p. 281–303.

Cox, E. P. (1927). A method of assigning numerical and percentage values to the degree of roundness of sand grains. *Journal of Paleontology*, *1*(3), 179-183.

Cubrinovski, M., and Ishihara, K. (2002). Maximum and minimum void ratio characteristics of sands. *Soils and foundations*, *42*(6), 65-78.

FEMA, (2011). Filteres for Embankment Dams, Best practices for Design and Construction.

Fredlund, M. D., Fredlund, D. G., and Wilson, G. W. (1997). Prediction of the soil-water characteristic curve from grain-size distribution and volume-mass properties. In *Proc., 3rd Brazilian Symp. on Unsaturated Soils* (Vol. 1, pp. 13-23). Rio de Janeiro.

Fuggle, A. R., Roozbahani, M. M., and Frost, J. D. (2014). Size effects on the void ratio of loosely packed binary particle mixtures. In *Geo-Congress 2014: Geo-Characterization and Modeling for Sustainability* (pp. 129-138).

Gray, J. M. N. T. (2018). Particle segregation in dense granular flows. *Annual review of fluid mechanics*, *50*, 407-433.

Holtz, R. D., Kovacs, W. D., and Sheahan, T. C. (2011). An introduction to geotechnical engineering. (2nd ed.). Pearson.

Igwe, O., Sassa, K., and Wang, F. (2007). The influence of grading on the shear strength of loose sands in stress-controlled ring shear tests. *Landslides*, *4*(1), 43.

Jiang, M. D., Yang, Z. X., Barreto, D., and Xie, Y. H. (2018). The influence of particle-size distribution on critical state behavior of spherical and non-spherical particle assemblies. *Granular Matter*, *20*(4), 80.

Khakhar, D. V., McCarthy, J. J., and Ottino, J. M. (1997). Radial segregation of granular mixtures in rotating cylinders. *Physics of Fluids*, *9*(12), 3600-3614.

Kleinhans, M. G., Markies, H., De Vet, S. J., and Postema, F. N. (2011). Static and dynamic angles of repose in loose granular materials under reduced gravity. *Journal of Geophysical Research: Planets*, *116*(E11).

Kovačević, M., Jurić-Kaćunić, D., Librić, L., and Ivoš, G. (2018). Engineering soil classification according to EN ISO 14688-2:2018. Gradevinar, 70(10), 873-879.

Kumara, G. J. J., Hayano, K., and Ogiwara, K. (2012). Image analysis techniques on evaluation of particle size distribution of gravel. *GEOMATE Journal*, *3*(5), 290-297.

Ladd, C. C., Foott, R., Ishihara, K., Schlosser, F., and Poulos, H. G. (1977). Stress-deformation and strength characteristics. ICSMFE 9, Tokyo, July 1977. In Proceedings (Vol. 2, pp. 421-494).

Lade, P. V., Liggio, C. D., and Yamamuro, J. A. (1998). Effects of non-plastic fines on minimum and maximum void ratios of sand. *Geotechnical testing journal*, *21*, 336-347.

Lee, J. S., Guimaraes, M. S., and Santamarina, J. C. (2007). Micaceous sands: Microscale mechanisms and macroscale response. *Journal of Geotechnical and Geoenvironmental Engineering*, *133*(9), 1136-1143.

Li, G., Ovalle, C., Dano, C., and Hicher, P. Y. (2013). Influence of grain size distribution on critical state of granular materials. In *Constitutive modeling of geomaterials* (pp. 207-210). Springer, Berlin, Heidelberg.

Mitchell, J. K., and Soga, K. (2005). Fundamentals of soil behavior. *Fundamentals of soil behavior.*, (Ed. 3).

Muir Wood, D., and Maeda, K. (2008). Changing grading of soil: effect on critical states. *Acta Geotechnica*, *3*(1), 3-14.

Nguyen, D. H., Azéma, E., Sornay, P., and Radjai, F. (2015). Effects of shape and size polydispersity on strength properties of granular materials. *Physical Review E*, *91*(3), 032203.

Odong, J. (2007). Evaluation of empirical formulae for determination of hydraulic conductivity based on grain-size analysis. *Journal of American Science*, *3*(3), 54-60.

Ohm, H. S., and Hryciw, R. D. (2013). Translucent segregation table test for sand and gravel particle size distribution. *Geotechnical Testing Journal*, *36*(4), 592-605.

Park, J., and Santamarina, J. C. (2017). Revised soil classification system for coarse-fine mixtures. *Journal of Geotechnical and Geoenvironmental Engineering*, *143*(8), 04017039.

Pillitteri, S., Opsomer, E., Lumay, G., and Vandewalle, N. (2020). How size ratio and segregation affect the packing of binary granular mixtures. *Soft Matter*, *16*(39), 9094-9100.

Rothenburg, L., and Bathurst, R. J. (1989). Analytical study of induced anisotropy in idealized granular materials. *Geotechnique*, *39*(4), 601-614.

Rousé, P. C. (2014). Comparison of methods for the measurement of the angle of repose of granular materials. *Geotechnical Testing Journal*, *37*(1), 164-168.

Santamarina, J. C., and Cho, G. C. (2001). Determination of critical state parameters in sandy soils—simple procedure. *Geotechnical testing journal*, *24*(2), 185-192.

Santamarina, J. C., and Cho, G. C. (2004). Soil behaviour: The role of particle shape. Skempton Conf.: Advances in Geotechnical Engineering, R. J. Jardine, D. M. Potts, and K. G. Higgins, eds., Vol. 1, Thomas Telford, London, 604–617.

Santamarina, J. C., Klein, K. A., and Fam, M. A. (2001). *Soils and waves*. New York: J. Wiley & Sons.

Santamarina, J. C., and Shin, H. (2009). Friction in granular media. *Meso-scale Shear Physics in Earthquake and Landslide Mechanics. CRC Press, London*, 157-188.

Savage, S. B., and Lun, C. K. K. (1988). Particle size segregation in inclined chute flow of dry cohesionless granular solids. *Journal of Fluid Mechanics*, *189*, 311-335.

Schofield, A. N., and Wroth, P. (1968). *Critical state soil mechanics* (Vol. 310). London: McGraw-hill.

Simoni, A., and Houlsby, G. T. (2006). The direct shear strength and dilatancy of sand–gravel mixtures. *Geotechnical & Geological Engineering*, *24*(3), 523.

Suh, H. S., Kim, K. Y., Lee, J., and Yun, T. S. (2017). Quantification of bulk form and angularity of particle with correlation of shear strength and packing density in sands. *Engineering Geology*, *220*, 256-265.

Tapia, F., Pouliquen, O., and Guazzelli, É. (2019). Influence of surface roughness on the rheology of immersed and dry frictional spheres. *Physical Review Fluids*, *4*(10), 104302.

Terzaghi, K., Peck, R. B., and Mesri, G. (1996). Soil mechanics in engineering practice. John Wiley & Sons.

Thevanayagam, S. (2007). Intergrain contact density indices for granular mixes—I: Framework. *Earthquake Engineering and Engineering Vibration*, *6*(2), 123-134.

Tickell, F. G. (1931). The examination of fragmental rocks. Stanford, California, USA: Stanford University Press.

Wadell, H. (1933). Sphericity and roundness of rock particles. *The Journal of Geology*, *41*(3), 310-331.

Wei, L. M., and Yang, J. (2014). On the role of grain shape in static liquefaction of sand–fines mixtures. *Géotechnique*, *64*(9), 740-745.

Wichtmann, T., Navarette Hernandez, M., Martinez, R., Duran Grae, F., and Triantafyllidis, T. (2011). Estimation of the small-strain stiffness of granular soils taking into account the grain size distribution curve. In *Fifth International Conference on Earthquake Geotechnical Engineering, Santiago, Chile*.

Wood, D. M. (1990). *Soil behaviour and critical state soil mechanics*. New York: Cambridge University Press, pp 219-224.

Wroth, C. P., and Wood, D. M. (1978). The correlation of index properties with some basic engineering properties of soils. *Canadian Geotechnical Journal*, *15*(2), 137-145.

Xiao, Y., Long, L., Matthew Evans, T., Zhou, H., Liu, H., and Stuedlein, A. W. (2019). Effect of particle shape on stress-dilatancy responses of medium-dense sands. *Journal of Geotechnical and Geoenvironmental Engineering*, *145*(2), 04018105.

Yang, J., and Luo, X. D. (2015). Exploring the relationship between critical state and particle shape for granular materials. *Journal of the Mechanics and Physics of Solids*, *84*, 196-213.

Yang, J., and Luo, X. D. (2018). The critical state friction angle of granular materials: does it depend on grading?. *Acta Geotechnica*, *13*(3), 535-547.

Yang, J., and Wei, L. M. (2012). Collapse of loose sand with the addition of fines: the role of particle shape. *Géotechnique*, *62*(12), 1111-1125.

Youd, T. L. (1973). Factors controlling maximum and minimum densities of sands. Evaluation of Relative Density and its Role in Geotechnical Projects Involving Cohesionless Soils. In STP523-EB *Evaluation of relative density and its role in geotechnical projects involving cohesionless soils*, Edited by R.S. Ladd, ASTM STP 523, American Society for Testing and Materials, Philadelphia, ASTM, 98-112.

Zheng, J., and Hryciw, R. D. (2015). Traditional soil particle sphericity, roundness and surface roughness by computational geometry. *Géotechnique*, *65*(6), 494-506.

Table 3.1: Five definitions of sphericity (Zheng and Hryciw, 2015).

Sphericity definition	Mathematical definition	Reference
Perimeter sphericity	$S_P = \frac{P_e}{P} = \frac{Perimeter\ of\ circle\ has\ similar\ area\ of\ particle}{Perimeter\ of\ particle\ 2D\ projection}$	Cox (1927); Altuhafi et al. (2013)
Area sphericity	$S_A = \frac{A}{A_c} = \frac{Area\ of\ particle\ 2D\ projection}{Area\ of\ minimum\ cirumscribed\ circle}$	Tickell (1931)
Diameter sphericity	$S_D = \frac{D_e}{D_{cir}} = \frac{Diameter\ of\ circle\ has\ similar\ area\ of\ particle}{Diameter\ of\ minmum\ cicumscribed\ circle}$	Wadell (1933)
Circle ratio sphericity	$S_c = \frac{D_{ins}}{D_{cir}} = \frac{Maximum\ inscribed\ circle}{minimum\ cirumscribed\ circle}$	Riley (1941); Santamarina and Cho (2004)
Aspect ratio	$S_{WL} = \frac{W}{L} = \frac{Particle's\ width}{Particle's\ length}$	Krumbein and Sloss (1963)

Table 3.2: Size and particle shape properties of uniform GB and CG.

Particle Size		Glass Beads					Crushed Glass				
Sieve No. (passed-retained)	D_{50} (mm)	G_s	Roundness		Aspect Ratio		G_s	Roundness		Aspect Ratio	
			Average	Std. dev	Average	Std. dev		Average	Std. dev	Average	Std. dev
18-20	0.922	2.49	0.99	0.01	0.97	0.02	2.5	0.26	0.06	0.69	0.12
25-30	0.653	2.49	0.96	0.07	0.97	0.04	2.52	0.24	0.06	0.69	0.13
30-35	0.548	2.49	0.95	0.12	0.96	0.09	2.51	0.26	0.11	0.65	0.16
45-50	0.326	2.48	0.95	0.09	0.96	0.09	2.51	0.30	0.07	0.69	0.15
60-70	0.23	2.46	0.97	0.06	0.99	0.03	2.51	0.29	0.09	0.64	0.15

Table 3.3: Volume calculations statistics of thirty-five GB and CG particles retained between sieves No. 30 and No. 35.

Material		Glass beads	Crushed glass
Volume (mm^3)	Average	0.09	0.17
	Max	0.11	0.26
	Min	0.06	0.09
	Std. dev	0.01	0.05

Table 3.4: Particle volume and surface area of the testing particles.

Material	D_{50}[a]	Particle diameter (mm)			Per one particle		Per 100 mm^3	
		Major, d_1	Intermediate, d_2	Minor, d_3	PV (mm^3)[c]	SA (mm^2)[d]	Number of particles	SA_{100} (mm^2)[e]
Glass Beads	0.922	0.929	0.910	0.910	0.403	2.640	248	655
	0.653	0.658	0.645	0.645	0.143	1.324	698	924
	0.548[b]	0.552	0.541	0.541	0.085	0.933	1181	1101
	0.326	0.329	0.322	0.322	0.018	0.330	5610	1851
	0.230	0.232	0.227	0.227	0.006	0.164	15975	2624
Crushed Glass	0.922	1.830	1.101	0.772	0.815	4.630	123	568
	0.653	1.296	0.780	0.547	0.289	2.322	345	802
	0.548[b]	1.088	0.654	0.459	0.171	1.636	584	956
	0.326	0.647	0.389	0.273	0.036	0.579	2776	1607
	0.230	0.457	0.275	0.193	0.013	0.288	7905	2278

[a] The mean particle size is based on sieve analysis.

[b] The dimensions are obtained by image analysis of the thirty-five pairs of GB and CG particles.

Note: other particle size diameters are estimated by $\mathbf{d_i = \frac{D_{50}}{0.548} * d_{i,0.548}}$, where i can be 1,2, or 3, D_{50} is for the particle size of interest, and $d_{i,\,o.548}$ is the i^{th} diameter of the same type particles with D_{50} = 0.548 mm.

[c] Particle volume, $\mathbf{VP = \frac{\pi}{6} d_1 d_2 d_3}$.

[d] Surface Area, $\mathbf{SA = 4\pi \left[\frac{(0.25 d_1 d_2)^{1.6} + (0.25 d_1 d_3)^{1.6} + (0.25 d_2 d_3)^{1.6}}{3}\right]^{\frac{1}{1.6}}}$.

[e] Surface area of 100 mm^3 solid volume, $\mathbf{SA_{100} = Number\ of\ particles\ per\ 100\ mm^3 \cdot SA}$.

Table 3.5: Equivalent roundnesses calculated based on volume fraction, number of particles, and surface area of the testing mixtures.

Mixture	R_V	$R_{eq,N}$	$R_{eq,SA}$	Mixture	R_V	$R_{eq,N}$	$R_{eq,SA}$
1	0.99	0.99	0.99	29	0.71	0.33	0.50
2	0.96	0.96	0.96	30	0.85	0.37	0.67
3	0.95	0.95	0.95	31	0.29	0.30	0.29
4	0.95	0.95	0.95	32	0.28	0.30	0.29
5	0.97	0.97	0.97	33	0.26	0.29	0.27
6	0.26	0.26	0.26	34	0.25	0.28	0.26
7	0.24	0.24	0.24	35	0.38	0.81	0.50
8	0.26	0.26	0.26	36	0.52	0.89	0.67
9	0.30	0.30	0.30	37	0.67	0.93	0.79
10	0.29	0.29	0.29	38	0.81	0.94	0.88
11	0.40	0.49	0.42	39	0.96	0.95	0.96
12	0.54	0.66	0.56	40	0.28	0.29	0.28
13	0.68	0.78	0.70	41	0.75	0.52	0.65
14	0.81	0.87	0.83	42	0.74	0.89	0.77
15	0.96	0.95	0.96	43	0.72	0.94	0.84
16	0.97	0.96	0.96	44	0.49	0.88	0.64
17	0.97	0.96	0.97	45	0.50	0.49	0.51
18	0.98	0.97	0.98	46	0.52	0.34	0.43
19	0.98	0.97	0.97	47	0.96	0.97	0.96
20	0.98	0.97	0.97	48	0.27	0.29	0.28
21	0.98	0.97	0.98	49	0.82	0.96	0.88
22	0.99	0.97	0.98	50	0.83	0.95	0.87
23	0.41	0.33	0.37	51	0.83	0.88	0.81
24	0.55	0.42	0.49	52	0.83	0.62	0.74
25	0.70	0.55	0.63	53	0.42	0.33	0.39
26	0.84	0.72	0.79	54	0.41	0.36	0.40
27	0.43	0.30	0.34	55	0.40	0.55	0.47
28	0.57	0.31	0.41	56	0.41	0.84	0.55

Note: R_V: equivalent roundness based on the volume fraction.
$R_{eq,N}$: equivalent roundness based on the number of particles.
$R_{eq,SA}$: equivalent roundness based on the surface area.

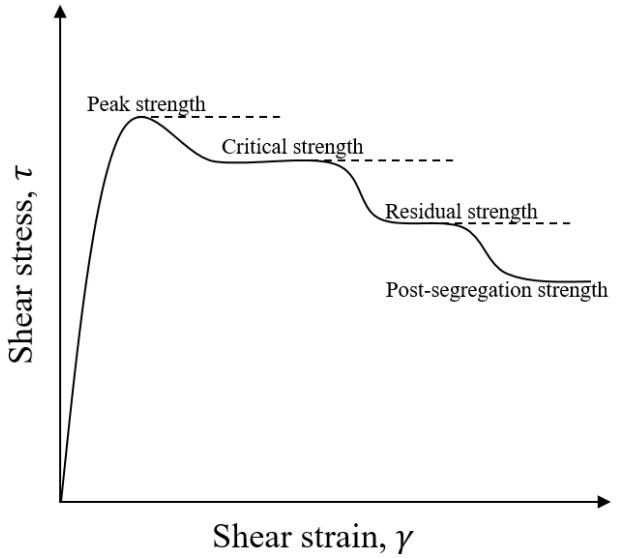

Figure 3.1: Hypothetical shear response of particulate material. Dashed and solid lines refer to two expected responses.

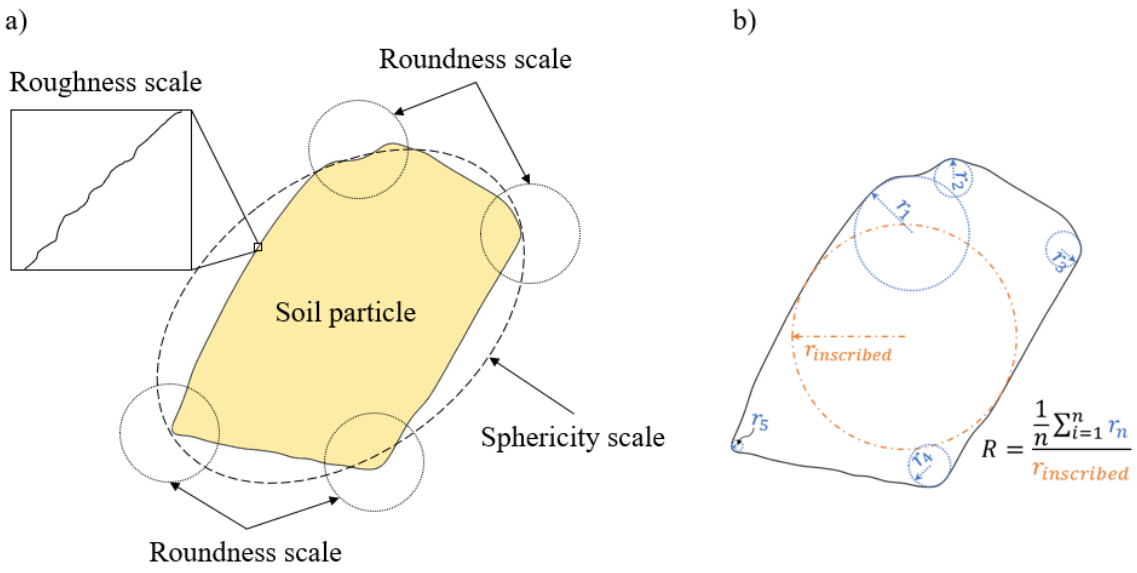

Figure 3.2: a) Particle shape scales: sphericity, roundness, and roughness; b) definition of roundness: the average of radii of circles fitted in the particle major features divided by the radius of the maximum inscribed circle.

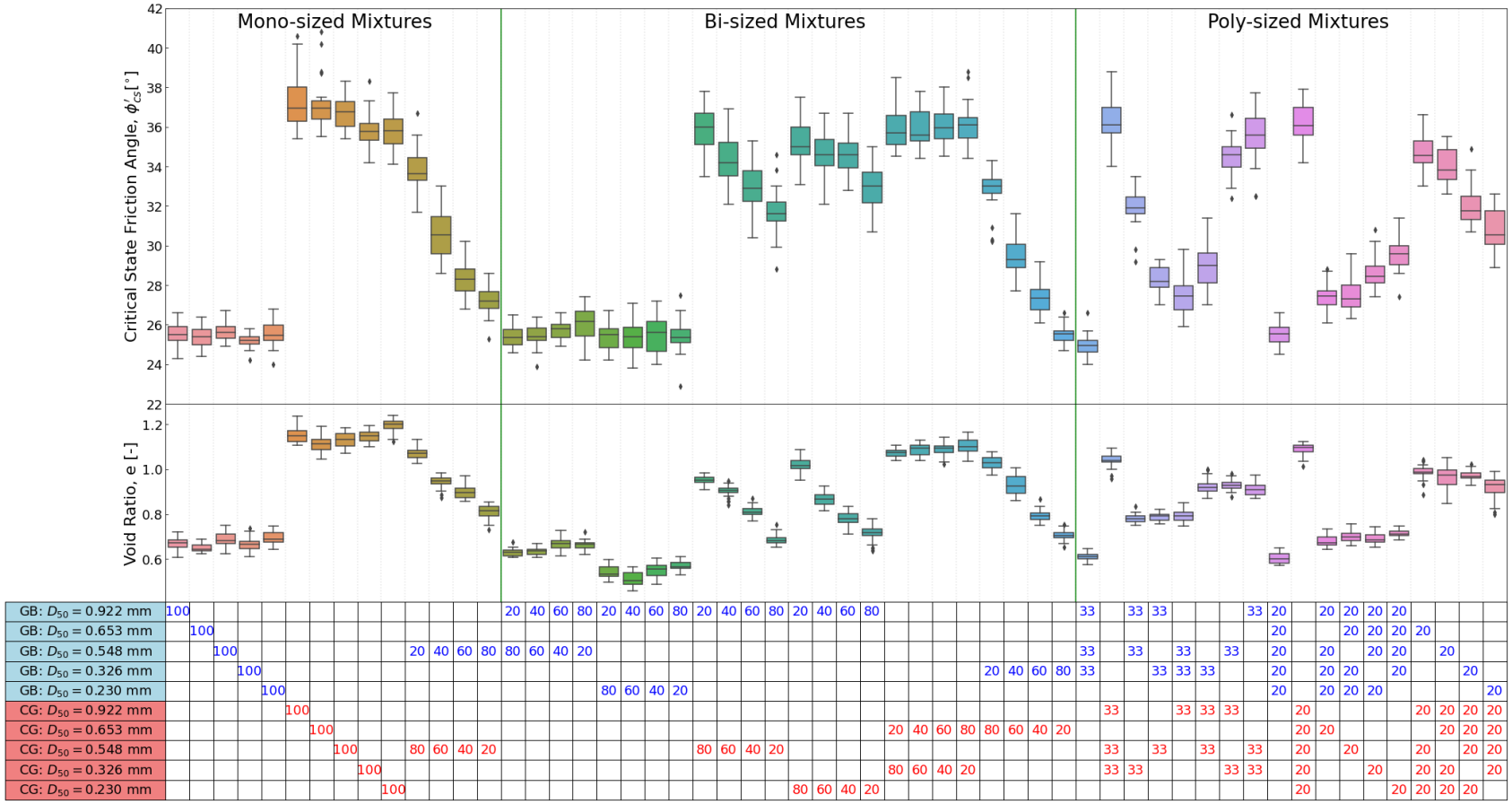

Figure 3.3: Experimental data matrix. The upper section of the y-axis documents the critical state friction angle measurements. The lower section of the y-axis presents the void ratio calculations. The x-axis is a table showing the volumetric percentage of constituents for each of the tested mixtures. The numbers in the table are volumetric percentages (%) of different fractions in the mixture. Blue cells are for the GB, and the red cells are for the CG. The left, middle and right regions present mono-sized, bi-sized, and poly-sized mixtures.

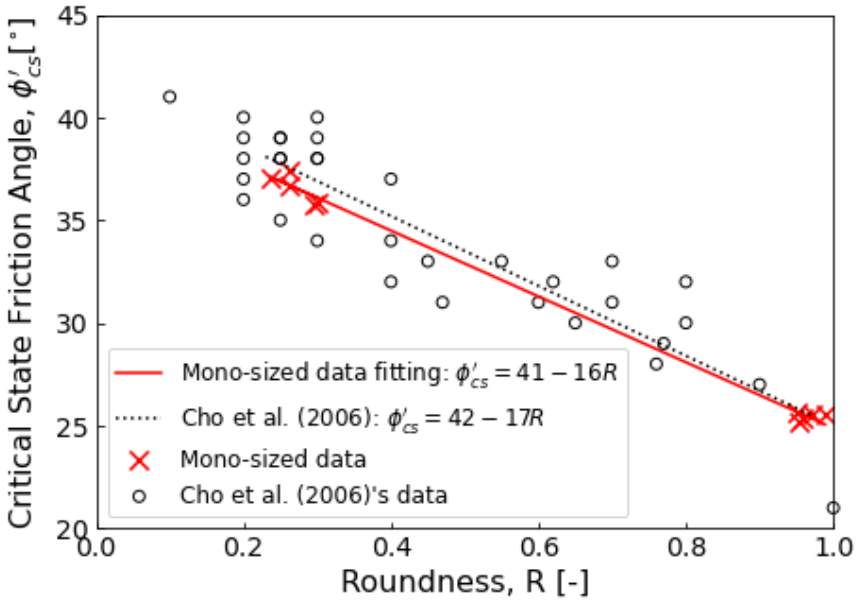

Figure 3.4: The critical state friction angle as a function of roundness for the mono-sized mixture made of one type of particle, either GB or CG. The open circles correspond to Cho et al. (2006)'s measurements.

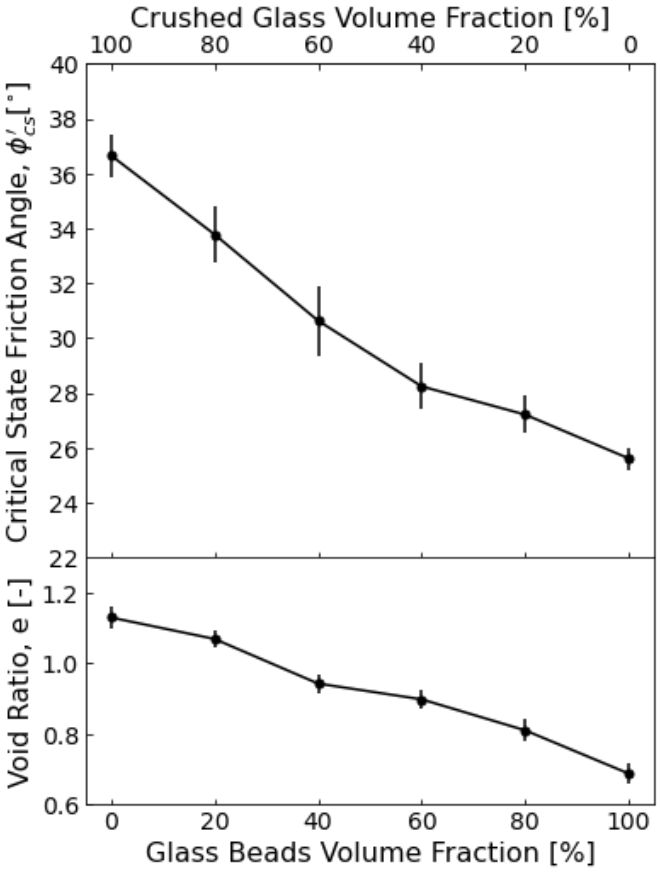

Figure 3.5: Variation of the critical state friction and void ratio of uniform size mixtures made of CG and GB of D_{50} = 0.548 mm.

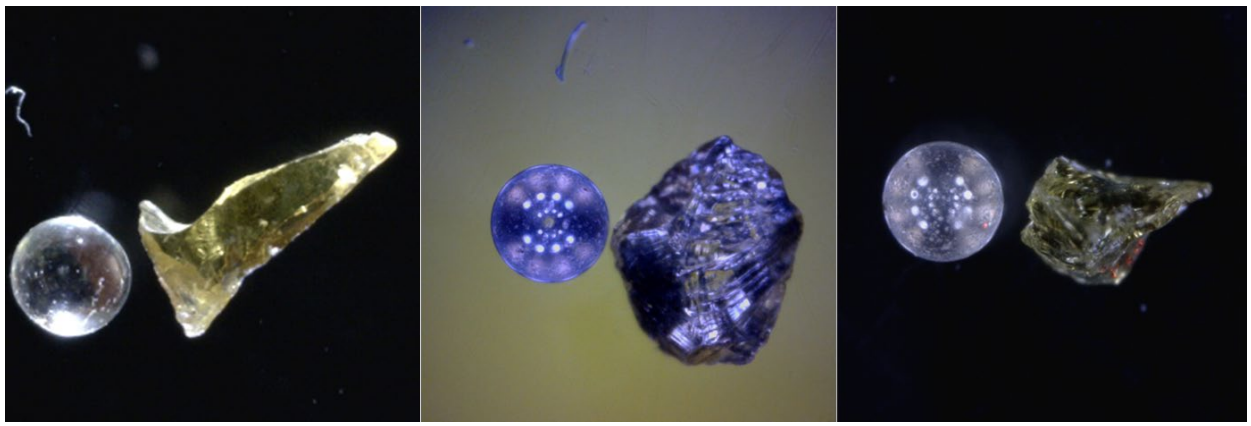

Figure 3.6: Pairs of the glass bead and CG retained between sieves No. 30 and No. 35 (i.e., D_{50} = 0.548 mm).

Figure 3.7: Silhouettes of CG and GB pairs rested naturally on the left side and rolled on the other side on the right side.

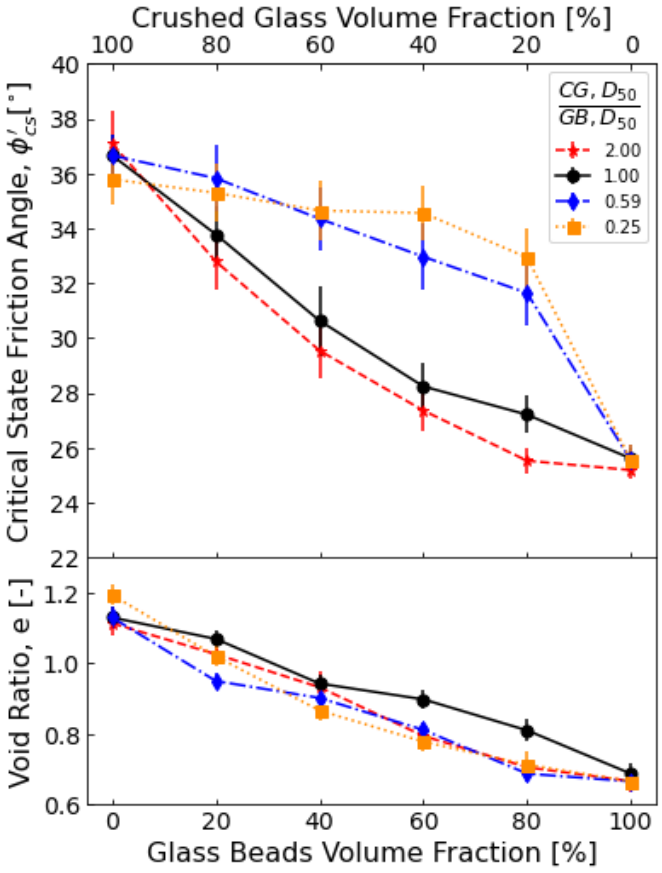

Figure 3.8: Critical state friction angle and void ratio variation of GB and CG binary mixtures.

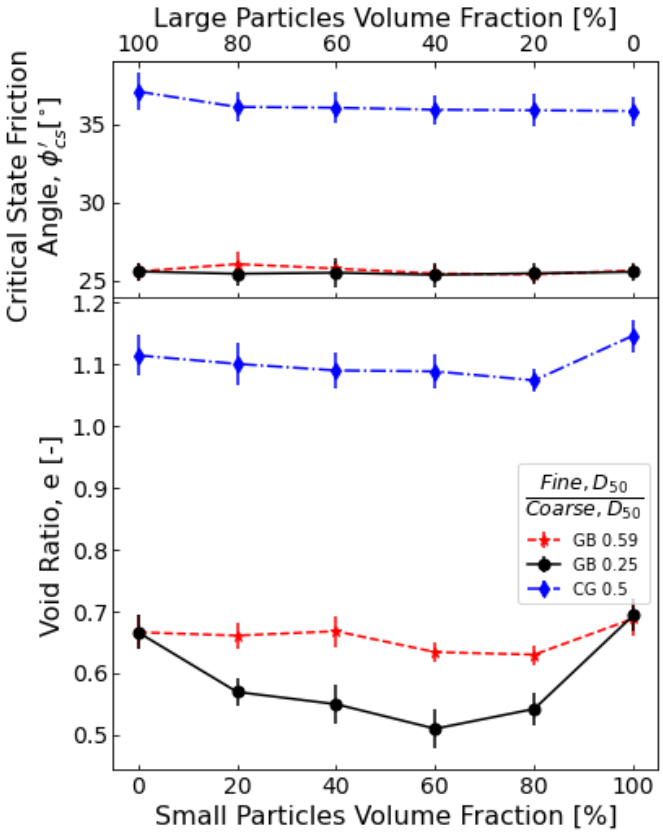

Figure 3.9: Critical state friction angle and void ratio variation of GB or CG binary mixtures.

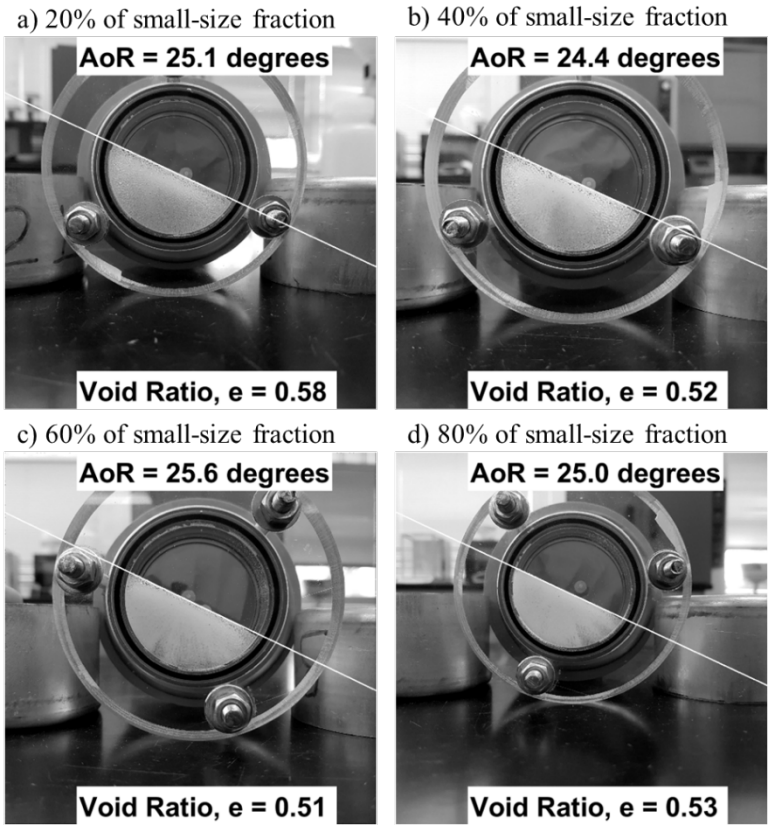

Figure 3.10: Pictures of the testing cylinder during the angle of repose measurements of bi-sized GB mixtures where large particles have D_{50} = 0.922 mm and small particles have D_{50} = 0.230 mm. The volume fraction of small-size particles is a) 20%, b) 40%, c) 60%, and d) 80%.

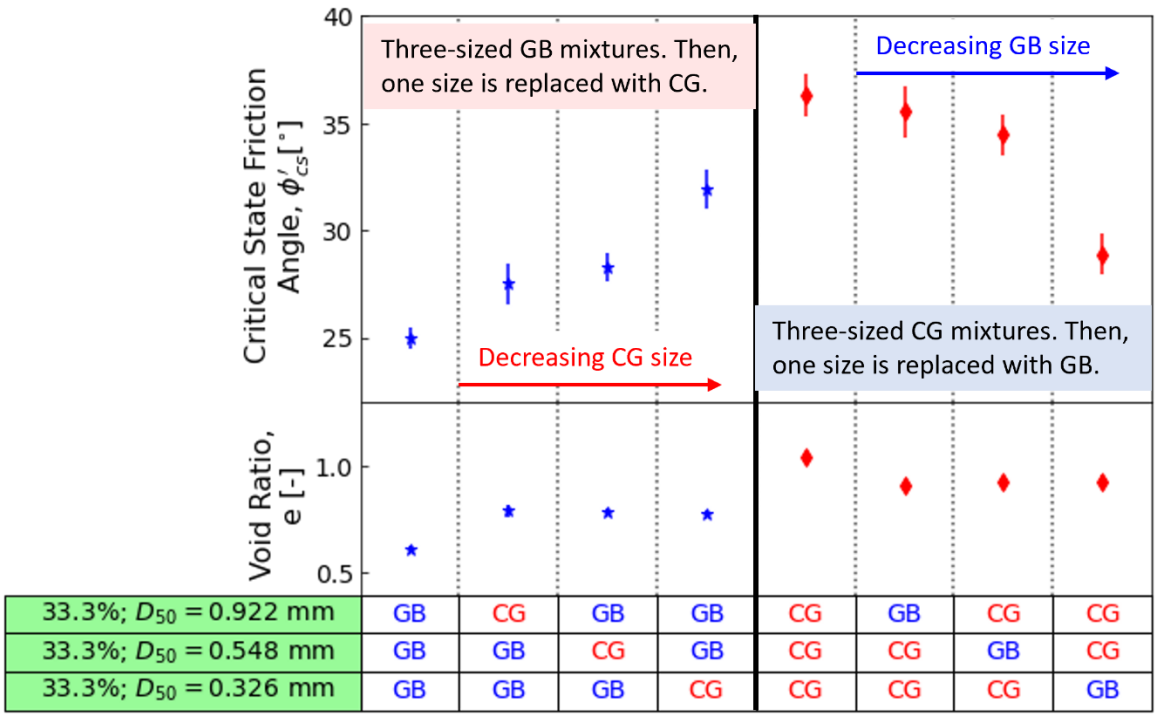

Figure 3.11: Three-sized mixtures made of one type of particle. Then, a different particle type replaces one size. The left side is GB dominated, and the right is CG dominated. The columns of the bottom table show the constituents of each mixture; the rows show volumetric fractions of the mean particle size of each constituent.

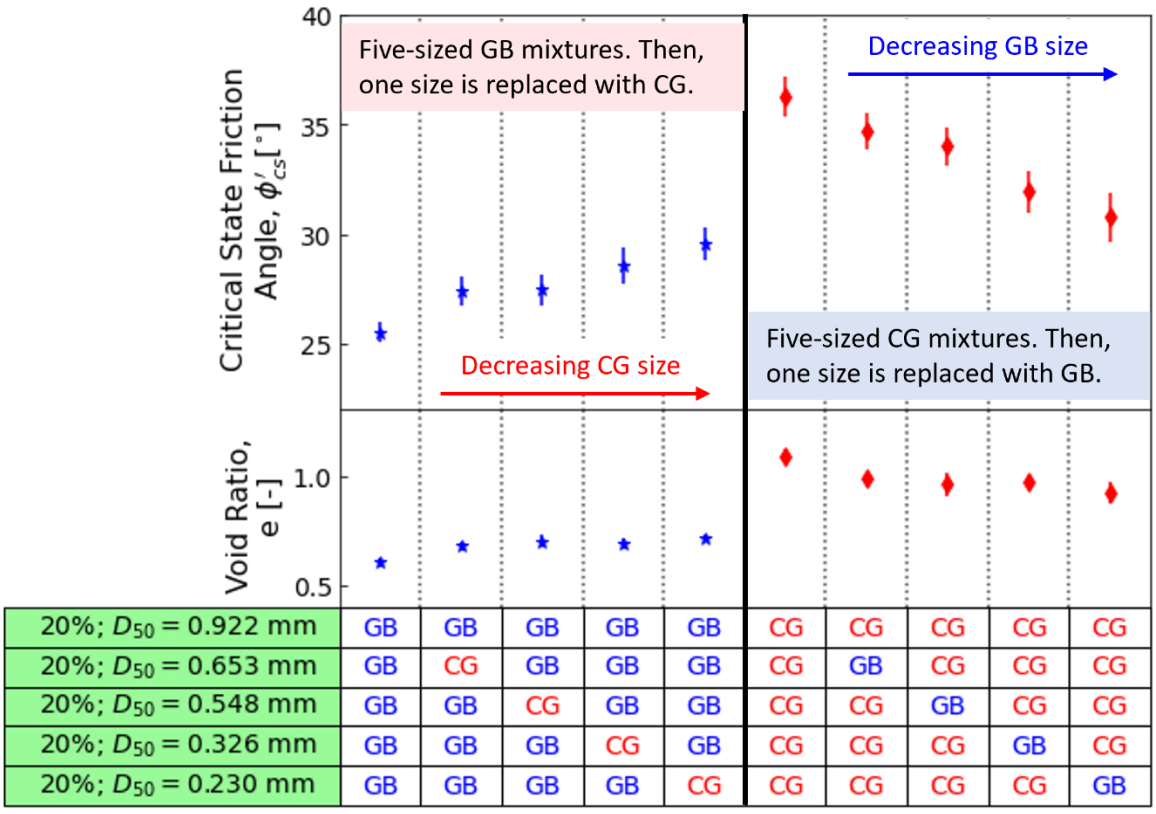

20%; D_{50} = 0.922 mm	GB	GB	GB	GB	GB	CG	CG	CG	CG	CG
20%; D_{50} = 0.653 mm	GB	CG	GB	GB	GB	CG	GB	CG	CG	CG
20%; D_{50} = 0.548 mm	GB	GB	CG	GB	GB	CG	CG	GB	CG	CG
20%; D_{50} = 0.326 mm	GB	GB	GB	CG	GB	CG	CG	CG	GB	CG
20%; D_{50} = 0.230 mm	GB	GB	GB	GB	CG	CG	CG	CG	CG	GB

Figure 3.12: Five-sized mixtures made of one type of particle. Then, a different particle type replaces one size. The left side is GB-particle dominated, and the right is CG-particle dominated. The columns of the bottom table show the constituents of each mixture; the rows show volumetric fractions of the mean particle size of each constituent.

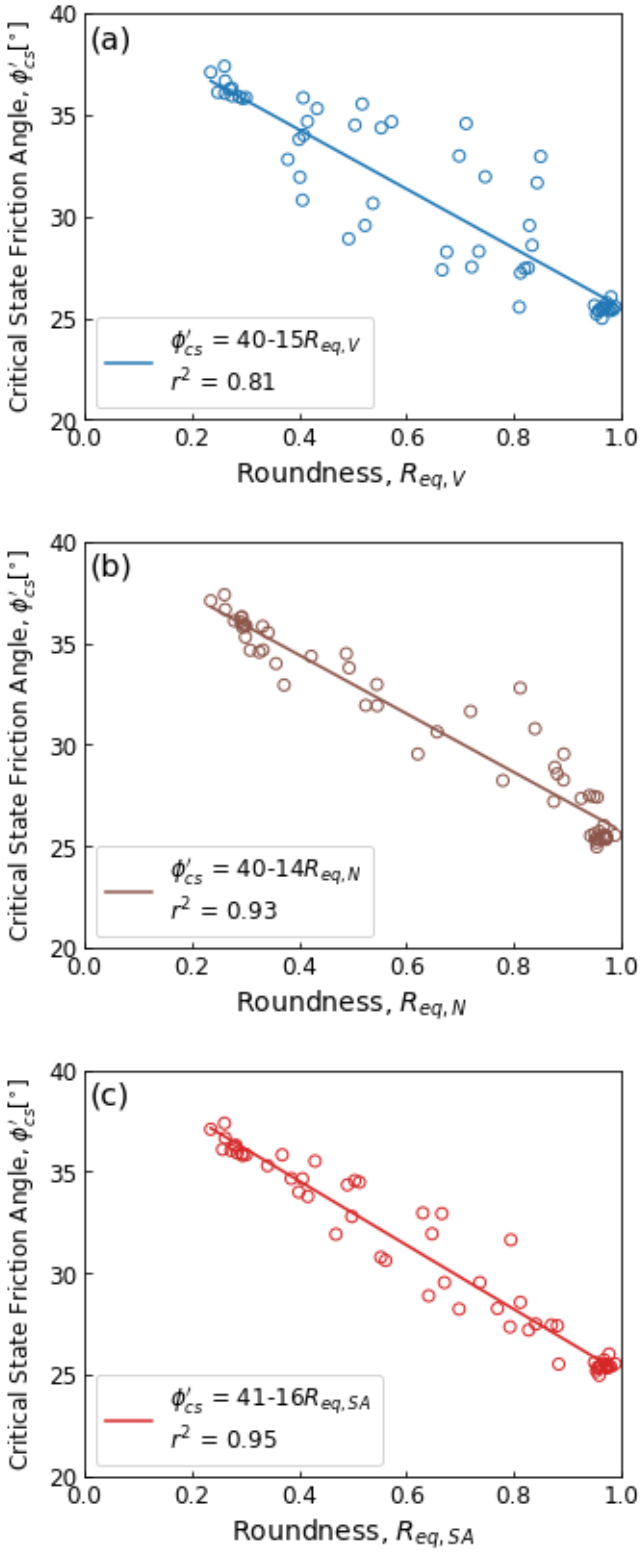

Figure 3.13: The critical state friction angle versus equivalent roundness: (a) equivalent roundness based on volume fraction, (b) equivalent roundness based on the number of particles, and (c) equivalent roundness based on the surface area.

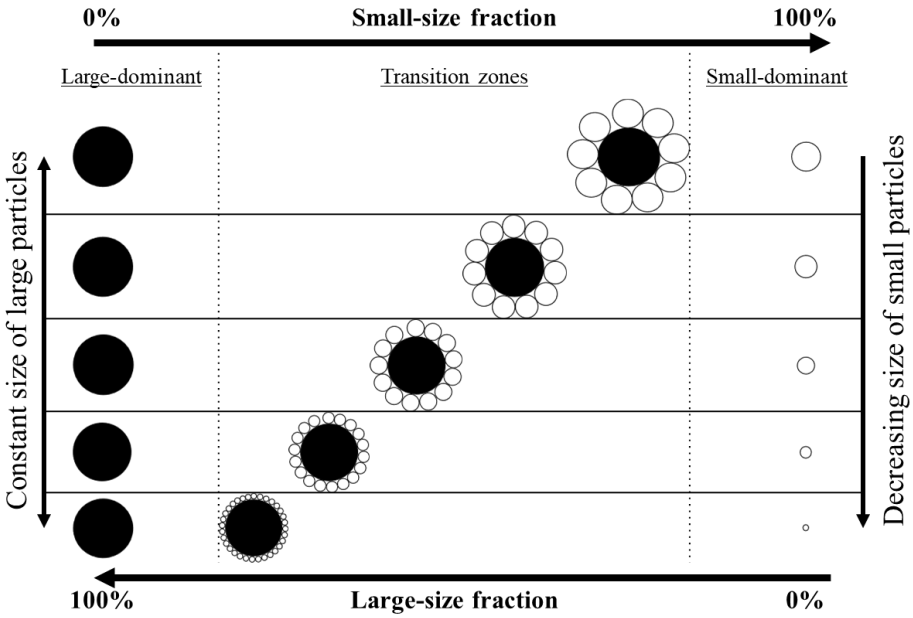

Figure 3.14: Conceptual model of the frictional behavior from large-dominant to small-dominant particles. The solid and open circles are for large and small particles, respectively.

CHAPTER 4:

The Combined Effect of Particle Shape and Grain Size Distribution on the Critical State Response of Coarse-Grained Soils

Ammar Mohammed Alshammari[5,6], Dante Fratta[6]

Abstract

We present an experimental program and simple model developments to test and evaluate how particle shape and grain size distribution (GSD) control the critical state response of coarse-grained soils. We tested over 50 controlled mixtures of different particulate materials to estimate the critical state void response based on the particle shape or grain size distribution. The evaluation of the tests shows that the position and slope of the critical state line change as the soil particles become more well-graded or include fractions with rounded shapes. However, the effect of particle shape varies across different particle sizes. Therefore, we adopted a simple method to assess the critical state line position of fifty-six mixtures with different particle sizes and shapes. We observed that large particle fractions tend to create skeletons with voids that the small particle fractions fill. During this process, the small particle fraction first reduces the critical state void ratio at specific effective stress (e_{cr}) as small particles fill the void between large particles, and then the small particle fraction might increase the e_{cr} as the small particles separate the large particles. Furthermore, the particle shape of the small size fractions dictates the solid volume needed to fill the voids and reach lower e_{cr}. As the solid volume of the small size fraction increases, e_{cr} decreases because the finer particles fill the space between the large particle fraction skeleton.

[5] Department of Civil and Environmental Engineering, King Fahd University of Petroleum & Minerals, Dhahran 31261, Saudi Arabia. Email: ashammari@kfupm.edu.sa
[6] Geological Engineering, Department of Civil and Environmental Engineering, University of Wisconsin–Madison, Madison, WI 53706, USA. Email: fratta@wisc.edu

However, as the small size fraction continues to increase, the large particles lose contact with other large particles, and the e_{cr} once again increases. Also, the particle shape of the small size fraction controls the large-strain stiffness. This effect is most significant as the particles in the small particle fraction become finer. The slope of the critical state line on e-log(p') correlates well with equivalent roundness based on the surface area of particles ($R_{eq,SA}$). However, the critical state line intercept correlates with the $R_{eq,SA,}$ and the coefficient of uniformity (C_u).

Keywords: binary mixtures, poly-sized mixture, glass beads, crushed glass.

4.1. Introduction

Critical State Soil Mechanics is a conceptual model used by engineers and scientists to describe the mechanical response of particulate materials at failure (Schofield and Worth, 1968; Wood, 1990). The critical state (CS) of a soil is defined by Schofield and Worth (1968) as the continuing shear distortion (γ) when the soil behaves like a frictional fluid. Wood (1990) explained the critical state as the nonstop plastic shearing of soil without any change in volume or effective stress (i.e., $\frac{dp\prime}{d\gamma} = \frac{dq}{d\gamma} = \frac{de}{d\gamma} = 0$, where $p' = \frac{\sigma_1' + 2\sigma_3'}{3}$ is the effective mean stress, $q = \sigma'_1 - \sigma'_3$ is the deviatoric stress, σ'_1 and σ'_3 are the maximum and minimum principal stresses, and e is the void ratio). The critical state represents a line in the 3-D effective stress-shear stress-void ratio (p'-q-e) space and is called the critical state line (CSL—Figure 4.1). Thus, the CSL is defined by:

$$q_{cs} = Mp'_{cs} \qquad \textit{CSL projection on the q-p' plane} \tag{15}$$

$$e_{cs} = e_{1kPa} - \lambda \log\left(\frac{p'_{cs}}{p_r}\right) \qquad \textit{CSL projection on the e-log(p') plane} \tag{16}$$

where the subscript cs stands for the critical state, M is the slope of the critical state line on the q-p' plane, e_{1kPa} is the critical state void ratio at the reference stress, λ is the slope of CSL on the e-log(p') plane, and p_r = 1 kPa is the reference stress. On the e-p' plane, the CSL projection is a straight line plotted on a semi-log scale (i.e., e-log(p') plane[7]). In Equation (15), M is related to the friction angle ϕ_{cs} at the critical state, but it is different for extension and compression load paths:

$$M = \frac{6\ \sin(\emptyset_{cs})}{3 - \sin(\emptyset_{cs})} \qquad \textit{for axial compression} \tag{17}$$

$$M = -\frac{6\ \sin(\emptyset_{cs})}{3 + \sin(\emptyset_{cs})} \qquad \textit{for axial extension} \tag{18}$$

[7] Equation (2) can also be written with natural logarithm and with specific volume v = 1+e (Roscoe et al., 1958; Schofield and Worth, 1968), but λ will have a different numerical value.

While the Critical State Soil Mechanics theory is a robust model, substantial advancements have occurred since it was proposed (Roscoe et al. 1958, Schofield and Worth 1968). For example, Dafalias (1986) incorporated the evolution of anisotropy into the critical state, Been and Jefferies (1985) captured the effect of fines on the critical state and defined the concept of state parameter (describing dilative/contractive response of soils upon shearing), and Wood and Maeda (2008) reported the influence of grain size distribution (GSD) on the critical state parameters.

Furthermore, several researchers attempted to correlate critical parameters with intrinsic soil properties, yet this area has not been fully explored. For fine-grained soils, Atterberg limits correlate well with the critical state parameters (Wood, 1990). For coarse-grained soils, Cho et al. (2006), Wood and Maeda (2008), Yang and Luo (2015), Chang and Deng (2020), Lashkari et al. (2020), and Wu et al. (2021) reported the link of critical state parameters to either particle shape descriptors or GSD. However, the combined effect of particle shape and GSD on the critical state is still unexplored.

We have already investigated the combined effect of particle shape and relative size on the critical state friction angle (Alshammari and Fratta, 2023a). In that study, we found that in multi-sized particulate mixtures, the particle shape of small-size fractions tends to influence the critical state friction angle more than the shape of large-size fractions. We attributed that observation to the ability of small-size particles to fill the pore space and cover the surface of the large particles, therefore, controlling interactions in the network of particles. In the current research, we expand our studies to investigate the combined effect of particle shape and grain size distribution (GSD) on the CS parameters on the e-log(p') plane, $e_{1kPa,}$ and λ. We tested glass beads (GB) and crushed glass (CG) mixtures. Our results show that particle shape and GSD are both controlling factors of e_{1kPa} and λ. However, the particle shape of the small-size fractions has more influence on the slope

and position of the CSL on the e-log(p') plane than the particle shape of the large-size fraction. Furthermore, these results and the simple correlations show that descriptor parameters describing the particle shape and GSD of soils can capture the critical state response of coarse-grained soils.

4.2. Materials and Methods

4.2.1. Material

To evaluate the individual and combined effects of particle shape and GSD on the mechanical response of coarse-grained soils, we prepared fifty-six particulate media samples by mixing different size fractions of particles with different shapes. We prepared these mixtures by combining fractions of well-rounded, very angular, or mixing two-particle shapes. We used uniform GB and CG to make the testing mixtures (Figure 4.2). First, we sieved GB and CG samples through consecutive sieve sizes to yield uniform particle fractions. Then, we sorted each particle size individually for later use in preparing the testing mixtures. We also measured the specific gravity (G_s) of the uniform GB and CG particles to accurately calculate the volumetric fraction of particles while making the testing mixtures. Table 4.1 summarizes the particles' mean particle size and shape properties of each of the GB and CG fractions. We used a Dino-Lite Pro Digital Microscope to capture images of at least 85 and 35 particles of CG and GB, respectively, for the particle shape analysis. We then calculated particle shape parameters (i.e., roundness and aspect ratio) using a MATLAB algorithm developed by Zheng and Hryciw (2015). Wadell (1932) defined roundness as:

$$R = \frac{\frac{1}{n}\sum_{i=1}^{n} r_n}{r_{inscribed}} \tag{19}$$

where n is the number of particle's corners, r_n is the radius of the circle fitted in the n^{th} corner, and $r_{inscribed}$ is the radius of the maximum inscribed circle in the 2D projection of the particle (Figure 4.3). The 2D aspect ratio is the ratio of the minimum to the maximum axes of the particle.

Using the GB and CG size fraction, we prepared mono-sized, bi-sized, and poly-sized mixtures; Figure 4.4 shows the GSD curves of the tested mixtures. The mono-sized mixtures included five different mean particle sizes (D_{50}), and coefficients of uniformity (C_u) are not greater than 1.1 (Figure 4.4a). In addition, we mixed two different mono-sized particles to create the bi-sized mixtures (Figures 4.4b, 4.3c, and 4.3d). Figures 4.4e and 4.3f present the GSD of the three and five-sized mixtures. To create those mixtures, we combined equal volume fractions of different particle sizes. First, we prepared the three-sized mixtures by composing three equal volume fractions of particles. Finally, we made the five-sized mixtures by mixing a 20% volume fraction of different uniform particles' sizes. Table 4.4 presents a matrix that includes particles' volumetric fractions, GSD properties, and the critical state parameters on each tested mixture's e-log(p').

For these mixtures made of different particle shapes, we calculated roundnesses by three methods: equivalent roundness based on the volume fraction, the number of particles, and the surface area (Alshammari and Fratta, 2023a). The following are equations for equivalent roundness:

$$R_{eq,V} = \frac{\sum_{n=1}^{m} R_n V_n}{\sum_{n=1}^{m} V_n} \qquad \textit{based on the volume fraction} \tag{20}$$

$$R_{eq,N} = \frac{\sum_{n=1}^{m} R_n V_n N_n}{\sum_{n=1}^{m} V_n N_n} \qquad \textit{based on the number of particles} \tag{21}$$

$$R_{eq,SA} = \frac{\sum_{n=1}^{m} R_n V_n SA_{100,n}}{\sum_{n=1}^{m} V_n SA_{100,n}} \qquad \textit{based on the surface area} \tag{22}$$

where m is the total number of mono-sized materials composing the mixture, R_n, V_n, and N_n are roundness, volume fraction, and the number of particles of the n^{th} sized fractions in the mixture.

$SA_{100,n}$ is the surface area of the mixtures' 100 mm^3 solid volume of the nth mono-sized material. Alshammari and Fratta (2023a) presented a complete discussion of these equivalent roundness measures. We present the equivalent roundnesses of the tested mixtures in Table 4.2.

4.2.2. CS Parameters Testing

We assessed the CS parameters of the testing mixtures using a modified version of the simple method proposed by Santamarina and Cho (2001). Their method is specified for coarse-grained soils and requires one specimen to obtain several points on the e-log(p') plane. First, the CS friction angle is estimated by the angle of repose measurement (Cornforth, 1973; Bolton, 1986). Santamarina and Cho (2001) used a 1000-mL cylinder to measure the angle of repose. After pouring the sample into the cylinder, the cylinder is tilted and slowly brought back to the original position. Then, the angle in the middle of the formed slope is measured. Then, Santamarina and Cho (2001) prepared a saturated specimen into a rubber membrane and isotopically stressed the specimen using vacuum pressure (σ'_{va}). Then, they sheared the specimen to about 40% of axial strain while measuring the volume change through a transparent hose. The vacuum pressure and rubber membrane resistance (σ'_{m}) provide effective stresses on the specimen. Therefore, the applied effective stress is:

$$\sigma'_3 = \sigma'_{va} + \sigma'_m \tag{23}$$

and the mean effective stress p' at the critical stress is:

$$p' = \sigma_3' \frac{3 - \sin(\emptyset_{cs})}{3[1 - \sin(\emptyset_{cs})]} \tag{24}$$

Santamarina and Cho (2001) measured the total volume of the sample (V_t) and the volume of apparatus without the soil, including membrane, caps, O-rings, and pre-determined part of the

transparent hose (V_a) using Archimedes' principle. Then, the void volume in the saturated sample (V_w) is calculated by:

$$V_w = V_t - V_a - V_s \tag{25}$$

where V_s is the volume of the solid particles. Finally, the critical state void ratio is calculated as:

$$e_{cr} = \frac{V_{w,cs}}{V_s} \tag{26}$$

where $V_{w,cs}$ is the void volume at the CS (i.e., V_w minus the volume change at 40% of axial strain). With multiple e_{cr} for different effective stresses p', the CSL is plotted, and then e_{1kPa} and λ parameters are calculated.

Santamarina and Cho (2001)'s method is simple and direct. As a result, the applied effective stresses on the soil sample are low, and they do not generate particle breakage or changes in the GSD (the effective stress needed to generate particle crushing in silica is about 3 MPa—Ghafghazi et al., 2014). Thus, by adopting Santamarina and Cho (2001)'s method, the intrinsic properties of our testing mixtures are less likely to change during the test; however, we modified their setup and procedure to improve the quality of the collected data.

4.2.2.1. The modified testing setup

Our modifications to Santamarina and Cho (2001)'s method include amending the apparatus and some procedures.

Table 4.3 summarizes our modifications and the proposed advantages of those modifications. For the CS friction angle measurement, we developed a novel imaging algorithm to calculate the slope angle of particulate materials in a rotating cylinder (details in Alshammari and Fratta, 2023b). With this method, we force particle remixing and therefore minimize particle segregation (Lee et al. (2007), as particle segregation was noted during the tilting cylinder measurements (Lee et al., 2007; Rousé, 2014). Another advantage of the procedure and algorithm is the reduction in operator bias. Using the algorithm, we measured the CS friction angle of the mixtures and documented our findings in Alshammari and Fratta (2023a). Here, we used those angle of repose measurements (i.e., CS friction angles) in Equation (24) to calculate the applied mean effective stresses on samples.

For assessing CS parameters on the e-log(p') plane, we prepared samples using the apparatus presented in Figure 4.5a. The complete setup includes a vacuum pump, regulator and pressure gauge, a flask, a graduated pipe, tubes, valves, quick couplings, platens topped with porous stones, rubber membrane and rubber bands, filter papers, and a syringe. Figure 4.5b shows an image of the prepared sample hooked to the system and ready for testing.

We added a flask between the vacuum source and the system to prevent the vacuum source from water suction. We also used rubber bands, instead of O-rings, to fix the membrane to the top and bottom platens. Rubber bands do not slide easily and provide a better grip between the membrane and the platens, especially during sample kneading, stretching, and axial deformation. Then, we used quick couplings to connect and disconnect the sample from the system.

We used the syringe to add a known volume of water to the tubes and sample. By measuring the volume of water going into the sample, we calculate the sample's void ratio avoiding submerging

the sample into the water to assess the system's volume. Finally, we connected the sample to the top and bottom platen pipes to allow water movement and ensure sample saturation (Figure 4.5b).

4.2.2.2. Sample preparation

We took several steps to prepare the sample for testing:

1. Put filter paper on the porous stone of the bottom platen (Figure 4.6). Next, stretch the rubber membrane and fit it around the platen. Then, extend rubber bands and put them on the platen to seal the membrane. The extended rubber bands exert sufficient pressure on the membrane to be fixed to the platen.
2. Fill the membrane with a pre-weighted mass of dry particles. The mass of particles should be enough to create a sample with a height about twice its diameter (Figure 4.6).
3. Put a filter paper on the top platen; then, while the membrane is standing vertical, stretch the open end and fit it around the top platen. Then, place the rubber bands on the platen to seal the membrane.
4. Connect the hose attached to the top platen with quick coupling. Keep the top platen's hose disconnected and hang it vertically to allow the venting of air (Figure 4.7).
5. Using the syringe, inject a known volume of de-aired water through the top of the graduated cylinder (Figure 4.7). While the water seeps into the sample through the hanging hose, ensure that water does not escape the system. Be sure that the system and the sample are dry.
6. After the water replaces most of the air in the sample, fit the top platen to the system using the quick coupling, and connect the graduated pipe with the vacuum line to the sample.
7. Close the bottom platen valve and apply vacuum pressure to remove air bubbles.

8. While the sample is under vacuum, close the top platen valve, open the bottom platen valve, and then release the vacuum. This step allows water circulation from the bottom to the top of the sample.
9. Repeat steps 7 and 8 until all air bubbles are removed. You can visually inspect air bubbles in the sample and pipes.
10. Ensure the graduated pipe's water level is in the measurable range that is in between the top and bottom tick marks of the pipe. The whole process should be repeated if water leaks out of the system while vacuuming the graduated pipe or injecting the water into the sample.

4.2.2.3. Calibration procedure

The experimental setup must be calibrated to ensure collecting accurate data:

1- Water volume between the last tick in the graduated pipe and the sample (V_{tube}). This water volume includes part of the graduated pipe, pipes connecting the sample to the graduated pipe, and porous stones, which do not represent the sample's void volume. To assess that additional volume, we repeated the sample preparation protocol without the sample while the two platens were in contact.

2- Pressure level needed to expand membrane diameter to 1.6 of the original size (i.e., σ'_m). This expansion is significant because the sample will be compressed and bulged to make a diameter about 1.6 times the original size. We used a 0.635 mm thick latex membrane and found that the water pressure needed to expand the membrane is about 11 kPa of pressure.

4.2.2.4. Data reduction

The mean effective stress is calculated using Equations (23) and (24). For each e_{cr} measurement, we calculate the porewater volume at the CS as:

$$V_{w,cs} = V_{sys} - V_{tube} - V_{pi} \quad (27)$$

where V_{sys} is water volume inserted into the system, and V_{pi} is water reading in the graduated pipe. Then, we compute the e_{cr} with Equation (26). We measured seven e_{cr} points for each tested mixture to fit the CSL on the e-log(p') plane.

4.3. Results and Interpretation

Since GSD reportedly controls the CS parameters on the e-log(p') plane (Wood and Maeda, 2008; Li et al., 2015; Xiao et al., 2016; Chang and Deng, 2020), we plotted the collected CS parameters of all testing mixtures against C_u in Figure 4.8. However, these results do not show a clear correlation, but separating the data based on particle shape provides a better understanding of the relationships between e_{1kPa} and C_u (Figure 4.8a). For example, e_{1kPa} decreases with increasing C_u for mixtures arranged by particle shape. Moreover, the CG mixtures have higher e_{1kPa} values than the GB mixtures, and the mixed-shape mixtures have e_{1kPa} values scattered between the values of the CG and GB mixtures (Figure 4.8a). These results show the importance of considering particle shape with the GSD to assess how e_{cr} evolves. For example, Youd (1973) suggested evaluating max and min void ratios based on particle shape and size range.

The fitting lines in Figure 4.8a show that individual particle shape mixtures yield a more robust fit than the mixed-shape mixtures. Nevertheless, the mixed-shape data show more scatter, possibly due to the variation of particle shape among different particle sizes. Figure 4.8b presents the

measured relationship between λ and C_u and particle shape. The data suggest no correlation between λ and C_u, but a stronger correlation between λ and particle shape. For instance, mixtures with one particle shape have similar λ values regardless of C_u; however, GB mixtures have lower λ values than the CG mixtures. These observations indicate a greater large-strain stiffness of GB mixtures than CG mixtures. This observation appears to relate to a lower range of e_{max}-e_{min} in GB mixtures, so GB mixtures create more compact structures than mixtures with angular particles (Cubrinovski and Ishihara, 2002; Cho et al., 2006; Sarkar et al., 2019). Overall, mixtures of mixed particle shapes yield a larger scatter in the measured λ values. Hence, the diversity in particle shape among different particle sizes of a mixture indicates a more complex critical state behavior. In-depth analyses of the e_{cr} data follow in the next sections.

4.3.1. Mono-sized Mixtures

To evaluate the effect of particle shape in each size fraction on the CSL, we tested and plotted the CSLs of different mono-sized particles in Figure 4.9a. The CSLs of GB mixtures plot close to each other on the e-log(p') because they have the same particle shape and gradation. Similarly, CG mixtures are in similar locations on the e-log(p') but have void ratios larger than GB mixtures. Also, the CSLs of CG are more dispersed than those of GB mixtures. We do not know the reason for this response, but we speculate that the different amounts of impurities in the recycled CG mono-sized mixtures might play a role. In Figures 4.9b and 4.8c, e_{1kPa} and λ are plotted versus roundness along with data from Cho et al. (2006). Both datasets show the same trend of decreasing e_{1kPa} and λ with roundness. However, the greater scatter in Cho et al. (2006)'s data in comparison with our data could be attributed to (1) particle shape measurements obtained using standard charts; (2) differences in the coefficient of uniformity; and (3) differences in the mineralogy.

Furthermore, Lashkari et al. (2020) and Torres-Cruz and Santamarina (2020) emphasized the effect of mineralogy on the critical state parameters on the e-log(p') plane.

We also prepared a class of mono-sized mixtures by combining GB and CG particles of the same mean particle size (D_{50} = 0.548 mm). Figure 4.10a documents the CSLs of these mixtures. The CSL shifts down on the e-log(p') plane, and the slope λ decreases when the percentage of the CG fraction decreases in the mixture. For example, e_{1kPa} and λ both decrease nearly linearly when the percentage of the GB volume fraction increases (Figure 4.10b). However, the rate of change of λ with percentage of GB volume fraction change at about 70%. This shows the effect of the GB on the CSL slope. It is worth noting that even though these GB and CG particles have the same mean particle size based on sieve analysis, the optical analysis revealed a larger size for CG particles (Alshammari and Fratta, 2023a). We discuss the effect of particle relative sizes on the critical state void ratio in the following two sections.

4.3.2. Bi-sized Mixtures

Lade et al. (1998), Thevanayagam et al. (2002), Papadopoulou and Tika (2008), Rahman et al. (2008), Carrera et al. (2011), and Yilmaz et al. (2021) studied liquefaction effect on gap-graded soils. As the small-size fraction increases in the bi-sized mixtures, characteristic void ratios (i.e., e_{min}, e_{max}, and e_{cr}) decrease. However, there is an optimal-small size fraction content, where void ratios reach the lowest possible values (Lade et al., 1998). Fractions beyond this optimal small-size fraction content cause the void ratios to increase. Furthermore, the lowest void ratios at the optimal-small size fraction decrease with the size ratio of the small and large particles. Based on published data, Zuo and Baudet (2015) showed that the optimal of the small-size fraction to achieve the lowest void ratios is between 20% and 50%.

We studied the effect of the small-size fractions on the CSLs of bi-sized mixtures. Figure 4.11a presents the evolution of the CSLs in GB mixtures composed of two mono-sized particles, D_{50} = 0.922 and 0.230 mm. The increase of the small particle fraction in the bi-sized mixtures shifts the CSLs down on the e-log(p') plane until about 40% volume fraction of the small-size fraction. Then, the CSLs shift gradually until the effect disappears as the volume of small-size fractions increases. This behavior agrees with findings by Zuo and Baudet (2015). They stated that the lowest void ratios are attained with small fractions between 20% and 50%. In light of this information, we argue that the CLS returns approximately to the original position because the large and small particles have similar particle shapes at the two extremes. However, when particle shapes differ, the CSL evolves differently (Figure 4.11b). Mixing 20% volume fraction of small CG particles (i.e., D_{50} = 0.230 mm) with the large GB particles, drops the CSL position on the e-log(p') plane. Then, adding more volume of CG particles shifts the CSL position until it reaches the CSL position of 100% CG particles, which is higher than the position of the critical state line for GB particles.

Moreover, the CSL slope λ increases with the CG fraction in the mixture. This CS behavior is different from the GB bi-sized mixtures in Figure 4.11a. Figure 4.12 captures these two different behaviors. CG particles create a more open fabric than GB particles, so CG mixtures attain a larger total volume than GB mixtures for the same solid volume. Therefore, a smaller number of CG particles is needed to fill the voids of the larger GB and achieve the lowest void ratio of the bi-sized mixture.

Figure 4.13 shows CSLs for bi-sized mixtures made of D_{50} = 0.922 and 0.548 mm particles. In Figure 4.13a, both particle size fractions are GB, while in Figure 4.13b, the large size fraction is GB, and the small size fraction is CG. The CSL shifts down minimally with the addition of the

small particle fraction (Figure 4.13a). This small change suggests that the small particles are not filling the voids left by the large particles. In the case of small CG particles (i.e., Figure 4.13b), the CSLs shift up on the e-log(p') plane with the increase of CG small-size volume fractions.

CSLs of the bi-sized CG mixtures made with D_{50} = 0.653 and 0.326 mm particles are presented in Figure 4.14a. The CSLs initially shift down until the 40% volume of the small-size fraction is reached, then the CSLs shift up again. Although the small to large particle size ratio is relatively high (i.e., $\frac{D_{50,Small,CG}}{D_{50,Large,CG}} = 0.5$ is close to the ratio of GB bi-sized mixtures in Figure 4.13a that show minor sensitivity of the CSLs to the increase in small-size fractions). The displacement of the CSL first down, then up is apparent. We attribute that pattern to the higher void ratio created by the CG particles, so small CG particles can fit into the voids between large particles. In Figure 4.14b, we replace the small size fraction with GB particles. The CSL moves down with the addition of a small GB fraction, and then at 60% volume fraction of the small GB, the CSL almost stabilizes with higher increases in GB volumes. This behavior is caused by GB particles separating the large CG particles, and that effect completes at a 60% volume fraction.

4.3.2.1. e_{1kPa} of the Bi-sized Mixtures

To better study the combined effect of particle relative size and shape, we plotted the e_{1kPa} against the volume fraction of small or large particles in the upper x-axis (Figure 4.15). The data of bi-sized mixtures in Figures 4.11, 4.13, and 4.14 are replotted in Figures 4.15a, 4.14b, and 4.14c, respectively. These results show that the particle shape of the small particle volume fraction controls when the small-size particle fraction achieves the lowest void ratio and how the e_{cr} advance as the small size fraction increases in the bi-sized mixture (Figure 4.15a). Furthermore,

the particle shape of large particles dictates the void ratio of the mixture. So, the small particles may not fit into the small voids formed by the large particles (GB bi-sized mixtures in Figure 4.15b). On the other hand, the small CG particles fit between the larger voids created by the large CG particles (CG bi-sized mixtures in Figure 4.15c).

4.3.2.2. λ of the Bi-sized Mixtures

The slope λ of the bi-sized mixture changes upon varying the volume fractions of the particle fractions. Figure 4.16 reveals the effect of increasing the small volume fraction in the bi-sized mixtures made with one particle type on λ. The variation of the λ is weak and does not show a clear trend with changes in the size volume fraction (i.e., the response is insensitive to changes in GSD). However, λ is sensitive to particle shape. If one size fraction in the bi-size mixture has a different particle shape, the λ response is different. Figure 4.17 presents λ data of the bi-sized mixtures of different particle shapes. Intuitively, increasing the GB fraction decreases the slope λ. However, the GB fraction's effect diminishes if CG's relative size decreases. For instance, when the mean particle size ratio of CG to GB is 0.25, a 20% volume fraction of CG in the bi-sized mixture considerably increases λ. Furthermore, when the D_{50} of the CG particles is twice the D_{50} of the GB particles, the effect of the CG on the λ is weak for the first 40% volume fraction of the CG. Finally, we also noted the response on the effect of the relative size of the CG fraction on the critical state friction angle (Alshammari and Fratta, 2023a).

4.3.3. Poly-sized Mixtures

We created poly-sized mixtures by mixing the same volumes of different fraction sizes of particles. For example, we made three-sized mixtures by mixing three mono-sized fractions with D_{50} = 0.922, 0.548, and 0.326 mm. Each one of these fractions occupied 33% of the mixture's solid volume. While we created the five-sized mixtures (Table 4.1) by mixing mono-sized fractions, each occupies 20% of the solid volume. Figures 4.18a and 4.19a show the GB poly-sized materials made of GB or GB with one size fraction replaced by CG particles. In these mixtures, the CSL shifts as one size fraction of CG replaces the same size GB fraction. Note that the CSL position and slope increase with the decrease in CG relative size.

Figures 4.18b and 4.19b show the CSLs of CG poly-sized mixtures. We made these mixtures by combining CG particles with one size fraction replaced by GB particles. The presence of GB particles on the CG mixtures lowers the position of CSL. This shift is significant when the GB size fraction replaces smaller particle sizes. Figure 4.20 summarizes the critical state parameters results. The effect of the CG particles on GB three-sized mixtures is more pronounced than that of GB particles on the CG three-sized mixtures. This effect increases inversely with the relative size of the intruded particles.

Moreover, the effect of the intruded GB on λ of the CG three-sized mixtures is small. For example, Figure 4.21 presents the CS parameters of Five-sized mixtures where the effect of the intruded GB on λ of the CG five-sized mixtures is noticeable but minor. The last mixture in Figure 4.21, composed of CG particles with the smallest size fraction replaced by GB, had the lowest e_{1kPa} value in the CG five-sized mixtures for two reasons. First, the behavior follows the trend of decreasing e_{1kPa} with decreasing GB relative size. Second, the replaced CG particles (D_{50} = 0.230

mm) show the highest e_{1kPa} among the mono-sized CG mixtures (for example, see mixture No. 10 in Figure 4.9a). Therefore, the e_{1kPa} of the last mixture in Figure 4.21 is slightly lower than the trend.

4.4. Correlations of CS Parameters with Particles Shape

Since we did not establish a strong correlation between C_u and λ, we correlate λ only with equivalent roundnesses to evaluate the best performing equivalent roundness.

Figure 4.22 presents the correlations between λ of all testing mixtures and equivalent roundnesses. All equivalent roundnesses correlate with λ and generate similar fitting equations but different coefficients of determination. For example:

$$\lambda = 0.11 - 0.08R_{eq,V} \qquad (r^2 = 0.78) \tag{28}$$

$$\lambda = 0.11 - 0.08R_{eq,N} \qquad (r^2 = 0.83) \tag{29}$$

$$\lambda = 0.11 - 0.08R_{eq,SA} \qquad (r^2 = 0.89) \tag{30}$$

The equivalent roundness based on surface area performed the best because it has the highest r^2. A similar conclusion was found while correlating equivalent roundnesses with the critical state friction angle (Alshammari and Fratta, 2023a).

e_{1kPa} showed sensitivity to both the particle shape and coefficient of uniformity. Therefore, we correlated e_{1kPa} with $R_{eq,SA}$, and C_u. The fitting model of data is a plane:

$$e_{1kPa} = 1.41 - 0.59R_{eq,SA} - 0.08C_u \qquad (r^2 = 0.91) \tag{31}$$

The fitting model has high predictability of the data (i.e., $r^2 = 0.91$), and Figure 4.23 shows different views of the fitting model in a 3D plot. e_{1kPa} decreases with the increase in roundness and

coefficient of uniformity. So, we can use Equations (16) and (17) to locate the CSL line on the e-log(p') based on intrinsic parameters: roundness and coefficient of uniformity.

4.5. Conclusions

We conducted an experimental study to evaluate the combined effect of particle shape and grain size distribution on the critical state parameters on the e-log(p') plane. The testing methodology is a modified version of the simple testing procedure proposed by Santamarina and Cho (2001). We revised their test to facilitate sample setup, saturation, and void ratio measurement. We tested fifty-six mixtures that vary in particle shape and gradation to evaluate the individual and combined effect of particle shape and gradation on the e_{cr}. We concluded the following:

- The C_u is the controlling factor that dictates the CSL position on the e-log(p') plane. However, the C_u alone cannot estimate the CSL location.
- Round particles attain lower CSL positions than angular particles. For constant particle shape, CLS shifts down with higher C_u. However, if particle shape changes among different particle sizes in the same particulate material, the behavior is complex and is weakly correlated with the C_u.
- In bi-sized mixtures, the small size fraction decreases the CSL position on e-log(p') to then, after the threshold of the small size fraction, the CSL shifts up.
- An optimum small-size fraction percentage that achieves the minimum e_{1kPa} depends not only on the size ratio of small to large particles but also on the particle shape of the small and large particles.

- Angular particles form a larger total volume than round particles for the same solid volume. Therefore, small angular particles fill voids of the larger particle with less volume than small round particles.
- The particle shape of the small size fraction has more influence on the λ than the large size fraction.
- $R_{eq,SA}$ is an equivalent roundness calculated based on a particle's surface area. This parameter correlates well with the slope of CSL. e_{1kPa} is sensitive to both particle shape and coefficient of uniformity. A plane fitting model is developed to predict e_{1kPa} based on $R_{eq,SA,}$ and C_u. So, we can estimate the location of the CSL line on the e-log(p') based on intrinsic parameters: roundness and coefficient of uniformity.

4.6. Acknowledgments

The scholarship by King Fahd University of Petroleum and Minerals (KFUPM) through the Saudi Arabian Cultural Mission (SACM) and the funds from the Wisconsin Department of Transportation (WisDOT) supported this research.

4.7. References

Alshammari, A. M., and Fratta, D. (2023a). The combined effect of gradation and particle shape on coarse-grained soils' critical state friction angle. To be Submitted for publication.

Alshammari, A. M., and Fratta, D. (2023b). An image processing algorithm to systematically evaluate the angle of repose and void ratio of particulate media. To be Submitted for publication.

Been, K., and Jefferies, M. G. (1985). A state parameter for sands. *Géotechnique*, *35*(2), 99-112.

Bolton, M. D. (1986). The strength and dilatancy of sands. Geotechnique, 36(1), 65-78.

Carrera, A., Coop, M. R., and Lancellotta, R. (2011). Influence of grading on the mechanical behaviour of Stava tailings. *Géotechnique*, *61*(11), 935-946.

Chang, C. S., and Deng, Y. (2020). Modeling for critical state line of granular soil with evolution of grain size distribution due to particle breakage. *Geoscience Frontiers*, *11*(2), 473-486.

Cornforth, D. H. (1973). "Prediction of Drained Strength of Sands from Relative Density Measurements," Evaluation of Relative Density and Its Role in Geotechnical Projects Involving Cohesionless Soils, ASTM STP 523, American Society for Testing and Materials, Philadelphia, p. 281–303.

Cubrinovski, M., and Ishihara, K. (2002). Maximum and minimum void ratio characteristics of sands. *Soils and foundations*, *42*(6), 65-78.

Dafalias, Y. F. (1986). An anisotropic critical state soil plasticity model. *Mechanics Research Communications*, *13*(6), 341-347.

Ghafghazi, M., Shuttle, D.A. and DeJong, J.T. (2014). Particle breakage and the critical state of sand. *Soils and Foundations*, 54(3), 451-461.

Lade, P. V., Liggio, C. D., and Yamamuro, J. A. (1998). Effects of non-plastic fines on minimum and maximum void ratios of sand. *Geotechnical testing journal*, *21*, 336-347.

Lashkari, A., Falsafizadeh, S. R., Shourijeh, P. T., and Alipour, M. J. (2020). Instability of loose sand in constant volume direct simple shear tests in relation to particle shape. *Acta Geotechnica*, *15*(9), 2507-2527.

Lee, J. S., Guimaraes, M. S., and Santamarina, J. C. (2007). Micaceous sands: Microscale mechanisms and macroscale response. *Journal of Geotechnical and Geoenvironmental Engineering*, *133*(9), 1136-1143.

Li, G., Liu, Y. J., Dano, C., and Hicher, P. Y. (2015). Grading-dependent behavior of granular materials: from discrete to continuous modeling. *Journal of Engineering Mechanics-ASCE*, *141*(6).

Papadopoulou, A., and Tika, T. (2008). The effect of fines on critical state and liquefaction resistance characteristics of non-plastic silty sands. *Soils and Foundations*, *48*(5), 713-725.

Rahman, M. M., Lo, S. R., and Gnanendran, C. T. (2008). On equivalent granular void ratio and steady state behaviour of loose sand with fines. *Canadian Geotechnical Journal*, *45*(10), 1439-1456.

Roscoe, K. H., Schofield, A., and Wroth, A. P. (1958). On the yielding of soils. *Geotechnique*, *8*(1), 22-53.

Rousé, P. C. (2014). Comparison of methods for the measurement of the angle of repose of granular materials. *Geotechnical Testing Journal*, *37*(1), 164-168.

Santamarina, J. C., and Cho, G. C. (2001). Determination of critical state parameters in sandy soils—simple procedure. *Geotechnical Testing Journal*, *24*(2), 185-192.

Sarkar, D., Goudarzy, M., and König, D. (2019). An interpretation of the influence of particle shape on the mechanical behavior of granular material. *Granular Matter*, *21*(3), 1-24.

Schofield, A. N., and Wroth, P. (1968). *Critical state soil mechanics* (Vol. 310). London: McGraw-hill.

Thevanayagam, S., Shenthan, T., Mohan, S., and Liang, J. (2002). Undrained fragility of clean sands, silty sands, and sandy silts. *Journal of Geotechnical and Geoenvironmental Engineering*, *128*(10), 849-859.

Torres-Cruz, L. A., and Santamarina, J. C. (2020). The critical state line of nonplastic tailings. *Canadian Geotechnical Journal*, *57*(10), 1508-1517.

Wadell, H. (1932). Volume, shape, and roundness of rock particles. *The Journal of Geology*, *40*(5), 443-451.

Wu, Y., Cui, J., Huang, J., Zhang, W., Yoshimoto, N., and Wen, L. (2021). Correlation of critical state strength properties with particle shape and surface fractal dimension of clinker ash. *International Journal of Geomechanics*, *21*(6), 04021071.

Wood, D. M. (1990). *Soil behaviour and critical state soil mechanics*. New York: Cambridge university press.

Wood, D. M., and Maeda, K. (2008). Changing grading of soil: effect on critical states. *Acta Geotechnica*, *3*(1), 3.

Xiao, Y., Liu, H., Ding, X., Chen, Y., Jiang, J., and Zhang, W. (2016). Influence of particle breakage on critical state line of rockfill material. *International Journal of Geomechanics*, *16*(1), 04015031.

Yang, J., and Luo, X. D. (2015). Exploring the relationship between critical state and particle shape for granular materials. *Journal of the Mechanics and Physics of Solids*, *84*, 196-213.

Yilmaz, Y., Deng, Y., Chang, C. S., and Gokce, A. (2021). Strength–dilatancy and critical state behaviours of binary mixtures of graded sands influenced by particle size ratio and fines content. *Géotechnique*, 1-16.

Youd, T. L. (1973). Factors controlling maximum and minimum densities of sands. *Evaluation of relative density and its role in geotechnical projects involving cohesionless soils*, *523*, 98.

Zheng, J., and Hryciw, R. D. (2015). Traditional soil particle sphericity, roundness and surface roughness by computational geometry. *Géotechnique*, *65*(6), 494-506.

Zuo, L., and Baudet, B. A. (2015). Determination of the transitional fines content of sand-non plastic fines mixtures. *Soils and Foundations*, *55*(1), 213-219.

Table 4.1: Size and particle shape properties of the uniform GB and CG.

Material		**Glass Beads**					**Crushed Glass**				
D_{50} (mm)		**0.922**	**0.653**	**0.548**	**0.326**	**0.23**	**0.922**	**0.653**	**0.548**	**0.326**	**0.23**
Sieve #		**18–20**	**25–30**	**30–35**	**45–50**	**60–70**	**18–20**	**25–30**	**30–35**	**45–50**	**60–70**
G_s		2.49	2.49	2.49	2.48	2.46	2.50	2.52	2.51	2.51	2.51
R	**Average**	0.99	0.96	0.95	0.95	0.97	0.26	0.24	0.26	0.30	0.29
	SD	0.01	0.07	0.12	0.09	0.06	0.06	0.06	0.11	0.07	0.09
AR	**Average**	0.97	0.97	0.96	0.96	0.99	0.69	0.69	0.65	0.69	0.64
	SD	0.02	0.04	0.09	0.09	0.03	0.12	0.13	0.16	0.15	0.15

NOTE: D_{50} is the mean particle size, Sieve# is the passed-retained sieve number, G_s is the specific gravity, R is the roundness, AR is the aspect ratio, and SD is the standard deviation.

Table 4.2: Equivalent roundnesses calculated based on volume fraction, number of particles, and surface area of the testing mixtures (Alshammari and Fratta, 2023a).

Mixture	R_V	$R_{eq,N}$	$R_{eq,SA}$	Mixture	R_V	$R_{eq,N}$	$R_{eq,SA}$
1	0.99	0.99	0.99	29	0.71	0.33	0.50
2	0.96	0.96	0.96	30	0.85	0.37	0.67
3	0.95	0.95	0.95	31	0.29	0.30	0.29
4	0.95	0.95	0.95	32	0.28	0.30	0.29
5	0.97	0.97	0.97	33	0.26	0.29	0.27
6	0.26	0.26	0.26	34	0.25	0.28	0.26
7	0.24	0.24	0.24	35	0.38	0.81	0.50
8	0.26	0.26	0.26	36	0.52	0.89	0.67
9	0.30	0.30	0.30	37	0.67	0.93	0.79
10	0.29	0.29	0.29	38	0.81	0.94	0.88
11	0.40	0.49	0.42	39	0.96	0.95	0.96
12	0.54	0.66	0.56	40	0.28	0.29	0.28
13	0.68	0.78	0.70	41	0.75	0.52	0.65
14	0.81	0.87	0.83	42	0.74	0.89	0.77
15	0.96	0.95	0.96	43	0.72	0.94	0.84
16	0.97	0.96	0.96	44	0.49	0.88	0.64
17	0.97	0.96	0.97	45	0.50	0.49	0.51
18	0.98	0.97	0.98	46	0.52	0.34	0.43
19	0.98	0.97	0.97	47	0.96	0.97	0.96
20	0.98	0.97	0.97	48	0.27	0.29	0.28
21	0.98	0.97	0.98	49	0.82	0.96	0.88
22	0.99	0.97	0.98	50	0.83	0.95	0.87
23	0.41	0.33	0.37	51	0.83	0.88	0.81
24	0.55	0.42	0.49	52	0.83	0.62	0.74
25	0.70	0.55	0.63	53	0.42	0.33	0.39
26	0.84	0.72	0.79	54	0.41	0.36	0.40
27	0.43	0.30	0.34	55	0.40	0.55	0.47
28	0.57	0.31	0.41	56	0.41	0.84	0.55

Note: R_V: equivalent roundness based on the volume fraction.
$R_{eq,N}$: equivalent roundness based on the number of particles.
$R_{eq,SA}$: equivalent roundness based on the surface area.

Table 4.3: Our modifications to Santamarina and Cho (2001)'s method with the advantages of those modifications.

Apparatus / Procedure	Santamarina and Cho (2001)'s method	Our modifications	Advantages of the modifications
The angle of repose	Tilting graduating cylinder along the vertical direction	Rotating cylinder with a novel algorithm to calculate the angle of the slope	• Reduces particle segregation • Consistency of measurements • Rapid multiple measurements for statistical calculations
Lines connected to the vacuum	One	Two	• Better water circulation through the sample • Simplified air removal from the sample
Saturation	During soil placement into the membrane. Then, vacuuming and kneading the sample	After placing the sample into the membrane and connecting the sample to the system	• Ability to measure how much water volume is in the system
Flask between the vacuum source and the system	None	Yes	• Preventing vacuum pump from water suction
Porewater volume measurement	Volume evaluation using Archimedes' principle	Pre-measured volume of water seeps into the specimen	• Simple and precise measurements.
Tubes connections in the system	None	Valves and quick couplings	• Simple handling • Improved saturation

Table 4.4: Mixtures properties and CSL parameters.

Mixture	Material	Glass Beads (%)					Crushed Glass (%)					GSD Properties		CSL Parameters on e-log(p')		
	D_{50} (mm)	0.922	0.653	0.548	0.326	0.230	0.922	0.653	0.548	0.326	0.230					
	Sieve #	18/20	25/30	30/35	45/50	60/70	18/20	25/30	30/35	45/50	60/70	C_u	C_c	D_{50} (mm)	λ	e_{1kPa}
1	Mono-sized	100										1.08	0.98	0.922	0.028	0.780
2			100									1.09	0.98	0.653	0.033	0.806
3				100								1.10	0.98	0.548	0.03	0.779
4					100							1.09	0.98	0.326	0.015	0.754
5						100						1.09	0.98	0.230	0.018	0.803
6							100					1.08	0.98	0.922	0.082	1.202
7								100				1.09	0.98	0.653	0.083	1.206
8									100			1.10	0.98	0.548	0.081	1.166
9										100		1.09	0.98	0.326	0.07	1.196
10											100	1.09	0.98	0.230	0.086	1.321
11				20					80			1.10	0.98	0.548	0.068	1.103
12				40					60			1.10	0.98	0.548	0.056	1.021
13				60					40			1.10	0.98	0.548	0.049	0.945
14				80					20			1.10	0.98	0.548	0.034	0.863
15	Bi-sized	20		80								1.12	0.98	0.560	0.023	0.754
16		40		60								1.16	0.97	0.582	0.028	0.744
17		60		40								1.71	0.70	0.873	0.034	0.761
18		80		20								1.68	1.49	0.903	0.035	0.783
19		20				80						1.11	0.98	0.235	0.017	0.688
20		40				60						1.15	0.97	0.243	0.016	0.552
21		60				40						4.06	0.29	0.873	0.021	0.489
22		80				20						4.00	3.55	0.903	0.024	0.583
23		20							80			1.12	0.98	0.560	0.078	1.107
24		40							60			1.16	0.97	0.582	0.068	1.000
25		60							40			1.71	0.70	0.873	0.058	0.905
26		80							20			1.68	1.49	0.903	0.046	0.828
27		20									80	1.11	0.98	0.235	0.081	1.139
28		40									60	1.15	0.97	0.243	0.082	0.963
29		60									40	4.06	0.29	0.873	0.078	0.777
30		80									20	4.00	3.55	0.903	0.074	0.722
31								20		80		1.11	0.98	0.333	0.087	1.194
32								40		60		1.15	0.97	0.345	0.083	1.120
33								60		40		2.03	0.58	0.617	0.089	1.075
34								80		20		2.00	1.76	0.639	0.085	1.085
35					20			80				2.00	1.76	0.639	0.069	1.021
36					40			60				2.03	0.58	0.617	0.051	0.876
37					60			40				1.15	0.97	0.345	0.026	0.763
38					80			20				1.11	0.98	0.333	0.022	0.773
39	Poly-sized	33		33	33							1.83	0.67	0.548	0.017	0.657
40							33		33	33		1.83	0.67	0.548	0.071	0.963
41		33		33						33		1.83	0.67	0.548	0.063	0.806
42		33			33				33			1.83	0.67	0.548	0.053	0.762
43				33	33		33					1.83	0.67	0.548	0.026	0.714
44					33		33		33			1.83	0.67	0.548	0.071	0.896
45				33			33			33		1.83	0.67	0.548	0.071	0.894
46		33							33	33		1.83	0.67	0.548	0.076	0.941
47		20	20	20	20	20						2.61	0.77	0.548	0.032	0.591
48							20	20	20	20	20	2.61	0.77	0.548	0.084	0.994
49		20		20	20	20		20				2.61	0.77	0.548	0.036	0.671
50		20	20		20	20			20			2.61	0.77	0.548	0.046	0.701
51		20	20	20		20				20		2.61	0.77	0.548	0.054	0.719
52		20	20	20	20						20	2.61	0.77	0.548	0.057	0.736
53			20				20		20	20	20	2.61	0.77	0.548	0.086	0.945
54				20			20	20		20	20	2.61	0.77	0.548	0.079	0.907
55					20		20	20	20		20	2.61	0.77	0.548	0.074	0.889
56						20	20	20	20	20		2.61	0.77	0.548	0.069	0.863

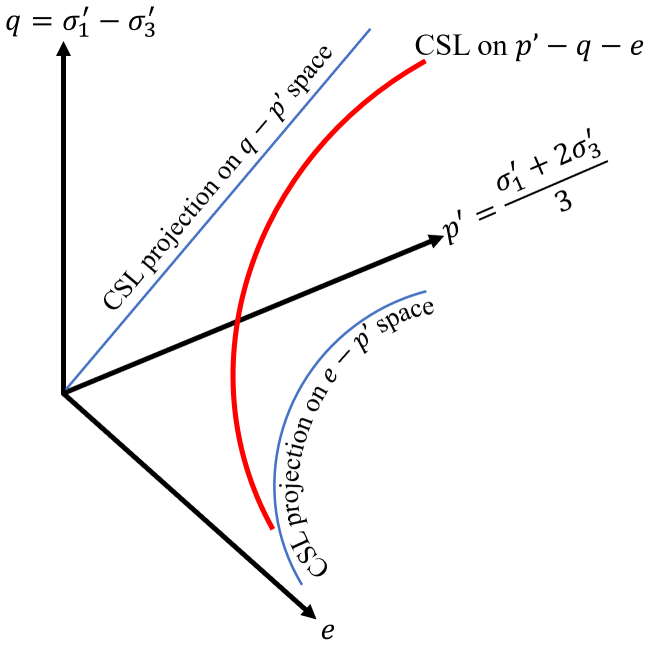

Figure 4.1: 3D representation of the CSL and its projections onto q-p' and e-p' spaces.

D_{50} (mm)	0.922	0.653	0.548	0.326	0.230
Sieve No. (passed-retained)	18-20	25-30	30-35	45-50	60-70
Glass bead (GB) particle fractions	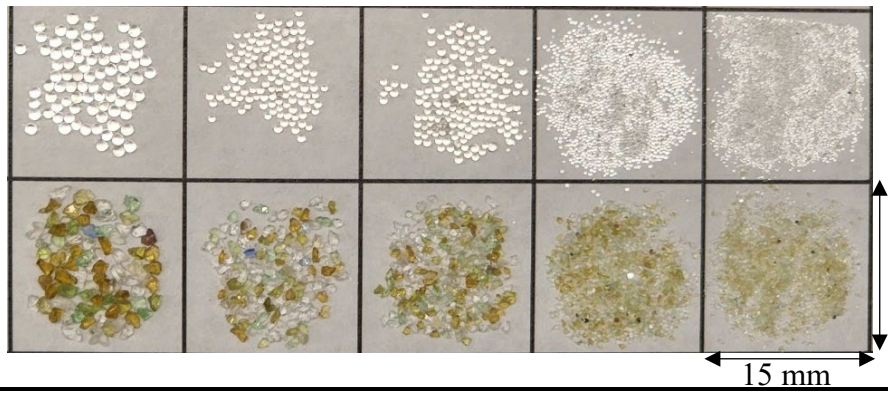				
Crushed glass (CG) particle fractions					

Figure 4.2: Photographs of the mono-sized GB and CG particles used to make the testing mixtures.

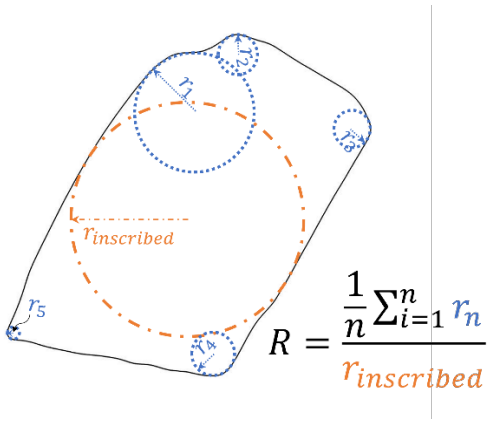

Figure 4.3: Roundness definition: the average of radii of circles fitted in the particle major features divided by the radius of the maximum inscribed circle.

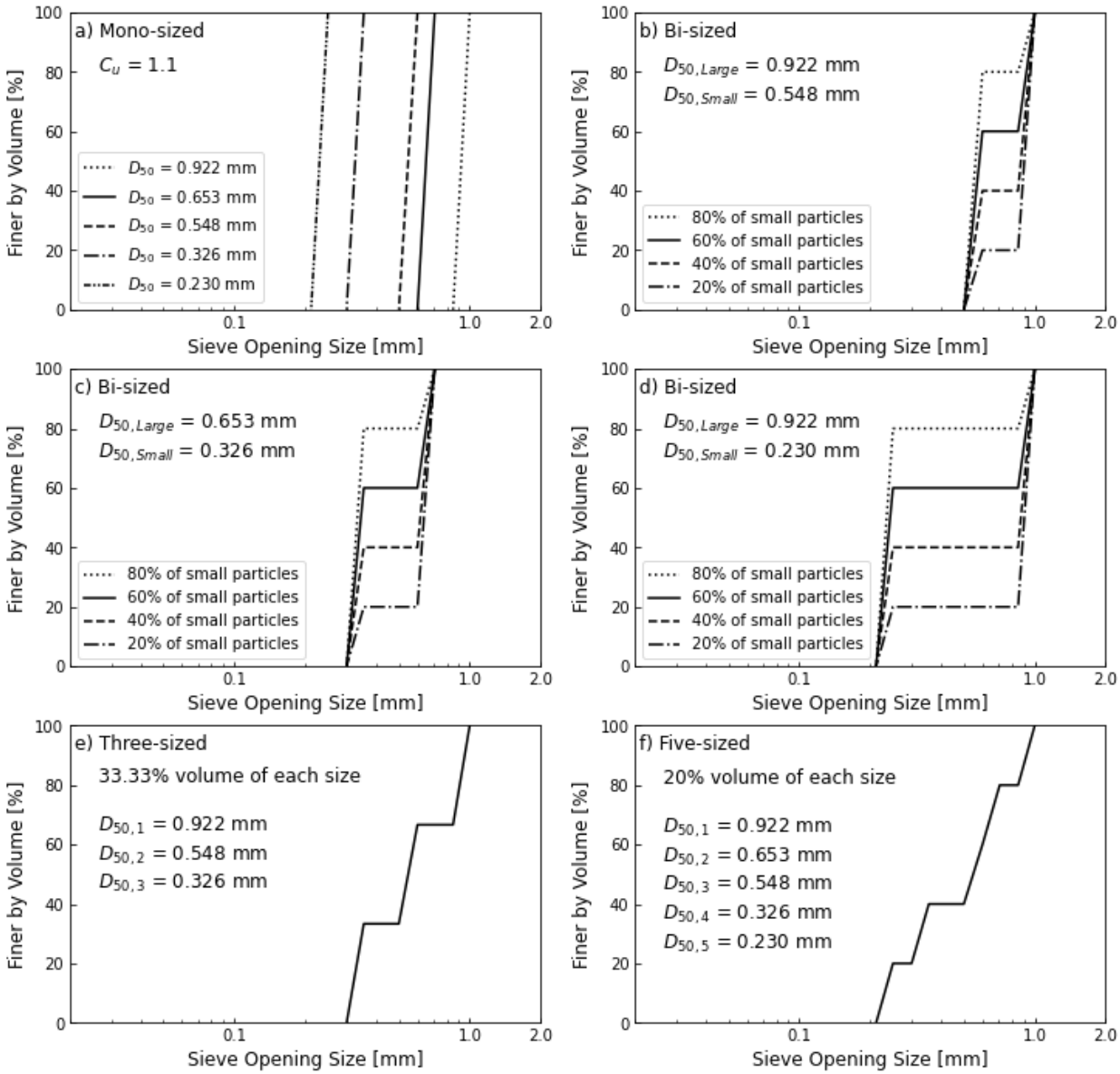

Figure 4.4: GSD curves for the testing mixtures: (a) mono-sized mixtures, (b) bi-sized mixtures made of D_{50} = 0.922 and 0.548 mm mono-sized particles, (c) bi-sized mixtures made of D_{50} = 0.653 and 0.326 mm mono-sized particles, (d) bi-sized mixtures made of D_{50} = 0.922 and 0.230 mm mono-sized particles, (e) three-sized mixtures made of D_{50} = 0.922, 0.548 and 0.326 mm particle size where each particle has the same volume fraction of 33%, and (f) five-sized mixtures made by combining 20% volume of each of the mono-sized particles.

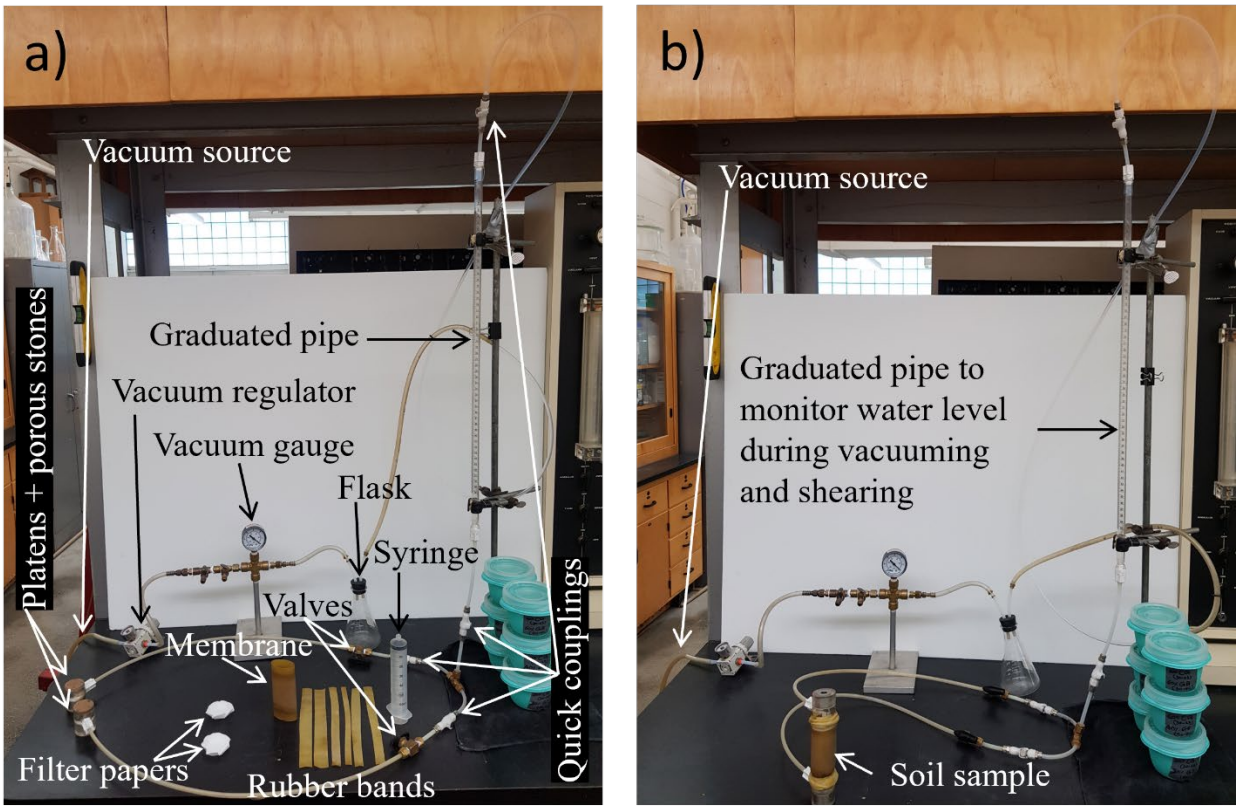

Figure 4.5: (a) complete testing apparatus, and (b) sample ready for testing.

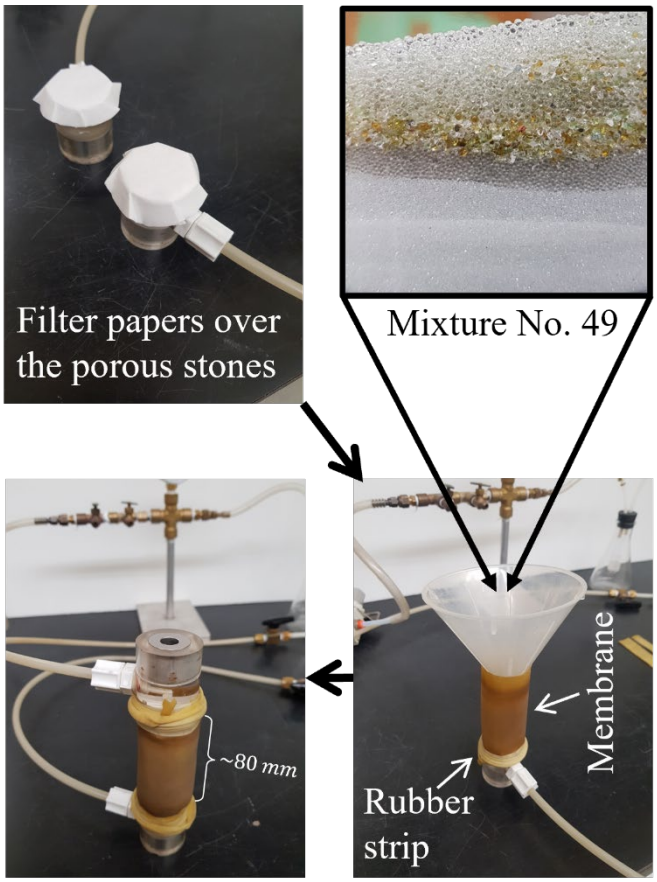

Figure 4.6: Sample preparation steps.

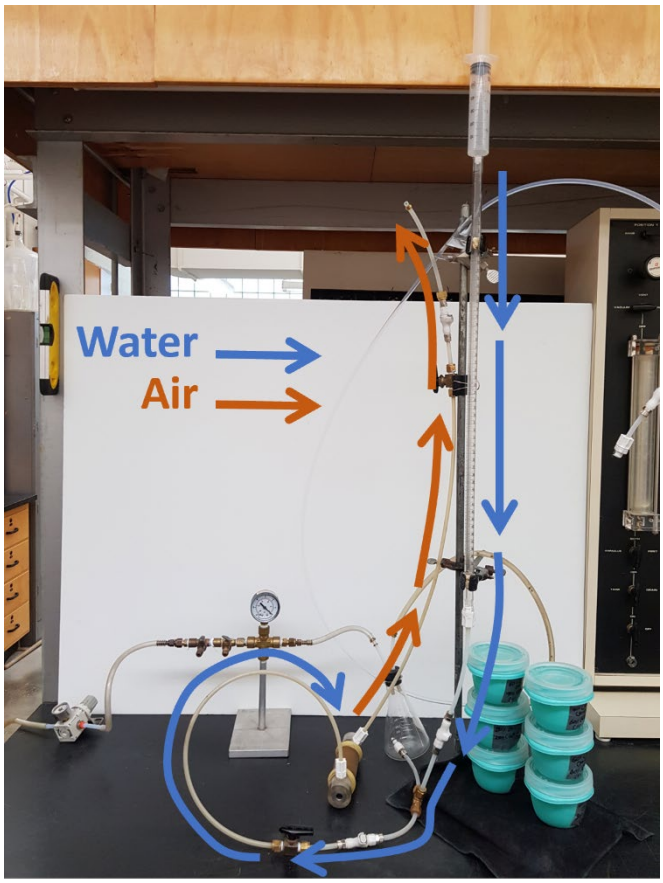

Figure 4.7: Process for sample saturation.

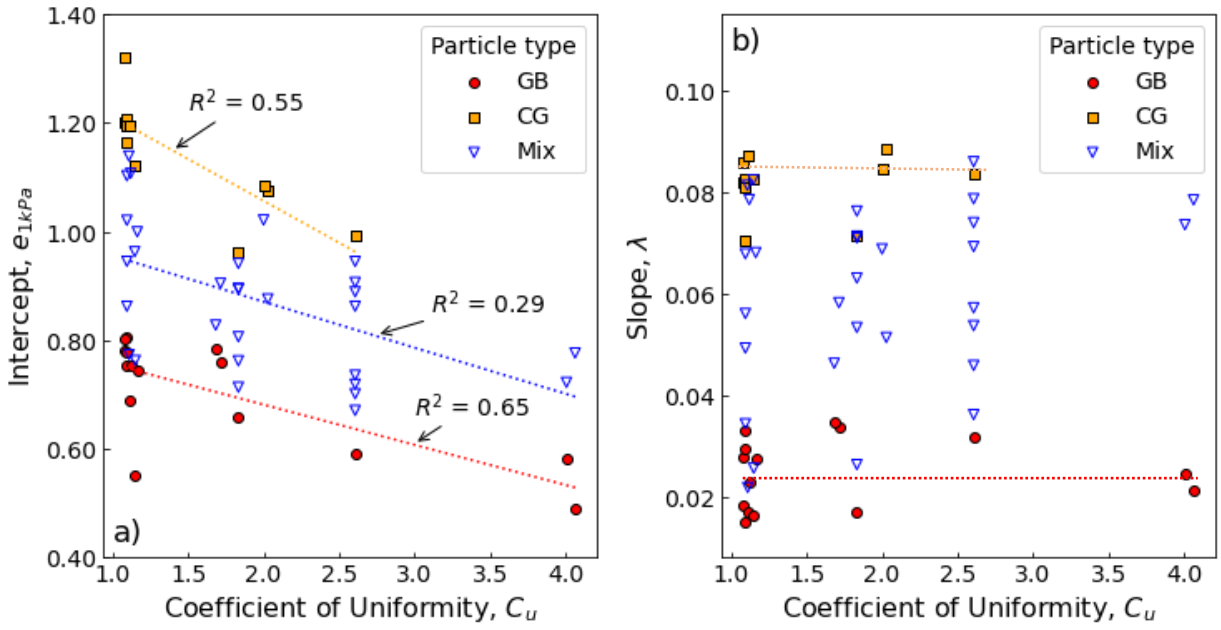

Figure 4.8: Critical state parameters of all mixtures against C_u: (a) CS void ratio intercept, e_{1kPa}; (b) the slope, λ.

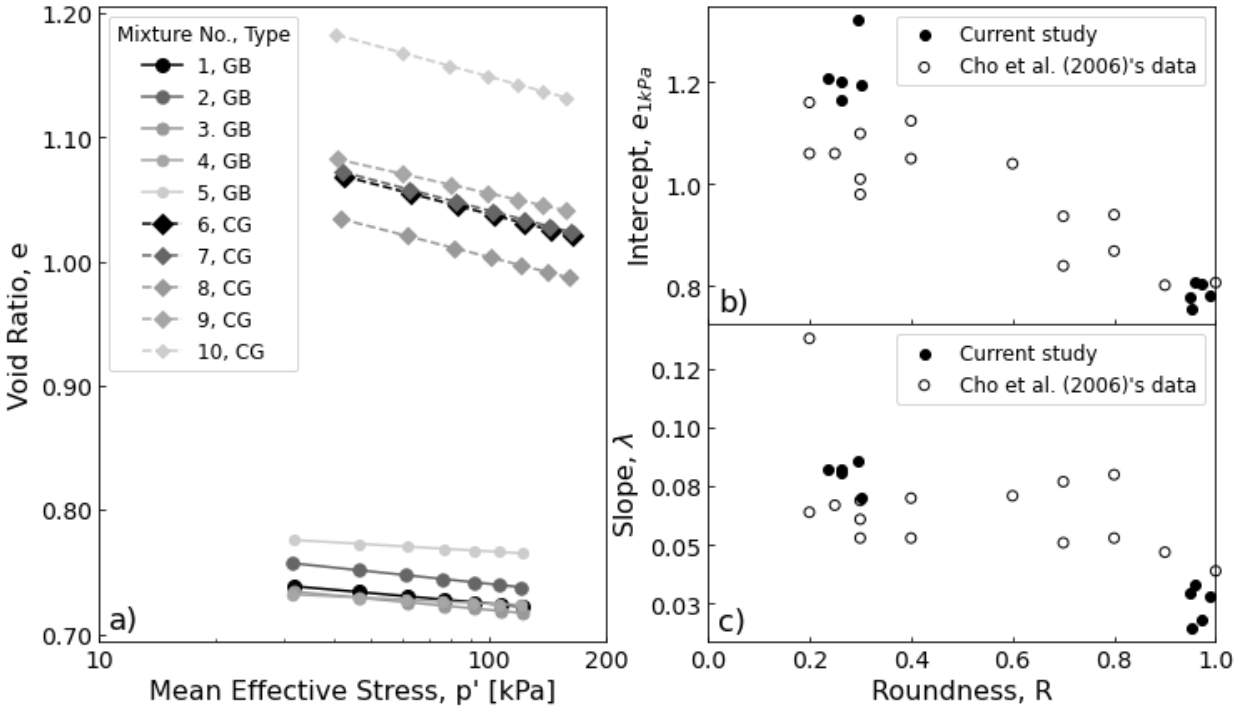

Figure 4.9: (a) CSLs for the mono-sized mixtures made of CG or GB particles, (b) e_{1kPa}, and (c) λ versus roundness.

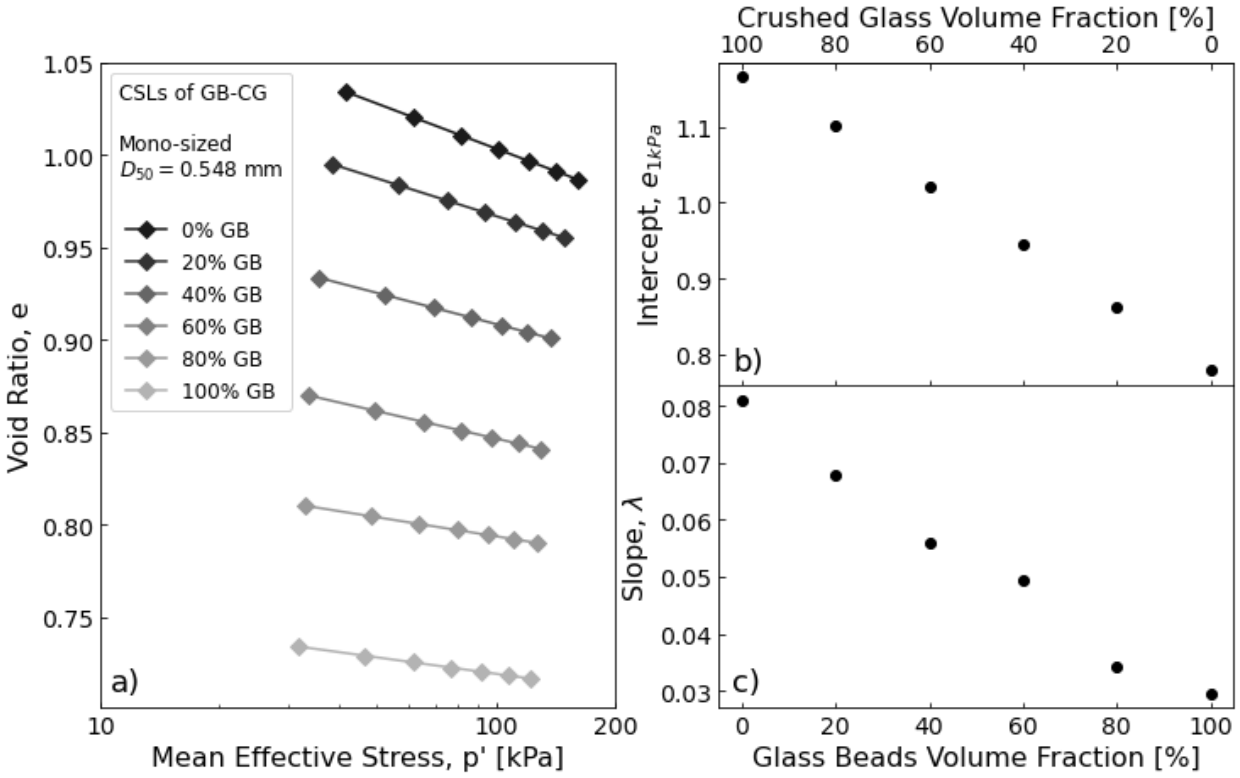

Figure 4.10: (a) CSLs of mono-sized GB-CG mixtures with D_{50} = 0.548 mm, (b) e_{1kPa}, and (c) λ versus roundness.

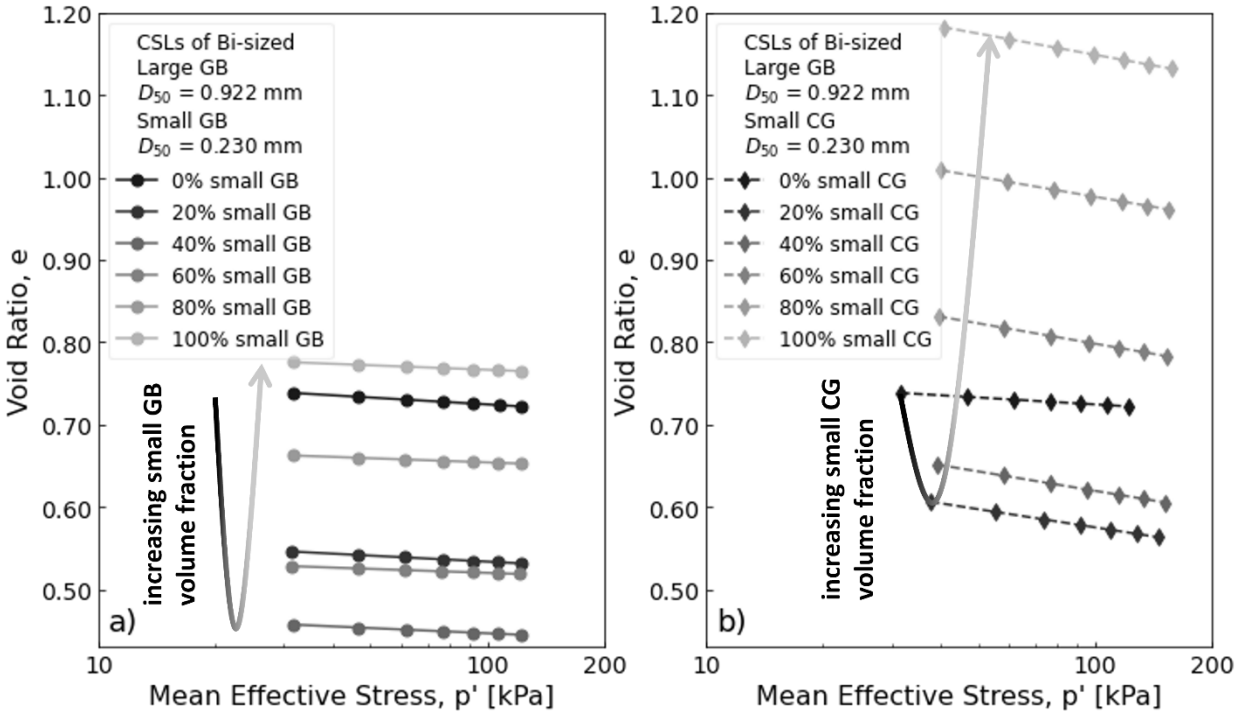

Figure 4.11: CSLs of bi-sized mixtures constituted by large particles with D_{50} = 0.922 mm and small particles with D_{50} = 0.230 mm: (a) both particle sizes are GB, and (b) large size GB and small size CG.

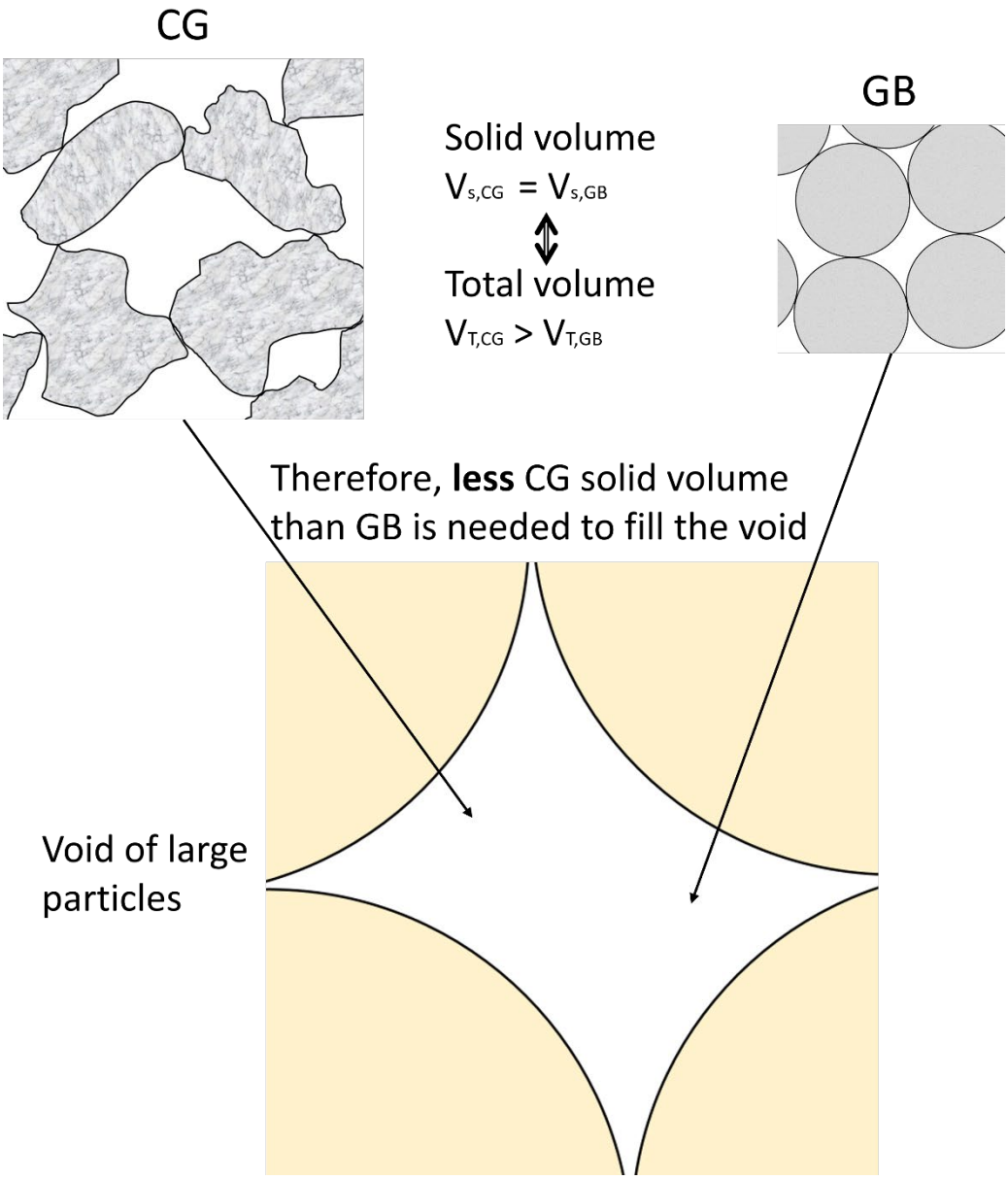

Figure 4.12: A comparison between CG and GB small particles to fill the void between large particles.

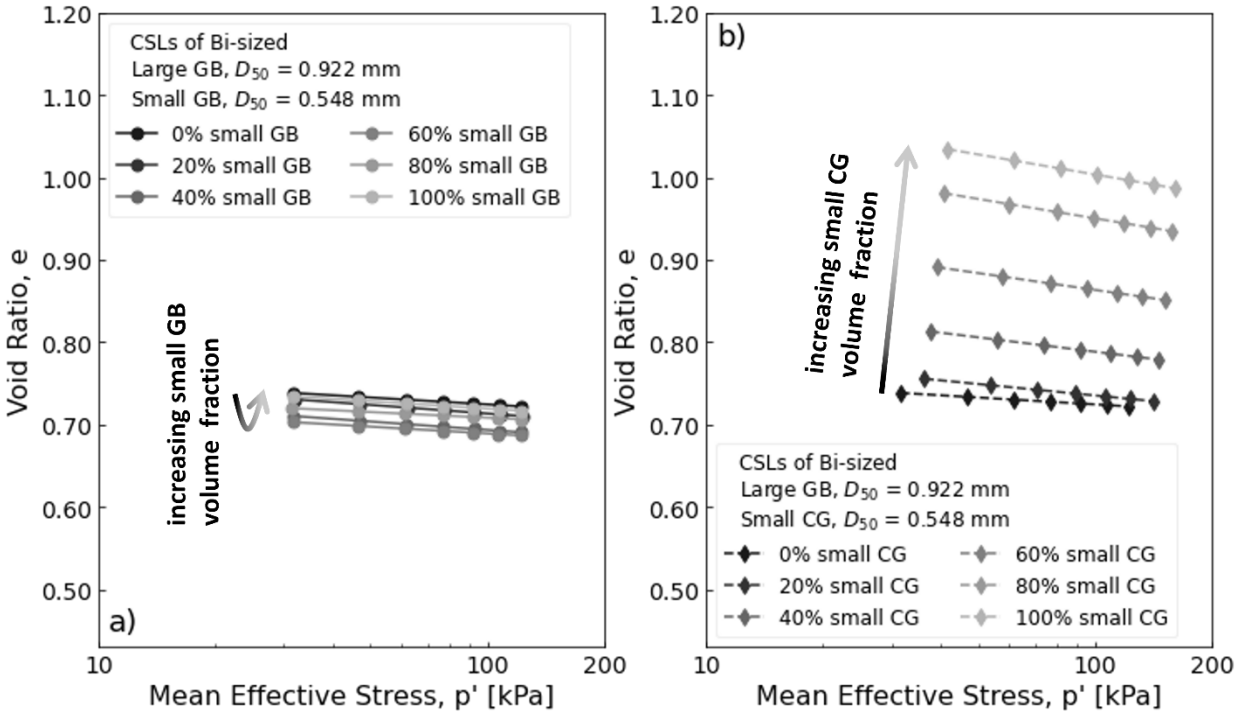

Figure 4.13: CSLs of bi-sized mixtures constituted by large particles with D_{50} = 0.922 mm and small particles with D_{50} = 0.548 mm: (a) both particle sizes are GB, and (b) large size GB and small size CG.

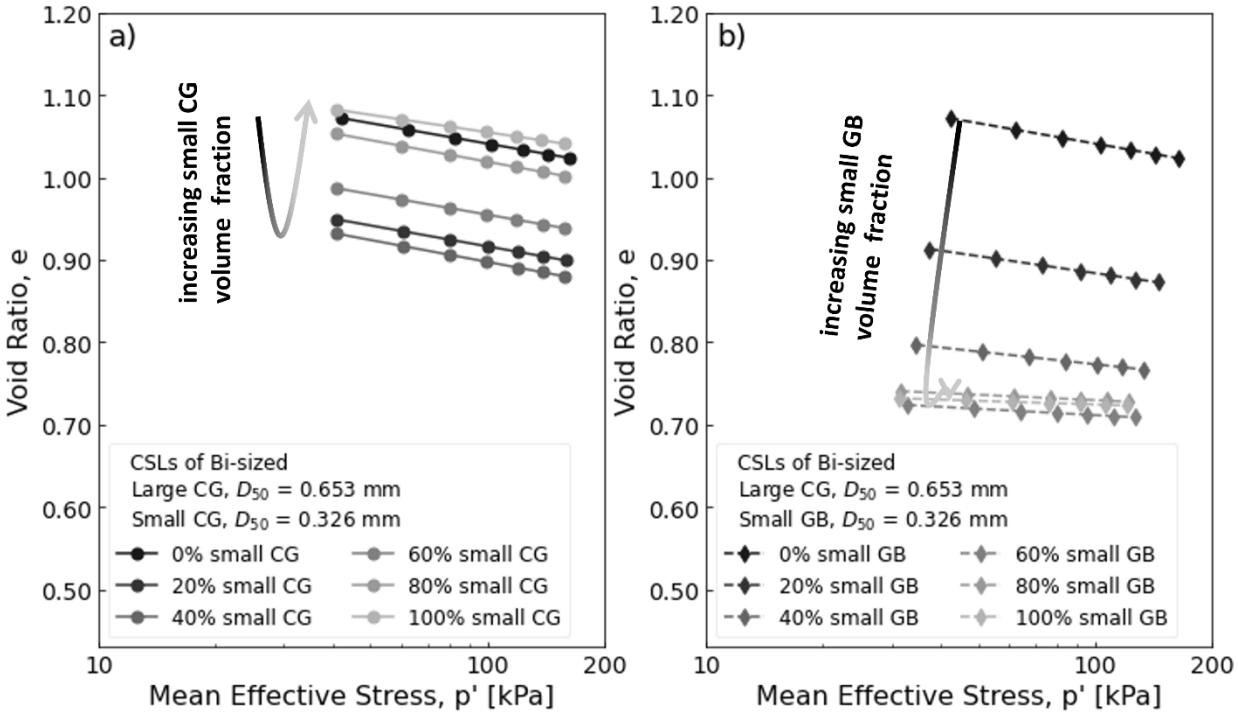

Figure 4.14: CSLs of bi-sized mixtures constituted by large particles with D_{50} = 0.653 mm and small particles with D_{50} = 0.326 mm: (a) both particle sizes are CG, and (b) large size CG and small size GB.

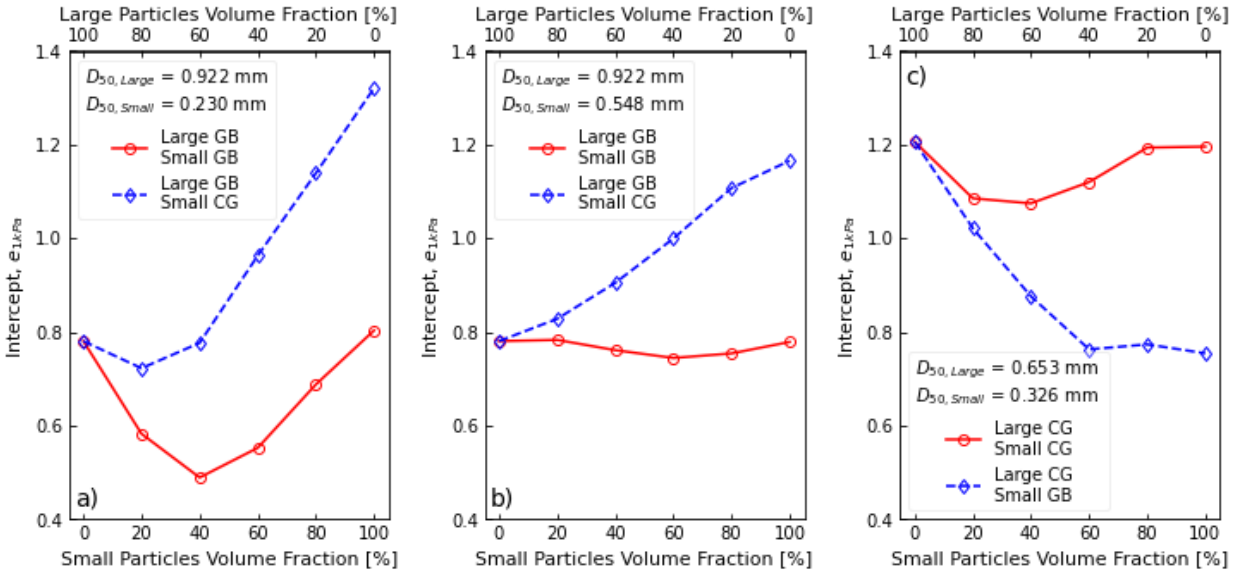

Figure 4.15: e_{1kPa} versus volume fraction of small particles, or large particles in the upper x-axis for bi-sized mixtures: (a) large particles of D_{50} = 0.922 mm and small particles of D_{50} = 0.230 mm, (b) large GB of D_{50} = 0.922 mm and small GB of D_{50} = 0.230 mm, and (c) large particles of D_{50} = 0.653 mm and small particles of D_{50} = 0.326 mm.

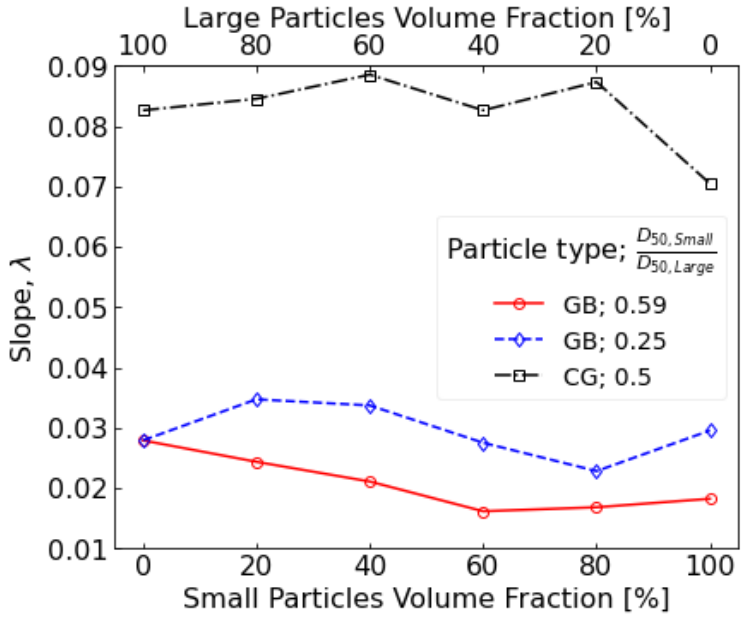

Figure 4.16: Variation of the CSL slope, λ, of GB or CG bi-sized mixtures upon increasing small size volume fraction.

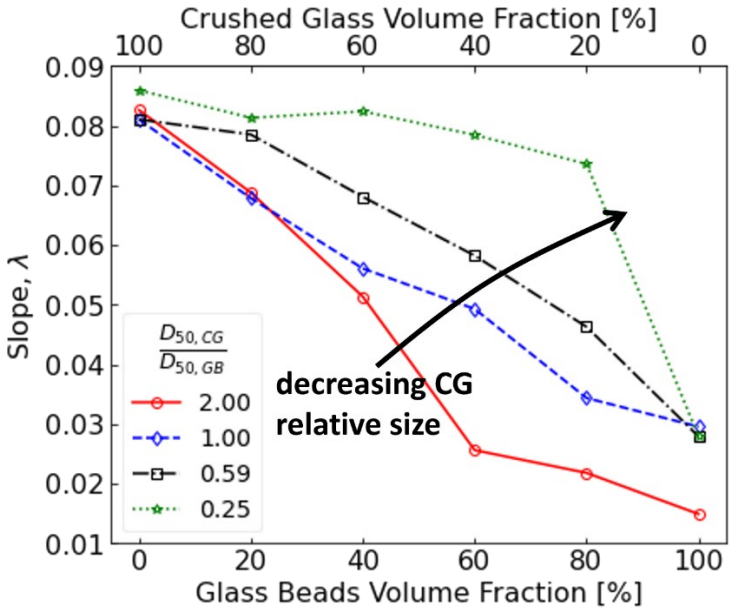

Figure 4.17: Variation of the CSL slope, λ, of bi-sized mixtures upon increasing small size volume fraction. The mixtures are made by one mono-size of GB and the other mono-size of CG.

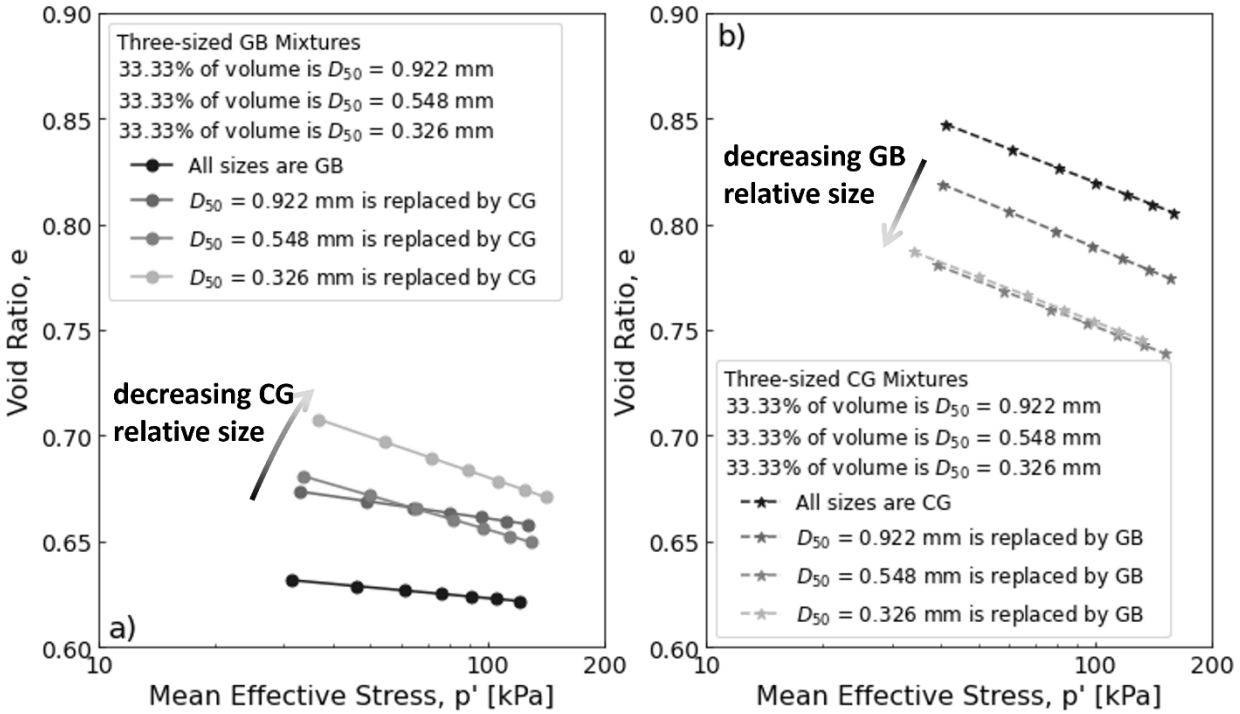

Figure 4.18: CSL's of the three-sized mixtures. (a) GB mixtures, then on size is replaced by CG, and (b) CG mixtures, then one size is replaced by GB.

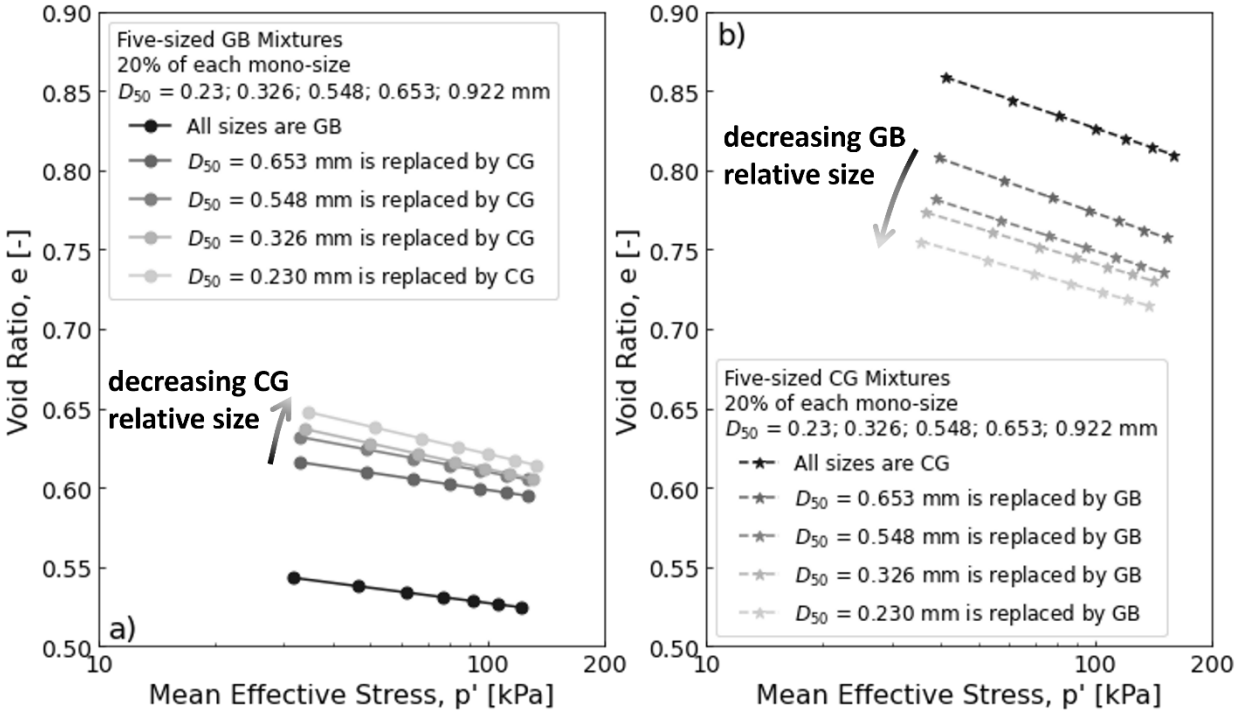

Figure 4.19: CSL's of the five-sized mixtures. (a) GB mixtures, then on size is replaced by CG. (b) CG mixtures, then one size is replaced by GB.

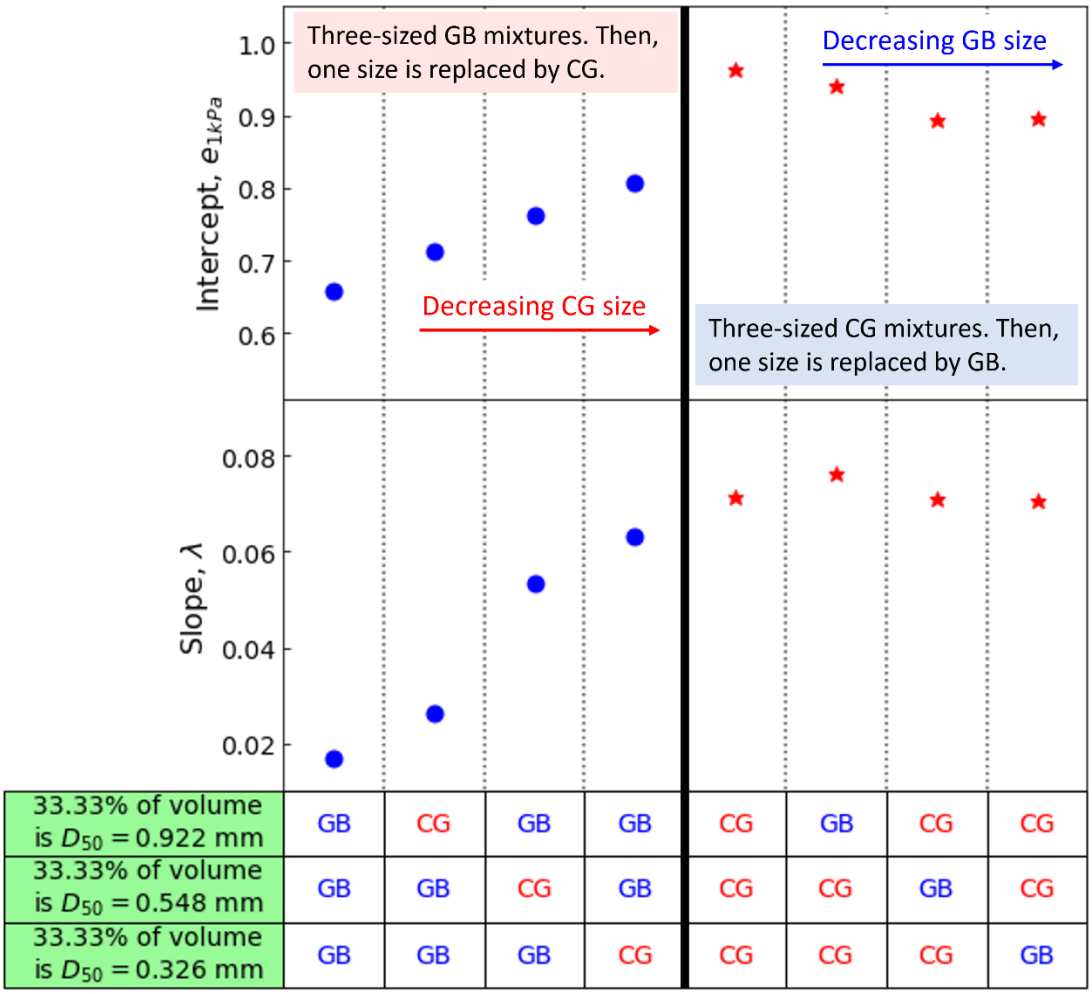

Figure 4.20: The CS parameters of the three-sized mixtures.

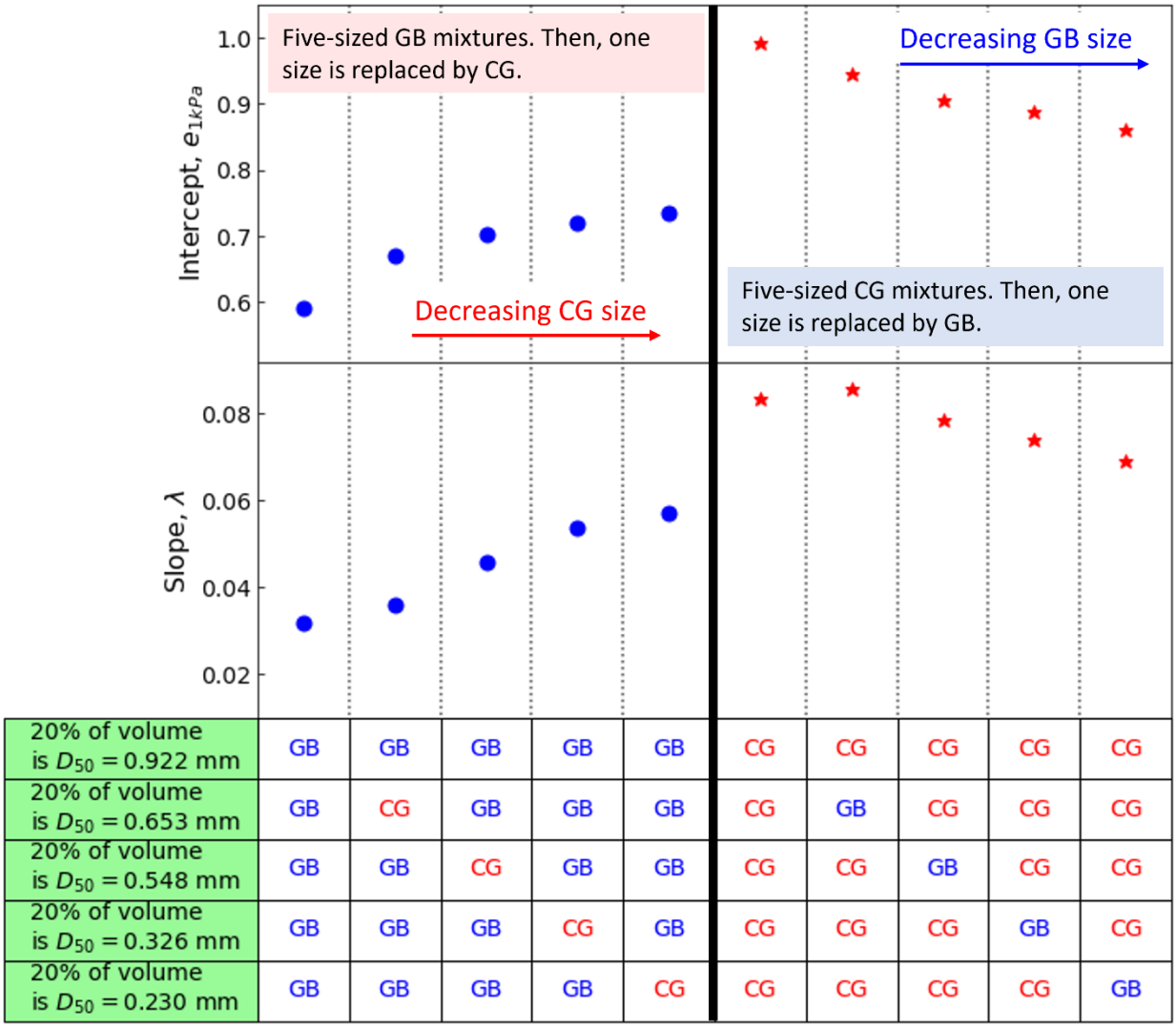

20% of volume is $D_{50} = 0.922$ mm	GB	GB	GB	GB	GB	CG	CG	CG	CG	CG
20% of volume is $D_{50} = 0.653$ mm	GB	CG	GB	GB	GB	CG	GB	CG	CG	CG
20% of volume is $D_{50} = 0.548$ mm	GB	GB	CG	GB	GB	CG	CG	GB	CG	CG
20% of volume is $D_{50} = 0.326$ mm	GB	GB	GB	CG	GB	CG	CG	CG	GB	CG
20% of volume is $D_{50} = 0.230$ mm	GB	GB	GB	GB	CG	CG	CG	CG	CG	GB

Figure 4.21: The CS parameters of the five-sized mixtures.

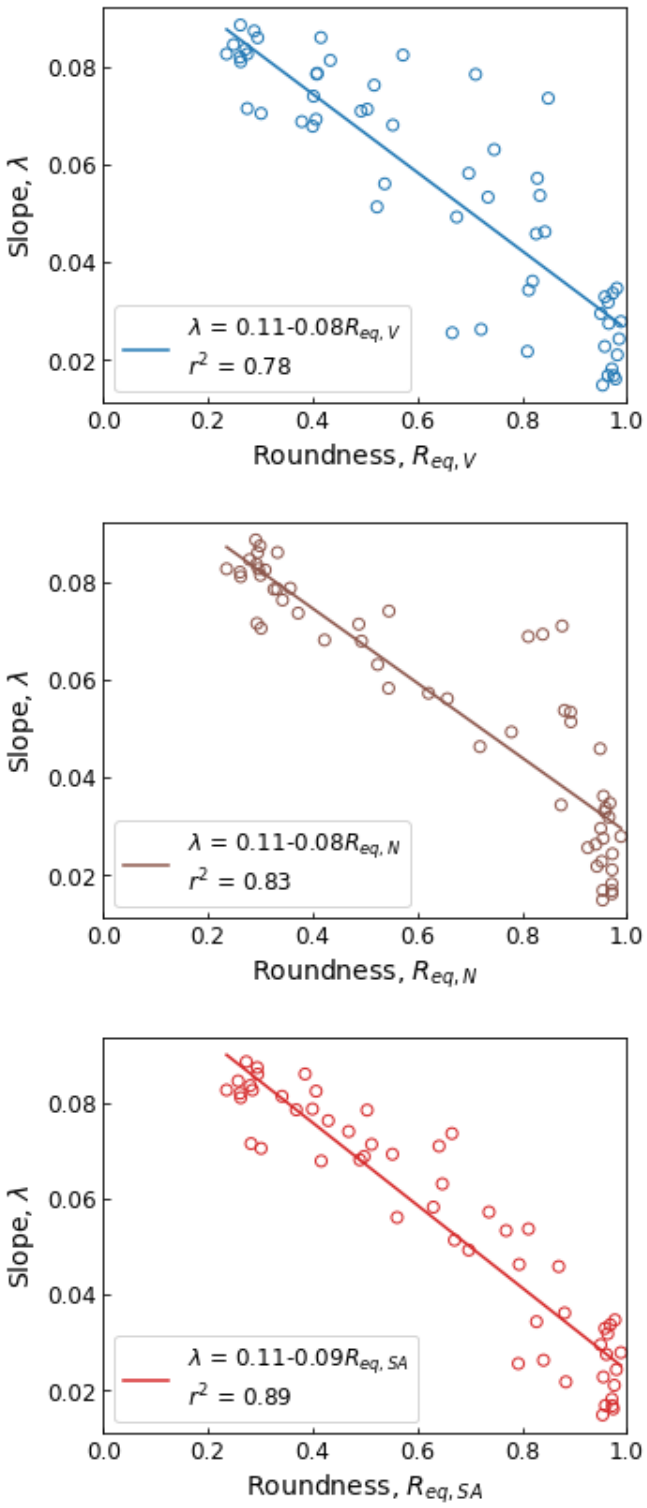

Figure 4.22: λ versus equivalent roundness: (a) equivalent roundness based on volume fraction, (b) equivalent roundness based on the number of particles, and (c) equivalent roundness based on the surface area.

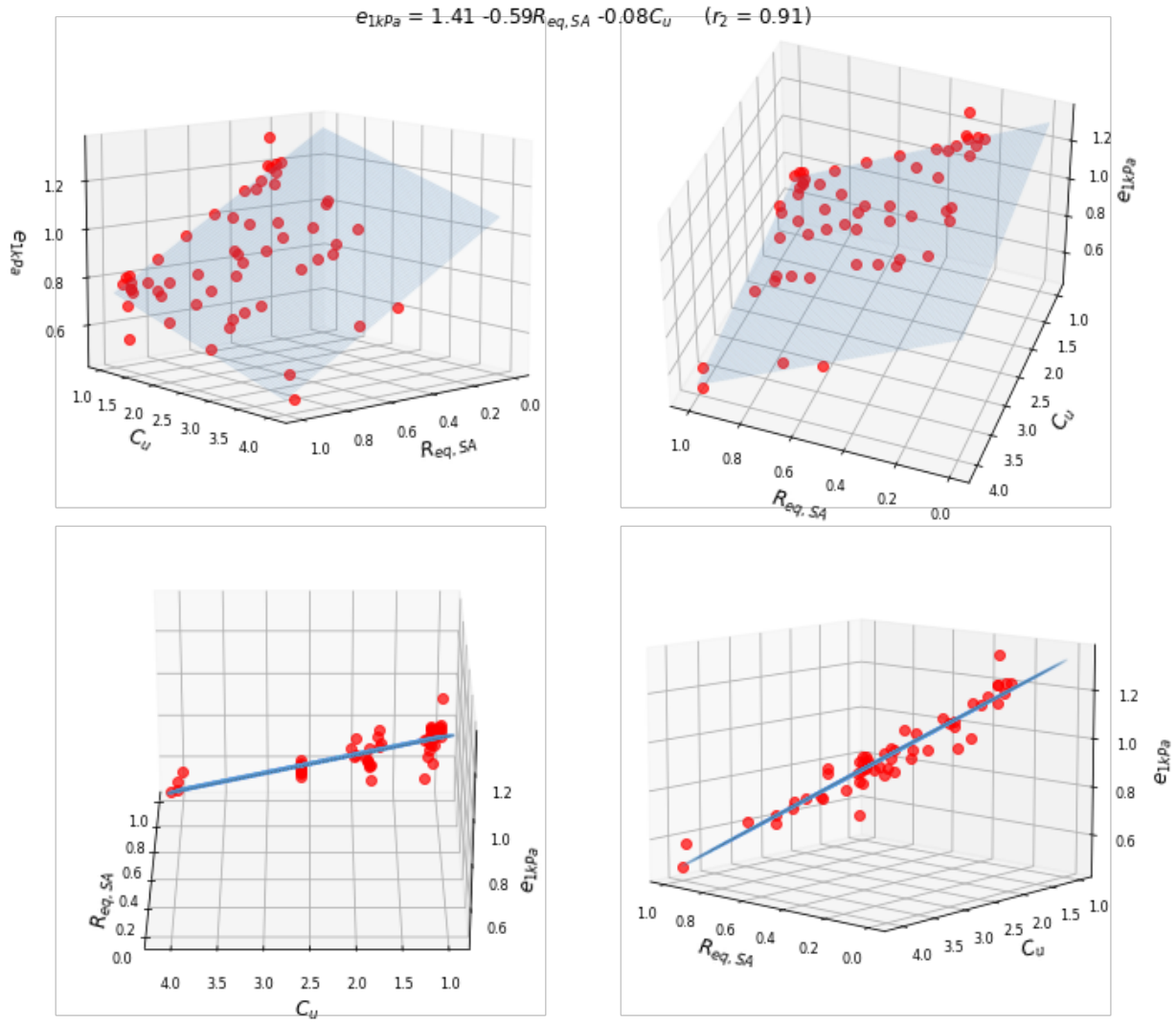

Figure 4.23: Different views of a plane fitting e_{1kPa} data dependent on $R_{eq,SA,}$ and C_u.